DEVELOPMENT OF INTEGRATED DIELECTRIC ELASTOMER ACTUATORS (IDEAS): TRENDING TOWARDS SMARTER AND SMALLER SOFT MICROFLUIDIC SYSTEMS

by

ALEXANDER K. PRICE

M.S., Saint Louis University, 2005

AN ABSTRACT OF A DISSERTATION

submitted in partial fulfillment of the requirements for the degree

DOCTOR OF PHILOSOPHY

Department of Chemistry
College of Arts and Sciences

KANSAS STATE UNIVERSITY
Manhattan, Kansas

2010

Abstract

During the last five years, great advancements in microfluidics have been achieved with the development of "sample-in-answer-out" systems. Such systems have begun to realize the true potential of analytical miniaturization since the concept of the "micro-Total Analysis System" was first envisioned. These systems are characterized by the elegant integration of multiple fluid-handling channel architectures that enable serial execution of sample preparation, separation and detection techniques on a single device. While miniaturization and portability are often identified as key advantages for microfluidics, these highly integrated systems are heavily reliant upon large off-chip equipment, *i.e.* the microchip is often tethered to the laboratory via multiple syringe pumps, vacuum pumps, solenoid valves, gas cylinders and high voltage power supplies.

In this dissertation, a procedure for the facile integration of dielectric elastomer (DE) actuators (called IDEAs) onto microfluidic devices is described. Poly(dimethylsiloxane) (PDMS) is commonly used as a microchip substrate because it is cheap and easy to fabricate, mechanically robust and optically transparent. The operation of an IDEA exploits the ability of PDMS to behave as a smart material and deform in the presence of an electric field. In Chapter 2, the fabrication of IDEA units on a standard microchip electrophoresis device is described. IDEA-derived injections were used to evaluate the physical performance of this novel actuator configuration.

In Chapter 3, the analytical merits of IDEA-derived injections were evaluated. Sampling bias caused by electokinetic injection techniques has been problematic for conventional microchip electrophoresis systems due to the lack of fluid access. The hydrodynamic injections created by IDEA operation were found to be highly reproducible, efficient, and possess a negligible degree of sampling bias. In Chapter 4, the spatial characteristics of microchannel deformation due to IDEA actuation have been investigated using fluorescence microscopy. It was determined that the DE compresses more along the edge of the channel than in the middle of the channel. This information can be used to design a new generation of more efficient IDEAs.

DEVELOPMENT OF INTEGRATED DIELECTRIC ELASTOMER ACTUATORS (IDEAS): TRENDING TOWARDS SMARTER AND SMALLER SOFT MICROFLUIDIC SYSTEMS

by

ALEXANDER K. PRICE

M.S., Saint Louis University, 2005

A DISSERTATION

submitted in partial fulfillment of the requirements for the degree

DOCTOR OF PHILOSOPHY

Department of Chemistry
College of Arts and Sciences

KANSAS STATE UNIVERSITY
Manhattan, Kansas

2010

Approved by:

Major Professor
Dr. Christopher T. Culbertson

Copyright

Abstract

During the last five years, great advancements in microfluidics have been achieved with the development of "sample-in-answer-out" systems. Such systems have begun to realize the true potential of analytical miniaturization since the concept of the "micro-Total Analysis System" was first envisioned. These systems are characterized by the elegant integration of multiple fluid-handling channel architectures that enable serial execution of sample preparation, separation and detection techniques on a single device. While miniaturization and portability are often identified as key advantages for microfluidics, these highly integrated systems are heavily reliant upon large off-chip equipment, *i.e.* the microchip is often tethered to the laboratory via multiple syringe pumps, vacuum pumps, solenoid valves, gas cylinders and high voltage power supplies.

In this dissertation, a procedure for the facile integration of dielectric elastomer (DE) actuators (called IDEAs) onto microfluidic devices is described. Poly(dimethylsiloxane) (PDMS) is commonly used as a microchip substrate because it is cheap and easy to fabricate, mechanically robust and optically transparent. The operation of an IDEA exploits the ability of PDMS to behave as a smart material and deform in the presence of an electric field. In Chapter 2, the fabrication of IDEA units on a standard microchip electrophoresis device is described. IDEA-derived injections were used to evaluate the physical performance of this novel actuator configuration.

In Chapter 3, the analytical merits of IDEA-derived injections were evaluated. Sampling bias caused by electokinetic injection techniques has been problematic for conventional microchip electrophoresis systems due to the lack of fluid access. The hydrodynamic injections created by IDEA operation were found to be highly reproducible, efficient, and possess a negligible degree of sampling bias. In Chapter 4, the spatial characteristics of microchannel deformation due to IDEA actuation have been investigated using fluorescence microscopy. It was determined that the DE compresses more along the edge of the channel than in the middle of the channel. This information can be used to design a new generation of more efficient IDEAs.

Table of Contents

List of Figures

List of Tables

Acknowledgements

Chris – Thanks for taking the time practically every day to sit down and talk/argue (maybe that should be argue/talk) with me about science and joke about everything else. Your passion for your research is one of the reasons why I came to KSU and the main reason why I had a positive experience working in your lab. I have so many awful ideas with a few decent ones thrown in, so thanks for being a sounding board as well as a source of inspiration for the path that our research has taken.

The Culbertson Group – working in a group with so many unique personalities has definitely enriched my experience here at KSU. Thanks for so many moments of levity, especially on those days when Murphy's Law was in effect.

To my friends – Kurt, Scott, Kevin, Tom and Jeff – I've appreciated all the time that we spent together NOT doing or talking about chemistry.

I'd like to thank all of my committee members – Dr. Ryszard Jankowiak, Dr. Takashi Ito, Dr. Bruce Law and Dr. Warren White.

To the Chemistry department faculty and staff – thanks for providing an environment that was conducive to learning and research. I'd like to specifically thank Jim Hodgson, Tobe Eggers, Ron Jackson and Richard Bachamp for creating and fixing the glassware/electronics/machinery that I needed in order to do my research. I'd also like to thank the chemistry office staff – Donna Wright, Connie Cusimano, Mary Dooley and Kim Ross for helping me out so much will all the paperwork needed to keep things running smoothly.

To the Electronics Design Lab – special thanks go out to Tim Sobering and Dave Huddleston for designing and building so much of the complex electronics that we needed (or thought we needed).

To my family – thanks for all of your support over the past 5 years. Everything has changed between when I started and now; the only exception has been that your encouragement of me was unwavering as I travelled this road. To Mom, Dad, Joe and Clayton – whether you know it or not, so much of what I do is based on the example that each of you have provided for me. So thanks for not being a bunch of degenerate sociopaths.

Dedication

To “Papa” Joe Wellington and Carl Stahl

Chapter 1 - Introduction

1.1. Microfluidics

Microfluidics is the study of fluid-based systems that are handled in enclosed channels that possess micro-scale geometries.[1-3] The designation "micro" refers to the characteristic length scale of the fluid handling architecture, which typically lies between 10^{-6} and 10^{-3} meters. With channel widths and depths of this magnitude, microfluidic devices typically handle fluid volumes between 10^{-15} and 10^{-6} liters. It has been known for approximately 20 years that miniaturization of chemical analysis systems will result in a multitude of advantages over conventional, bench-top systems.[4, 5] Fast mass and thermal transport enable large increases in analysis speed. Efficient use of space enables the fabrication of massively parallel systems. These two advantages combine to maximize the high-throughput capability of microfluidics. The miniaturization of the fluid-handling architecture results in a conservation of resources; namely, a reduction in the consumption of reagents, samples, power and dedicated, expertly trained staff. Versatility in the design of microfluidic devices has enabled the development of novel techniques that were previously unfeasible. Other advantages often touted for microfluidics include an increase in sensitivity, portability, affordability and disposability. Lastly, miniaturization allows for multiple sample preparation and analytical functions to be integrated directly to one another. This last advantage will be expounded upon in the following section as integration has become a point of focus within recent years. Overall, these benefits are a direct result of both the design flexibility allowed by microfabrication techniques (discussed in Section 1.2.) and the behavior of fluids in this microscale regime (discussed in Section 1.3.).

1.1.1. Integrated micro-Total Analysis Systems

Within the past ten years and even more so within the last five years, the level of integration on microfluidic devices has increased considerably. The reason for this is that chemical analysis on the nanoliter scale is well suited for research in the life sciences sector, where there is increased interest in the chemical profile of low-abundance cellular material – DNA (genomics), RNA (transcriptomics), proteins (proteomics), metabolites (metabolomics), and lipids (lipidomics). As scientists seek to address increasingly complex questions about these

systems, the incorporation of multiple functionalities into a single microchip has become a necessity. The key advantage of microfluidic integration is that the miniaturized architecture allows for dilution and loss of the sample to be minimized when it is transported from one functional region to another. In addition, contamination becomes negligible because the sample remains in the chip for the entire duration of the experiment instead of being transferred between benchtop instruments.

The ideal micro-total analysis system is one that incorporates every aspect of a quantitative analysis:[6] sample preparation (*e.g.* cell sorting, extraction, reagent metering, mixing, reactions, purification, preconcentration), sampling, eliminating interferences (separation techniques) and detection. Often, introducing functionality is accomplished by the design of the fluidic architecture. For instance, there are three basic channel architectures that are used in microfluidic devices: the straight channel, the T-junction and the cross intersection. Straight channels can be used to perform separations, T-junctions can be used to perform mixing and sorting, and cross intersections can be used to perform valving and flow focusing. Combinations of these three architectures can be used to perform more complex processes.

The design and fabrication of a successful device will greatly depend upon the nature of the operations that will be performed on the device. For instance, the identity and order of the processes to occur on-chip demands forethought upon (1) what type of materials can be used for device fabrication, (2) how different functional regions will be connected or separated from one another, and (3) how samples will be transported between these regions.[7] Samples can be transported between functional regions using electokinetic manipulation and segmented-flow.[8] However, exquisite control over a complex fluidic system can best be accomplished with the use of valves. Programmable mechanical microvalves such as the pneumatic systems created by the Quake[9] and Mathies groups[10] are elegantly designed vehicles for the partitioning, metering and pumping of fluids. To date, highly-integrated systems have been used for genetic analysis,[11-18] single cell analysis,[19-22] enzymatic[23] and protein-binding assays,[24] protein crystallization,[25-27] cell culture/handling,[28, 29] and disease diagnostics/monitoring.[30, 31]

1.1.2. Motivation and Overview

In this dissertation, the results of research aimed at successfully integrating miniaturized electroactive actuators onto microfluidic devices will be reported. The motivation for

developing miniaturized "smart" actuators stems from the need for microscale components that can be operated and completely contained within the smallest space possible. For instance, microfluidic devices less than 8 cm^3 in size can require equipment several thousand times greater in volume in order to perform tasks such as fluid manipulation (pumping, valving, mixing, etc.), temperature control and sample detection. The large size of off-chip components limits the portability, user-friendliness and thus the commercial viability of microfluidic systems. Reducing or eliminating the use of large, off-chip equipment such as syringe pumps, vacuum pumps, solenoid valves, gas cylinders, electromagnetic actuators, tubing and other accessories associated with their use increases the ease with which micro-total analysis systems can be developed for diagnostic "point-of-care" analyses.

In this chapter, the concepts that underlie the operation of the micro-actuators as well as an introduction to microfluidics will be discussed. Chapter 2 will describe the fabrication of microfluidic devices with integrated dielectric elastomer actuators (IDEAs). These proof-of-concept devices were used to evaluate actuator behavior as a function of electric field strength and polymer elasticity under typical operating conditions. Chapter 3 examines the ability of the IDEAs to produce sample injections for electrophoretic separations. Specifically, the actuator-derived injections were evaluated in terms of reproducibility, efficiency, and injection bias. Lastly, the spatial characteristics of channel deformation due to IDEA compression will be discussed in Chapter 4.

1.2. Microchip Fabrication

The first microfluidic device ever fabricated was a miniaturized gas chromatograph made at Stanford University in 1975.[32] The open-tube GC column was made by milling channels in a silicon wafer. Without the aid of computer-controlled equipment, there is little doubt that this process was both tedious and time-consuming. Additionally, it would be nearly impossible to reproducibly create columns having uniform width and depth without the use of expensive machinery. For these reasons, the miniaturization of analytical instrumentation was largely abandoned until the early 1990s, when technology used in the manufacture of integrated circuit (IC) boards was adapted for the fabrication of microfluidic devices. Photolithography, soft lithography and wet chemical processing (etching) are the main technologies responsible for the reproducible and facile fabrication of microfluidic devices. Microfluidic devices can be made

from a wide variety of materials: inorganic materials such as glass, silicon, ceramic and organic polymers such as poly(dimethylsiloxane) (PDMS), poly(methylmethacrylate) (PMMA), polyurethane and cyclicolefin copolymer (COC). The aspects of the fabrication techniques that are most important to the fabrication of PDMS-based IDEA devices will be discussed. PDMS devices are fabricated via soft lithographic molding using a master template. There are two main methods of fabricating this template. A method developed by Effenhauser *et al*. employs a silicon wafer with micromachined features as a master for micromolding.[33] A cheaper and quicker alternative is a method developed by Duffy *et al*., in which the master is fabricated using photolithography,[34] which is detailed below in Section 1.2.1.

1.2.1. Photolithography

Photolithography is a technique that uses the irradiation of a photoactive "resist" to reproduce features from an original pattern, called a "photomask", on the surface of a substrate. The photolithographic process produces a 3-dimensional positive relief mold, which is subsequently used in the soft lithographic process. Photoresists are organic polymers that undergo chemical reactions when exposed to light. Typically, these light-induced chemical reactions will change the average molecular weight of the polymer molecules, but they can also change the chemical reactivity or the polarity of the polymer. The chemical and physical properties that the photoresist possesses after exposure change its solubility in certain solvent systems by orders of magnitude in comparison to what it was before exposure. Photoresists are classified as either negative tone resists or positive tone resists. Upon exposure to light, negative tone resists undergo reactions that strengthen the polymer network, usually through additional polymerization. Conversely, positive tone resists undergo reactions that weaken the polymer network.

One photoresist that is commonly used in the production of molds for PDMS device fabrication is SU-8. A negative tone resist, SU-8 is composed of an epoxy resin (EPON-SU-8) and a triarylium-sulfonium salt photoinitiator dissolved in a solvent (*e.g.* cyclopentanone or gamma butyrolactone). When exposed to light, the photoinitiator produces protons, which catalyze polymerization of the epoxy resin molecules. The reaction yields a high degree of resist cross-linking, which produces very stable structures. In addition to this, SU-8 has other properties that make it advantageous for microfluidic device fabrication. For instance, SU-8

resist is cheap, features good adhesion to many substrate materials, and can be uniformly applied in films between 0.5 and 240 μm thick. SU-8 also has very low absorption down to ~ 380 nm in the near-ultraviolet (UV) region of the spectrum, which facilitates the fabrication of structures with low aspect ratios.

For the fabrication of a mold, a process that is depicted in Figure 1.1, SU-8 is typically spin-coated to a desired thickness on a clean substrate, which is typically silicon or glass. After spin-coating, the resist-covered substrate undergoes a "soft bake", where it is heated in order to remove the majority of the solvent in the resist and to promote adhesion between the resist and substrate. After the soft bake, a photomask is placed in direct or "hard" contact with the surface of the SU-8 layer and the substrate is irradiated through the mask with a predetermined dose of light intensity. The photomask consists of transparent and opaque regions that together define the pattern of the channel network. Since the areas of the SU-8 that are exposed to light are fixed via additional polymerization, the area of the photomask defining the channel network is clear and the surrounding area is opaque.

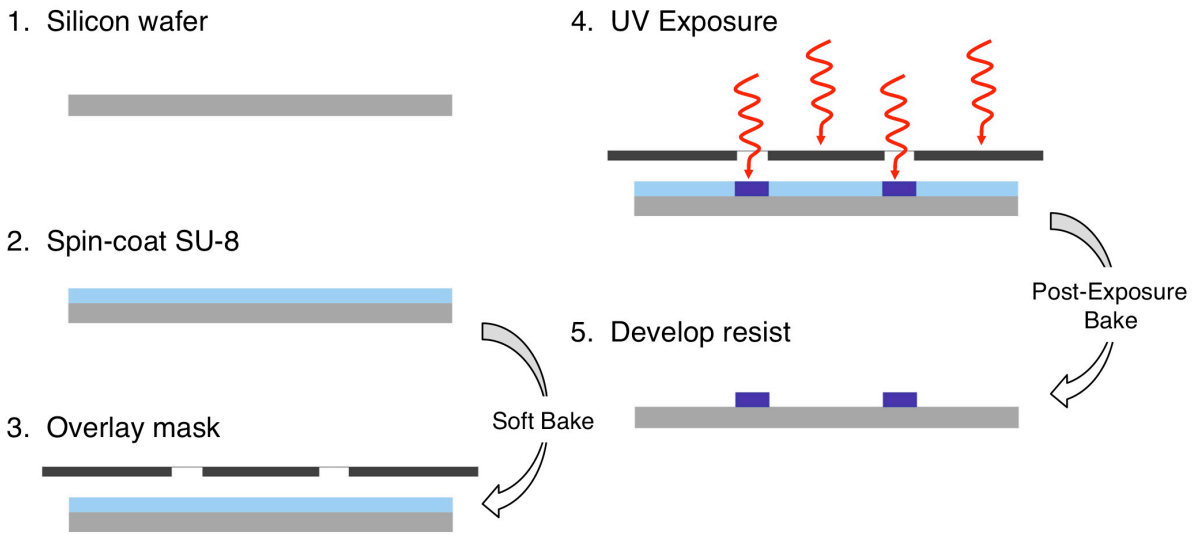

Figure 1.1 Fabrication of an SU-8 resist mold using photolithography. The resist is spin-coated on a silicon wafer, exposed to UV light through a photomask, and developed to remove uncrosslinked SU-8.

The photomask can be a chrome mask or a printed transparency mask. Chrome masks are fabricated by using electron beam lithography to etch the metal off a piece of chrome-plated quartz in the shape of the channel network. While chrome masks feature resolution down to 1

μm, their cost is prohibitively expensive (> $400 per mask) and thus their use is not ideal for the development of prototype systems. Conversely, photomasks can be made by standard or emulsion printing techniques on plastic transparency films. Due to the materials and methods used, transparency masks are cheaper ($2-$150 per film) and faster to produce. Masks can be printed between 1000 and 65k dpi, with a top resolution of ~ 5 μm.

The SU-8 coated substrate is exposed to radiation from a flood exposure system, which consists of a mercury arc lamp and optical components. A digital timer regulates a mechanical shutter in the flood exposure system and its operation determines the magnitude of the radiation dose. The mercury arc lamp features multiple intense emissions in the UV and visible spectrum. Prominent emission peaks exist at 313, 334, 365, 405 and 436 nm. The last three peaks listed are sometimes referred to respectively as the I, H and G lines. A long-pass filter set inside the exposure system is used to block the transmission of light that is more energetic than 350 nm. This is done because SU-8 photoresist absorbs light strongly below this wavelength, so that the top of the resist film is exposed much more than the bottom of the resist film. This phenomenon produces structures whose sidewalls have a large inwardly horizontal component to their slope (also called "undercut" or "negative slope") and whose cross-sectional geometries are highly trapezoidal. In order to help reduce this undercutting phenomenon, the light is passed through a collimating lens prior to exposure.

After exposure, the SU-8 coated substrate is heated once more. This heating step, called a "post-exposure bake", speeds up the rate of the resist polymerization. Once the substrate has cooled down to room temperature, it is developed by submersion in a solvent bath. The developer selectively removes the unexposed photoresist and the areas of exposed resist are left behind as raised structures. This relief, with channel widths and lengths defined by the diffraction of light through the photomask and channel height defined by the resist thickness, is used to replicate these dimensions for the channel network on the final PDMS device.

1.2.2. Soft Lithography

Soft lithography includes a group of techniques in which the features of a structure are replicated in a soft material. These techniques include microcontact printing (μCP), micromolding, and hot-embossing. Of these techniques, both micromolding and hot-embossing are used in the fabrication of microfluidic devices; elastomers are the preferred material for

molding whereas rigid plastics such as PMMA and COC are used for embossing. These techniques are advantageous to use over other microfabrication techniques for numerous reasons. For instance, soft lithography has the ability to replicate 3-dimensional objects very quickly (< 24 hours). Moreover, these techniques are cost-effective since the polymers used are typically less expensive than glass and silicon and hundreds of replicas can be fabricated from a single mold. Lastly, the use of soft, flowable materials allows for structure dimensions on the scale of 10-100 nm to be replicated faithfully.

Micromolding is of particular importance to the work presented in this dissertation since our microfluidic devices are made of PDMS. PDMS is the most common silicon-containing organic polymer, or silicone. As can be seen in Figure 1.2, PDMS features a repeating siloxane (Si−O) backbone with methyl groups on the silicon atoms.

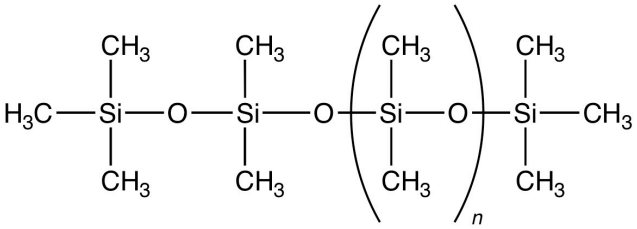

Figure 1.2 The molecular structure of poly(dimethylsiloxane).

The siloxane bonds provide the polymer with a great deal of flexibility because functional groups are able to rotate freely around the center of the bond. At room temperature, PDMS is a liquid. As such, PDMS can be synthesized to have a wide range of viscosities, from 0.65 centipoise (cP) when *n* is small to $1x10^8$ cP when *n* is very large.[35] At molecular weights greater than 10 kDa, the large degree of backbone flexibility leads to a significant amount of entanglement amongst PDMS molecules in the same vicinity. The high degree of entanglement gives PDMS viscoelastic properties. For instance, PDMS will act like a liquid when subjected to forces over long timescales as polymer chains have ample time to slide over one another but will act like a solid when subjected to forces over short timescales as the entangled polymer chains lock together.

The methods developed by Effenhauser[33] and Duffy[34] for fabricating PDMS devices (Figure 1.3) use a commercially available PDMS kit as a liquid precursor.

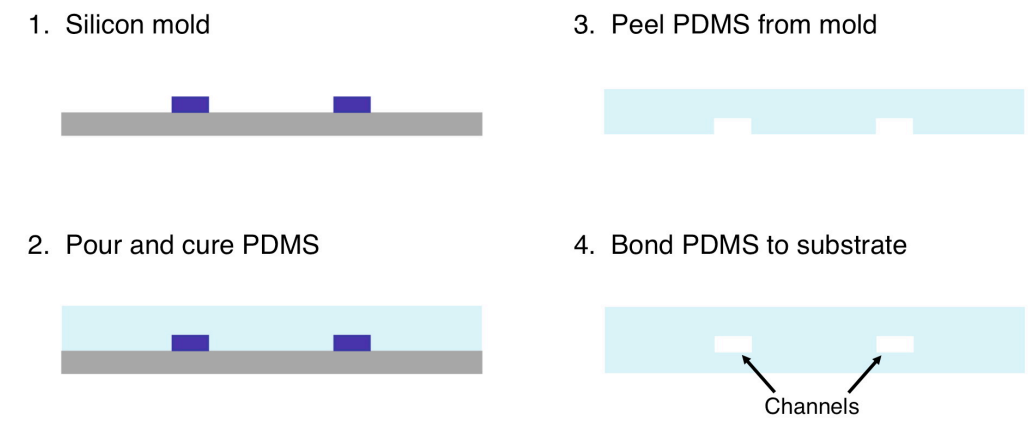

Figure 1.3 Fabrication of a microchip using soft lithography. PDMS precursor is poured onto the mold and cured. The PDMS is then removed from the mold and bonded to another substrate.

PDMS is cross-linked by a Pt-catalyzed hydrosilylation reaction between two or more PDMS precursors. Dimethylvinyl-terminated dimethyl siloxane precursors of variable size typically serve as the long-chain "elastomer base" (Figure 1.4a).

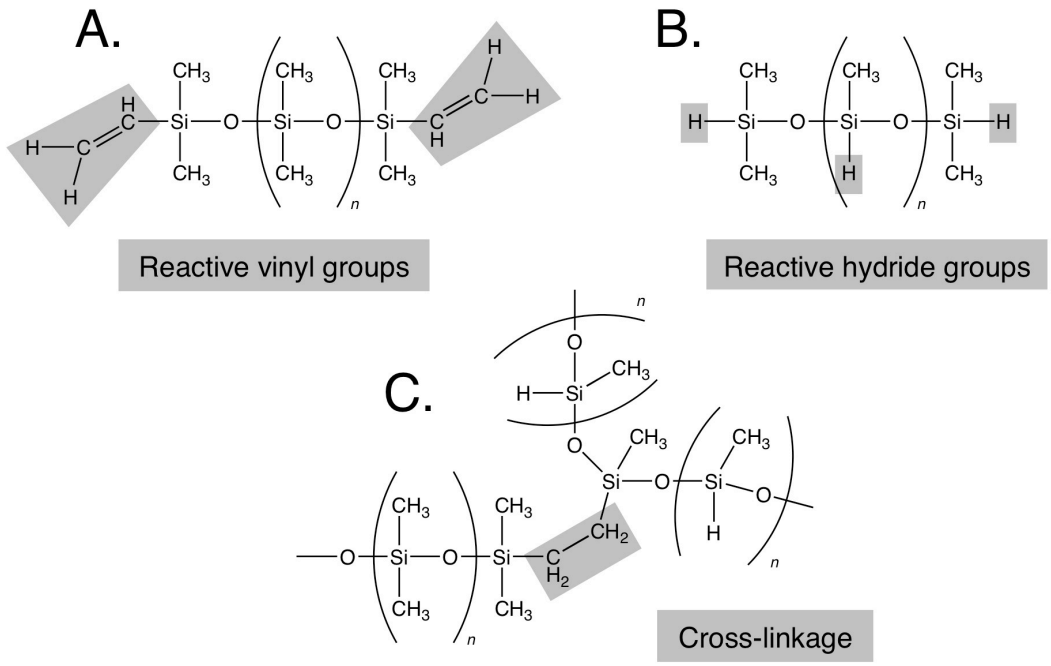

Figure 1.4 The molecular structure of (A) vinyl-terminated PDMS precursor, (B) hydride-containing PDMS precursor, and (C) the cross-linkage between (A) and (B) after a Pt-catalyzed hydrosilylation reaction.

Likewise, dimethyl, methyl hydride siloxane precursors of variable size typically act as the short-chain cross-linkers and possess one hydride group on every silicon atom (Figure 1.4b). These two precursors are mixed thoroughly, degassed in a vacuum, and then poured onto the silicon mold. When mixed together, the hydride and vinyl groups react to form 2-carbon linkages between silicon atoms on different precursor molecules (Figure 1.4c). The amount of cross-linking is dependent upon the quantity of hydride-containing PDMS precursor present in the mixture. If there is a sufficient degree of cross-linking between the precursors, the PDMS becomes solid. Chemically modified fumed silica is also commonly added to the precursor mixture. The silica acts as a reinforcing filler that increases the stiffness and tensile strength of the polymer.[36] The PDMS is typically cured in an oven to speed up the reaction since it can take more than 12 hours at room temperature but less than 1 hour at 80°C.

Once cured, the PDMS chip is peeled off of the mold. Holes are punched in the chip to provide fluid access to the channel network, and it is bonded to a flat substrate in order to completely enclose the channels. The PDMS chip can be reversibly sealed by placing it in conformal contact with a variety of complementary substrate materials: PDMS, glass, silicon, PMMA, and many others. The Van der Waals forces present between the two substrates form a watertight seal. The main advantage that a reversible seal provides is reusability – if a channel becomes clogged with debris, the substrates can be pulled apart, cleaned, and then reassembled. However, the seal can only withstand hydraulic pressures lower than 5 psi within the channels before delamination occurs.

PDMS can also be irreversibly bonded to another substrate. This occurs through the formation of covalent bonds between the PDMS and the complimentary substrate material. With an irreversible seal, the two substrates cannot be separated from one another without bulk material failure; this enables larger pressure drops to be applied in the channels without delamination. One method of irreversibly bonding PDMS to another substrate is to expose both surfaces to oxygen plasma immediately prior to placing them in conformal contact.[34] The ionized air inside the chamber of the plasma cleaner strips exposed methyl ($-CH_3$) groups off the surface of the PDMS. The oxidation of the PDMS surface produces free radical species, which are thought to introduce hydroxyl ($-OH$) and hydroxyl radical ($-OH\bullet$) groups. These oxygen-containing groups are much more reactive than the methyl groups they replaced. When brought into contact with glass, silicon, or another PDMS substrate, the oxidized groups react with one

another and form covalent $R_3Si{-}O{-}SiR_3$ bonds. Irreversible bonding via plasma exposure does require a high degree of technical proficiency, however; the two substrates must be aligned and placed in contact within 10-15 seconds of plasma dissipation before the ionized groups on the substrate surfaces react in air. The time dependent nature of the surface reactivity often results in irreproducible bond strengths between chips.[37]

Simpler, thermal-based methods to bond two PDMS substrates together have been developed. Unger *et al.* have bonded two PDMS slabs with different concentrations of the short-chain precursor.[9] "Stamping" methods use a thin layer of uncured PDMS as an adhesive layer between two fully cured PDMS slabs.[38-40] Lastly, partially cured PDMS slabs can be bonded together.[41] In each of these methods, the hydrosilylation reaction between the two PDMS precursors (Figure 1.4) occurs across the PDMS-PDMS interface, which bonds the entire device together. Since the devices used in this dissertation are made entirely from PDMS, a thermal bonding method is used.

PDMS is used as a material for microchip fabrication because it is cheap and easy to fabricate; PDMS devices can be made quickly without the use of expensive equipment or clean-room facilities. As a material, PDMS is chemically inert, flexible, non-toxic, gas-permeable, optically transparent down to ~ 230 nm and features a low surface energy. These qualities can each be either advantageous or problematic depending upon the application for which the device is used. For instance, its negligible toxicity and gas permeability make PDMS highly suitable for biological applications such as cell culture.[29, 42-44] In addition, its transparency allows for utilization of various optical detection methods in the visible and infrared (IR) regions. However, the low surface energy and hydrophobicity of PDMS promote phenomena that are not ideal for aqueous-based microfluidic applications. PDMS has a tendency to absorb small, non-polar molecules[45] and non-specifically adsorb large proteins. PDMS will swell in organic solvents[46] and features poor wettability for aqueous solutions. Poor wettability is a disadvantage for single-phase aqueous systems but becomes an advantage for dual-phase segmented flow systems.[47, 48]

1.2.3. Wet Chemical Processing

Another dimension of microfabrication is the use of etchants in combination with photolithography in order to create 3-dimensional structures. Wet etching has been used widely

as a method of removing chemical impurities and physical imperfections from the surface of substrates, but it is also used heavily in the IC industry to introduce multiple regions with disparate chemistries on the same surface of a device.[49] In theory, wet chemical etching is a simple process; a material is suspended in a volume of etchant that dissolves its surface. For the purpose of microfabrication, a "mask" or protective layer is typically applied on the material surface (referred to henceforth as the "primary layer") and specific regions where etching is to occur are exposed via lithographic techniques. This mask layer can be composed of many different materials, including photoresist, wax, gold, chrome, titanium, silicon dioxide and silicon nitride. Once the desired amount of etching has been performed, the mask layer is removed. This process can be seen in Figure 1.5.

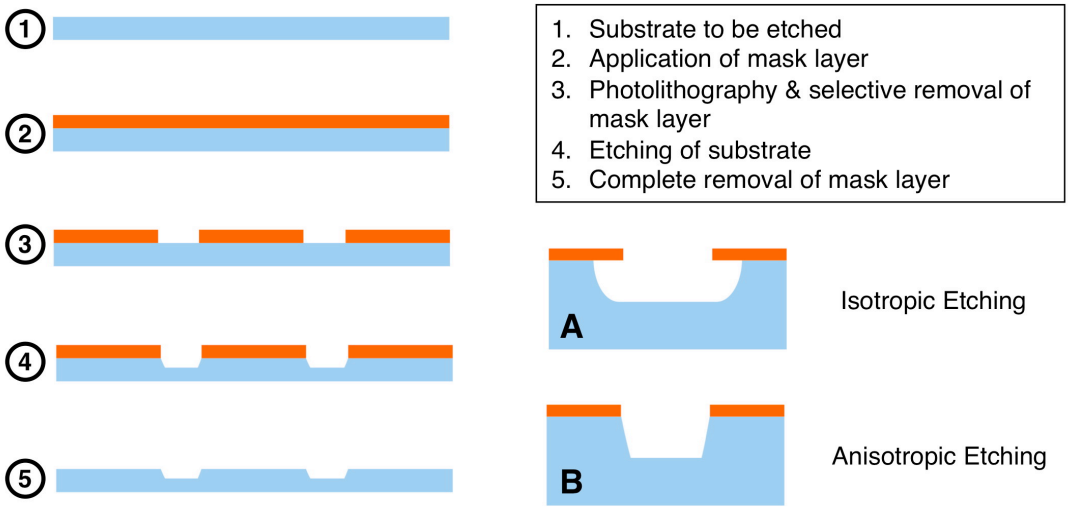

Figure 1.5 Schematic showing the selective etching of a substrate. The insets on the right show the cross-sectional geometry of isotropic (A) and anisotropic (B) etches.

Successful implementation of a wet etching technique depends primarily upon the amount of control over three factors: etch selectivity, etch rate and etch bias. Etch selectivity refers to the difference in the dissolution rate for the primary layer versus that of the mask layer or any layers below the primary layer. It is very desirable to select an etchant solution with a high etch selectivity for the primary layer. If high etch selectivity does not exist between the mask layer and the primary layer, the resultant etch design will have a low degree of fidelity to the original mask design.

Proper selection of the second factor, etch rate, provides fine control over the etch dimensions and expedient etch times for both thick (> 10 μm) and thin (< 1 μm) primary layers. Etch rate is dependent upon the kinetics of three steps in the etch process. In the first step, the etchant is transported to the surface of the primary layer. Once there, the etchant oxidizes the surface material and forms soluble products. Finally, the dissolved products are transported away from the surface of the primary layer. Overall etch rate is dependent upon etchant and primary layer identities, etchant concentration, diffusion, temperature and etch solution viscosity. If the etch rate is limited by transport of the etchant or dissolution products, it can be increased by increasing convection in the etch solution. Conversely, if the etch rate is limited by the reaction kinetics between the etchant and the surface, it can be increased by heating the etch solution.

The last factor, etch bias, describes the difference between etch rates along different planes within the material. Etch bias, which dictates the geometry of the etch profile, is completely dependent upon the structure of the primary layer and the etchant composition. In isotropic etching, the etch rate is the same in all directions, which produces a significant amount of "undercut" beneath the mask layer and creates a smooth contour within the trench (Figure 1.5a). This type of etching is fairly common for amorphous materials such as glass. Isotropic etching is typically diffusion-limited, and is performed at room temperature with acidic etchants. Conversely, anisotropic etching occurs more commonly in crystalline solids and features direction-sensitive etch rates that are dependent upon the orientation of the crystal face. This produces etches that possess little undercut and very sharp corners at the transitions between crystal faces (Figure 1.5b). Anisotropic etching typically employs alkaline etchants that are heated because the process is limited by the reaction rate.

1.3. Fluid Behavior in Microfluidic Devices

1.3.1. Forces on the Microscale

In order to fully understand both the possibilities and limitations of microfluidic-based applications, it is essential to analyze how scale impacts the interactions between matter and the physical forces present in the system. To illustrate this, consider a cube of matter. As the edge length of the cube decreases, so do both its volume and surface area. However, both of these parameters change at different rates, such that the ratio between them (the surface area-to-

volume or SAV ratio) is small when objects are large and increases as the length scale decreases. The SAV ratio becomes very important for both liquids and solids on the order of 10^{-4} meters and smaller. As an example, the SAV ratio has a large influence on cell biology. A lower cellular volume allows for the intracellular diffusion of molecules to occur quickly, as is required in cell-signaling cascades. However, cells also benefit from a lower surface area because it allows them to retain vital nutrients, heat and water. For these reasons, the majority of cells are spheroid or cylindrical with a maximum diameter of 20 μm. Cells may have high SAV ratios if they perform specific functions, *i.e.* nutrient uptake. Inanimate materials having high SAV ratios have increased reaction kinetics and are also more inclined towards surface phenomena such as sorption. In this manner, the behavior of microscale systems is impacted greatly by forces that are typically considered negligible in the macro-world. The most notable microscale forces that affect liquids will be examined here.

1.3.1.1. Viscosity and Inertia

While fluid flow on the macroscale is dominated by inertial forces, microfluidic flow is instead characterized by the viscous forces that act to slow it down. The relationship between these two forces is described by the Reynolds number (Re):

$$\mathrm{Re} = \frac{\rho u d}{\eta} \tag{1.1}$$

where ρ is the fluid density, u is the fluid velocity, d is the characteristic length of the channel (or diameter of the tube), and η is the fluid viscosity. At Re values less than 2300, the flow in an open channel is laminar.[50] The laminar regime consists of well-defined, parallel streamlines that flow side-by-side without disturbing one another. In these circumstances, the mixing of two or more streams occurs only by diffusion. As the inertial forces in the system are increased such that Re is greater than 2300, the fluid streams start to fold over themselves, forming eddies that mix neighboring streamlines via convection. Reynolds numbers for flow in microfluidic channels are usually less than 0.1, which is firmly in the region where viscous forces dominate and flow is laminar.

1.3.1.2. Diffusion

Diffusion is a kinetic process in which molecules move from a region of higher density to a region of lower density until a uniform concentration exists. Diffusive transport is a random process in which there is equal probability of a molecule moving in any direction except beyond the boundaries of the system. As mentioned above, diffusion is a very important form of mass transport in microfluidic devices because laminar flow is the predominant regime. Fick's first law describes the flux of molecules (J) through an area as they are driven towards this concentration equilibrium:[51]

$$J = -D\frac{\partial C}{\partial x} \tag{1.2}$$

where D is the diffusion coefficient of a particular molecule in a particular medium (in cm^2/s), C is the molecule concentration and x is its location in space. Values of the diffusion coefficient depend upon the molecule size, the temperature, and the solvent viscosity; typical values in aqueous solutions range from 1×10^{-5} to 1×10^{-7} cm^2/s. In systems that vary with time, however, diffusion can also be described by the Einstein-Smoluchowski Equation:

$$\sigma^2 = kDt \tag{1.3}$$

where σ is the distance the molecule has diffused, k is a constant and t is the amount of time that the molecule has diffused. The constant k has a value of 2, 4 or 6 depending on whether the molecule diffuses in 1, 2 or 3 dimensions. In chemical separations, k is set to 2 because only diffusion along the length of the capillary or microchannel is capable of changing the concentration profile in a plug of analyte(s). The miniaturization of dimension has significant ramifications for molecular diffusion since distance is directly proportional to he square root of time. Thus, an amino acid will take 1×10^4 seconds (~ 2.8 hours) to diffuse 1 cm in water, but only 10 ms to diffuse 10 μm.

With microfluidic applications where mixing two separate reagent streams is necessary, laminar flow will move the reagents abreast of each other in the channel while diffusive mixing occurs. For situations such as this, the Péclet number (Pe) compares the amount of advection (laminar flow) to diffusion that a molecule experiences. The Péclet number is defined as:

$$Pe = \frac{ud}{D} \tag{1.4}$$

For two analyte streams co-flowing through a microchannel with a constant velocity, the Péclet number represents the number of channel widths that the analytes will flow downstream before complete mixing occurs.

1.3.1.3. Surface Tension

Surface tension, also called surface free energy, is the cohesive force between liquid molecules at an interface. It arises due to the attractive interactions between like molecules, which means that molecules at a surface are attracted in towards the bulk solution. In the macroscale world, we observe the effects of surface tension in both subtle and remarkable examples. For instance, a liquid droplet suspended in air assumes a spherical shape in order to minimize the number of liquid/gas molecular interactions and thus minimize its surface area. Surface tension is also why small objects such as a metal pin can rest on the surface of a liquid, even though they are denser than the liquid. At an interface between two fluids, the pressure across the surface (ΔP) is defined by the Young-LaPlace equation:[50]

$$\Delta P = \gamma\left(\frac{1}{r_1} + \frac{1}{r_2}\right) \tag{1.5}$$

where γ is the surface tension and r_1 and r_2 are the principal radii of curvature that are perpendicular to each other.

On the microscale, surface tension governs many interfacial phenomena and can be manipulated to affect bulk fluid movement through the microchannel network. For instance, the distance (h) that a liquid will wick through a tube is defined as:

$$h = \frac{2\gamma\cos\Theta}{\rho g r} \tag{1.6}$$

where Θ is the contact angle between the wall of the tube and the liquid, g is the gravitational acceleration and r is the radius of the tube. Since the "radii" of microfluidic channels are on the order of microns, aqueous solutions can travel considerable distances through hydrophilic channels by capillary action alone.[52] Virtual walls can be created in microfluidic devices by using laminar flow to selectively pattern regions inside a channel with alternate chemistries

(hydrophilic/hydrophobic).[53] As long as the pressure drop inside the channel does not exceed that defined by Young-LaPlace equation, aqueous solutions flowing through the channel network will confine themselves to the hydrophilic regions, even though they are bounded by solid walls on only two sides. Surface tension also plays a crucial role in the manipulation of segmented flow systems, which feature interactions between aqueous and organic liquids within the channel network. The formation[54], combination[55] and splitting[56] of droplets or "plugs" at channel bifurcations is dependent upon the capillary number (*Ca*), which is expressed as:

$$Ca = \frac{\eta u}{\gamma} \tag{1.7}$$

This dimensionless number represents the magnitude of the shear forces to the surface tension. The balance of these forces provides a threshold that determines whether or not conditions are favorable for the coalescence or division of liquid volumes.

1.3.2. Bulk Fluid Flow

Fluid flow through a microfluidic channel is achieved by creating a pressure drop across its length. This pressure drop can have either a positive or a negative source, *i.e.* the fluid is either pushed or pulled through the channel. As pressure is exerted on the fluid, it begins to flow and accelerates until a steady state velocity is reached. At this point, the viscous forces due to fluid drag are balanced with the applied pressure. The magnitude of the total fluid flux (*U*) is defined as:

$$U = uA_{cs} = \frac{\Delta P}{R} \tag{1.8}$$

where A_{cs} is the cross-sectional area of the channel, ΔP is the pressure drop across the channel and *R* is the resistance to fluid flow in the channel. The fluidic resistance can be calculated as:[50]

$$R = \frac{8\eta L}{\pi r^4} \tag{1.9$_1$}$$

for a tube with a radius *r* and a length *L*. However, most microfluidic devices do not feature channels with circular cross-sections, so the fluidic resistance for a channel with a rectangular cross-section can be approximated as:[50]

$$R \approx \frac{12\eta L}{wh^3} \qquad (1.9_2)$$

where L is the channel length, w is the channel width, and h is the channel height. This equation only holds as long as the channel has a very high aspect ratio ($w >> h$). It is obvious from this relationship that the resistance to flow through a microchannel increases as its length increases and as its cross-sectional area (wh, A_{cs}) decreases.

As can be seen in Equation 1.8, fluid flow through a microchannel is analogous to the flow of current (I) through an electrical circuit according to Ohm's law (V = IR), where the pressure drop is similar to an electrical potential (V) and the fluidic resistance is similar to electrical resistance (R). Just as electrical circuits must obey Kirchoff's laws for charge and energy conservation, fluidic networks in microfluidic devices must obey the laws of mass and momentum conservation. This makes it possible to define the properties of flow in any region of the fluidic network, since fluidic resistances will add directly when placed together in series and add inversely when placed in parallel with one another.

1.3.2.1. Pressure-Driven Flow

Here, pressure-driven flow is defined as the bulk movement of a liquid via an external pressure source, *i.e.* a pump, gravity or centrifugation. When a liquid is pushed or pulled through a conduit, its velocity at the channel wall is zero due to the no-slip boundary condition.[57] Away from the wall, friction between a layer of fluid and the wall or another adjacent fluid layer causes the formation of a velocity gradient across the channel cross-section. This results in a parabolic flow profile (Figure 1.6a), where the velocity of the fluid is zero at the wall and possesses a maximum value at the center of the channel. Since molecules closer to the wall travel slower than molecules at the center of the channel, the parabolic flow profile is one form of dispersion that leads to band broadening in chemical separations (discussed further in Section 1.3.3.3).

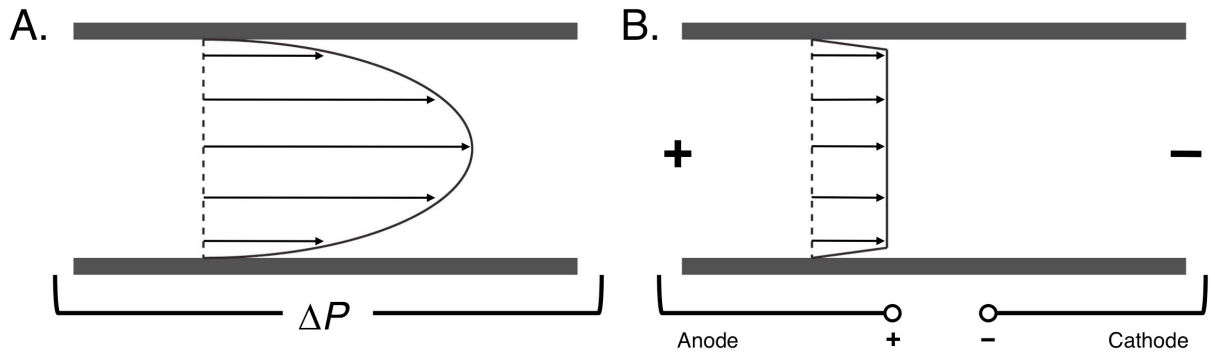

Figure 1.6 Cross-sectional fluid flow profiles for (A) pressure-driven flow and (B) electroosmotic flow.

The maximum velocity in the channel can be calculated as:[58]

$$u_{\max} = \frac{r^2 \Delta P}{4\eta L} \tag{1.10$_1$}$$

for a channel with a circular cross-section and:[58]

$$u_{\max} = \frac{h^2 \Delta P}{8\eta L} \tag{1.10$_2$}$$

for a channel with a rectangular cross-section, assuming a very high aspect ratio. The average fluid velocity inside the channel is defined as:[58]

$$u_{ave} = \frac{u_{\max}}{2} = \frac{r^2 \Delta P}{8\eta L} \tag{1.11$_1$}$$

and

$$u_{ave} = \frac{2u_{\max}}{3} = \frac{h^2 \Delta P}{12\eta L} \tag{1.11$_2$}$$

for channels with circular (Eqn. 1.11$_1$) and rectangular (Eqn. 1.11$_2$) cross-sectional geometries, respectively.

1.3.3. Electrophoresis

Electrophoresis is a single-phase separation method that is based upon the differences in migration rate for a mixture of ions in an electric field. Of relevance to the work presented here, capillary electrophoresis (CE) is based upon the general principles expounded by Arne

Tiselius.[59] Developed in 1981,[60] CE utilizes pieces of fused silica microbore tubing between 50 and 100 cm long with inside diameters between 25 and 100 μm. Electric fields are applied axially along the tubing via a high-voltage (HV) power supply. In-channel field strengths between 300 and 1000 V/cm are required for adequate separation of species and so very large potentials must be applied (10 to 30 kV). In CE, plugs of analyte between 1 and 20 nL can be injected onto the column, separated within 30 minutes and detected quantitatively on the column. Microfluidic capillary electrophoresis (μCE) was one of the techniques first demonstrated in the early 1990s during the emergence of analytical miniaturization.[61-63] In μCE, the rectangular channel cross-sections are typically 50 to 75 μm wide and 10 to 30 μm deep. The higher SAV ratio results in more efficient dissipation of joule heating than in capillary CE systems. In turn, larger field strengths can be applied, which allows for analytes to be separated using channels with lengths less than 20 cm. Due to the decrease in channel length with regards to conventional CE systems, analyses are also shortened with typical separation times less than 10 min. The lower total channel volumes allow microfluidic devices to handle smaller sample volumes, so injections are typically on the order of picoliters. The physics that underlie electrophoresis are explored in the text below.

1.3.3.1. Electrophoretic Flow

Upon application of a field, ions in solution experience a Coulombic force; cations are attracted to the cathode (a negatively charged electrode) and anions are attracted towards the anode (a positively charged electrode). This force (F) is defined as:

$$F = qE = q\frac{V}{L} \tag{1.12}$$

where q is the charge of the ion, E is the electric field strength and V is the applied potential. Conversely, the viscous force that resists movement of an ion (approximated by a spherical particle) is given by the Stokes equation:[64]

$$F = 6\pi\eta r_p u_{ep} \tag{1.13}$$

where r_p is the radius of the ion and u_{ep} is the electrophoretic velocity. These opposing forces quickly reach a steady state and the velocity of an ion in this system can be calculated by combining Equations 1.12 and 1.13:[64]

$$u_{ep} = \frac{qE}{6\pi\eta r_p} = \mu_{ep} E \tag{1.14}$$

where μ_{ep} is known as the electrophoretic mobility. Since it can be generally stated that the mass of an ion is directly proportional to its radius, ions are separated in electrophoresis by differences in their charge/mass (q/r_p) ratio. Cations with larger charge/mass ratios will travel faster towards the cathode than cations with smaller charge/mass ratios, and the same holds true for anions moving towards the anode. Neutral species, however, do not experience any Coulombic forces in an electric field and therefore cannot be separated using electrophoresis.

1.3.3.2. Electroosmotic Flow

Electrophoretic flow is not the only transport mechanism present in electrophoretic systems. Electroosmotic flow (EOF) is the bulk flow that is created when an electrical field is applied to a polar liquid in a conduit. Specifically, this phenomenon is driven by the interfacial chemistry between the liquid (here, an aqueous electrolyte solution) and the wall of the conduit. Most solid surfaces adopt a net electrical charge when they are immersed in an aqueous solution. This may be due to either the adsorption of ions at the solid surface or some type of acid/base equilibria. For fused silica capillaries or glass microchips, the silanol groups that cover the inside surface of the channel wall are deprotonated at a pH greater than 3. For PDMS devices, it is thought that anions are preferentially adsorbed to the channel wall. As a result, the surface of both materials has a negative charge associated with it. Due to the requirement of charge neutrality, cations in solution are attracted to the channel wall and form a region of positive charge known as the electrical double layer (EDL).

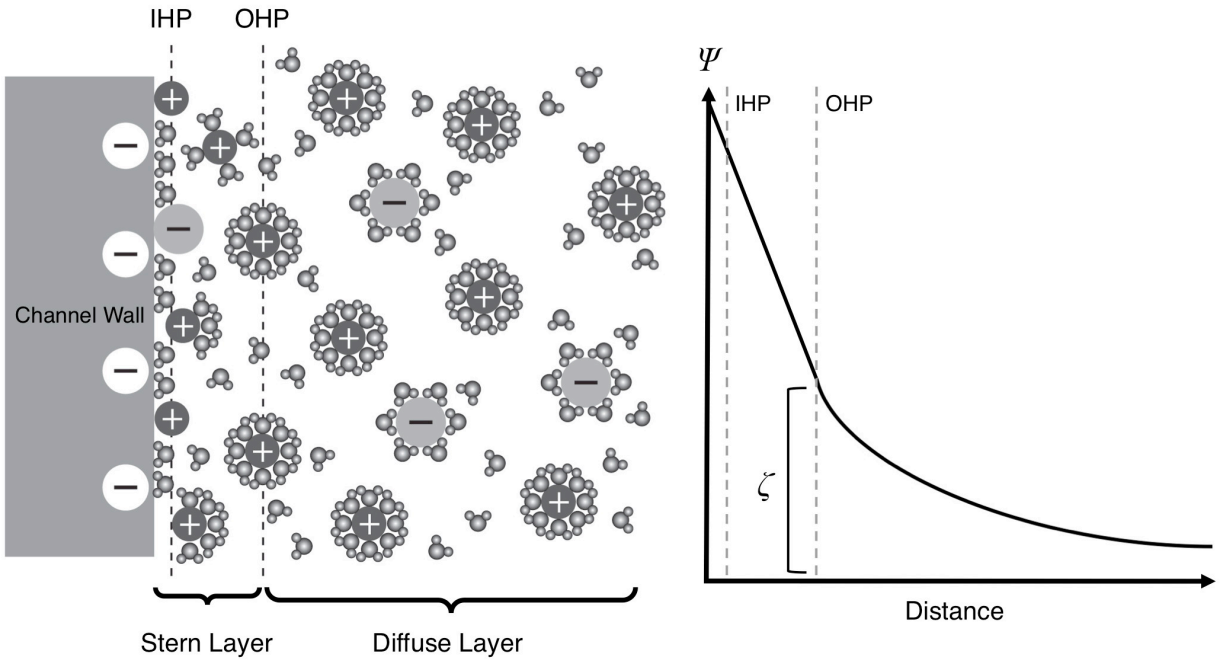

Figure 1.7 Left: Illustration showing the composition of the electrical double layer (EDL) formed at the channel wall when it is filled with an aqueous solution. The Stern layer is bounded by the inner Helmholtz plane (IHP) and the outer Helmholtz plane (OHP). The diffuse layer is bounded by the OHP and the bulk solution. Right: The electrical potential (Ψ) as a function of distance in the EDL.

According to the Stern model, the EDL consists of two regions; these are a compact layer (also called the Stern layer) where the cations are held tightly by strong electrostatic attraction to the wall surface and a diffuse layer where the cations are more solvated and more mobile (Figure 1.7). Some of the cations in the Stern layer are unsolvated and adsorbed directly to the wall surface while partially and fully solvated cations are typically fixed within 0.2 nm of the wall. The thickness of the diffuse layer is also called the Debye length (λ_D, units of meters), and can be calculated for an electrolyte solution at 25 °C as:[65]

$$\lambda_D = \frac{3.04 \times 10^{-10}}{z_i \sqrt{C}} = \frac{2.15 \times 10^{-10}}{\sqrt{I_s}} \tag{1.15}$$

where z_i is the charge of the symmetrical ion pair (+1/-1, +2/-2, etc.), C is the concentration of the electrolyte and I_s is the ionic strength of the electrolyte. For common solutions in which the electrolyte concentration varies between 1 M and 1x10^{-5} M, the Debye length varies between 0.1 and 100 nm. Due to the separation of charge, a potential drop (Ψ) exists between the channel

wall and the bulk solution. The potential decreases linearly across the Stern layer. The potential drop across the diffuse layer, known as the zeta potential (ζ), is very important in determining the velocity of the electroosmotic flow. The zeta potential for an electrolyte solution can be calculated as:[66]

$$\zeta = e^{\left(-\frac{x}{\lambda_D}\right)}\left(\frac{2k_BT}{z_i}\right)\sinh^{-1}\left(\sigma_s\left[\frac{500\pi}{\varepsilon_b RCT}\right]^{1/2}\right) \tag{1.16}$$

where x is the counter-ion thickness, k_B is the Boltzmann constant, T is the temperature, σ_s is the surface charge density, ε_b is the permittivity of the buffer, and R is the gas constant. For most aqueous electrolyte solutions, the zeta potential is less than 100 mV. As the ionic strength of the solution increases, both the thickness of the diffuse layer and the potential drop across it decrease. The electrical potential drops exponentially across the diffuse layer and reaches zero at the bulk solution.

When an electrical potential is applied along the length of the channel, the mobile cations in the diffuse layer become attracted by Coulombic force towards the cathode. As they migrate towards the cathode, the cations pull their hydration spheres along with them, which causes the bulk movement of fluid throughout the entire channel cross-section. Due to the network of hydrogen bonds between water molecules, each fluid layer outside of the double layer moves with the same velocity; this produces a flat flow profile that does not contribute greatly to the dispersion of molecules (Figure 1.6b). The velocity of electroosmotic flow (u_{eo}) is defined as:[64]

$$u_{eo} = \frac{\varepsilon_b \zeta E}{\eta} = \mu_{eo} E \tag{1.17}$$

where E is the electric field strength along the length of the channel and μ_{eo} is the electroosmotic mobility. Since the electroosmotic mobility is dependent upon the zeta potential, there are many different factors that can affect both the magnitude and direction of EOF. These include the ionic strength of the buffer, the presence of additives and impurities in the buffer, the chemistry of the channel wall, pH and temperature. Due to its reliance upon molecular interactions and interfacial chemistry at the channel surface, EOF is characterized by poor reproducibility both over time and among different devices.

Unless EOF is suppressed through surface passivation or manipulation of the solution pH, electrophoretic systems will feature both transport mechanisms described above. Therefore, the total ion velocity (u_{tot}) is equal to the sum of the electrophoretic and electroosmotic velocities:

$$u_{tot} = \left(\mu_{ep} + \mu_{eo}\right)E = \mu_{app}E \tag{1.18}$$

where the sum of the electrophoretic and electroosmotic mobilities is called the apparent (or electrokinetic) mobility (μ_{app}) of the ion. Typically, the electroosmotic mobility is greater than the electrophoretic mobility, so all ions move towards the cathode (Figure 1.8). This is a desirable trait for electrophoresis systems since it allows the researcher to use a single detector.

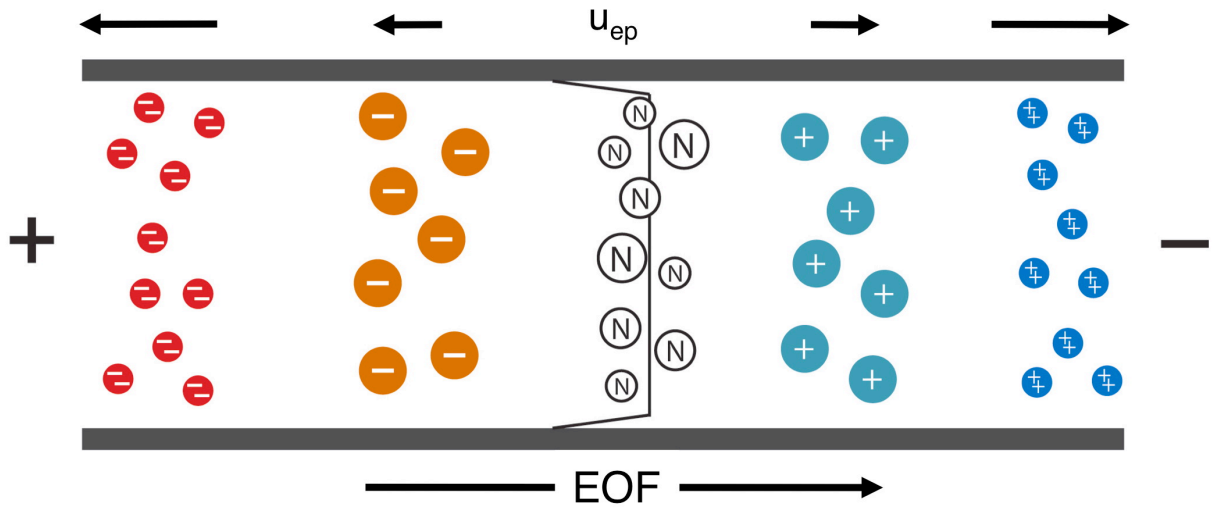

Figure 1.8 Illustration showing the separation of ions based on their electrophoretic velocity, which is based upon their charge/mass ratio. All the ions are carried towards the cathode (−) by the EOF. Neutral species are carried along by the EOF and are not separated from one another.

1.3.3.3. Separation Performance

The goal of a chemical separation is to completely resolve each component of a mixture. In electrophoresis separations, the sample plug is injected at one end of the column and an electropherogram is recorded as the analytes pass by the detection window, which is located a chosen distance downstream of the injection site. Electropherograms are recorded as changes in signal intensity from the detector as a function of time (Figure 1.9). As the sample components

are eluted towards the cathode, they undergo band broadening. The band broadening is due in large part to random molecular diffusion but can potentially be increased by many other phenomena that can also be modeled as stochastic processes. As a result, the detected analyte band usually exhibits a Gaussian profile. The total dispersion that an analyte band can experience during its elution is defined as:[67]

$$\sigma_{tot}^2 = \sigma_{diff}^2 + \sigma_{inj}^2 + \sigma_{\det}^2 + \sigma_{joule}^2 + \sigma_{geo}^2 + \sigma_{MT}^2 + \sigma_{ads}^2 + \sigma_{edisp}^2 + \sigma_{flow}^2 \quad (1.19)$$

where σ_{tot}^2 is the total variance of the analyte band and the right side of the equation are the individual sources of band broadening that contribute to the total variance. These are diffusion (*diff*), the initial injection length (*inj*), the detection window length (*det*), joule heating (*joule*), channel geometry (*geo*), mass transfer effects (*MT*), molecular adsorption (*ads*), electrodispersion (*edisp*) and parabolic flow (*flow*), respectively.

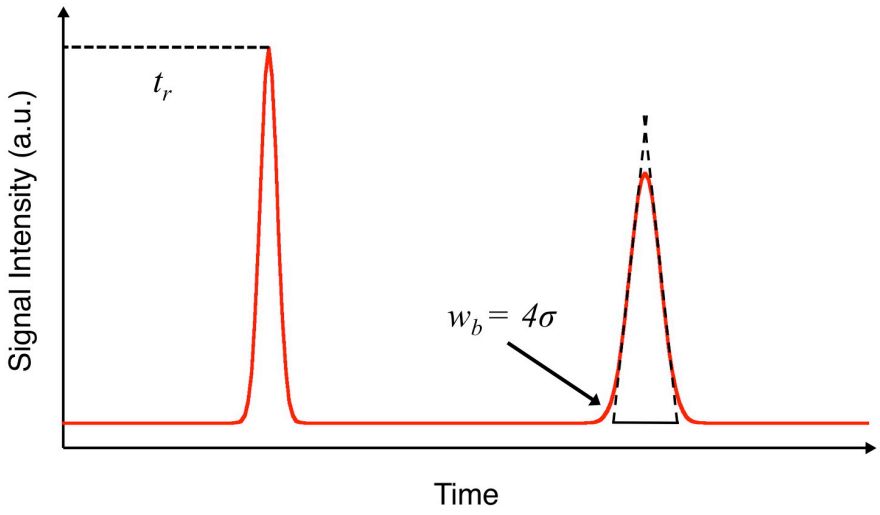

Figure 1.9 A sample electropherogram showing the elution of two analyte bands. The peak migration time (t_r) and peak width at the base (w_b) are shown on the graph. These properties are used to calculate separation efficiency and resolution, two indicators of separation performance.

The contribution from most of these sources of dispersion is negligible except under extreme conditions and therefore can be controlled easily. Joule heating, which arises from friction between migrating ions and the surrounding fluid, becomes significant only when the field strength exceeds 1000 V/cm. Keeping the ion concentration of the sample three orders of magnitude lower than that of the electrolyte buffer minimizes electrodispersion, which is caused

by large differences in the ionic strengths of the sample and the buffer. Dispersion due to parabolic flow is minimized by keeping the height of the solution in the channel reservoirs roughly equal so as to avoid a siphoning effect caused by generation of hydrostatic pressure.

The total variance can be determined from the electropherogram via the width of the Gaussian peak at its base (w_b):

$$w_b = 4\sigma \tag{1.20}$$

One important thing to remember is that systems predicated upon fluid flow can be analyzed in both time and space; that is, the peak width can be measured in units of time ($w_{(t)}$) directly from the electropherogram or calculated in units of length ($w_{(l)}$) as follows:

$$w_{(l)} = w_{(t)}u \tag{1.21}$$

and the same can be said for both the standard deviation of the peak (σ) and the variance (σ^2). In order to distinguish between these two forms of the same peak parameter, the terms "spatial" or "temporal" will be used in the following text when necessary.

It becomes easier to fully separate each component from a mixture if the peak variances are minimized. This is especially true for samples with a large number of analytes. However, a small peak variance in and of itself tells the researcher very little about the resolving power of the separation technique. Thus, there are a couple of parameters that are used to assess the quality of a separation. One of these, separation efficiency, evaluates the amount of band broadening relative to the length of the channel. In order to numerically assess separation efficiency, it is essential to introduce the concepts of plate height (H) and number of theoretical plates (N). The nomenclature used here is taken from the "plate theory" developed by Martin and Synge.[68] Although this view of mechanistic band broadening has since been eschewed in favor of "rate theory", H and N remain heavily used.

For optimal electrophoretic separations, plate height (in units of length) is expressed as:

$$H = \frac{\sigma^2}{L_D} \tag{1.22}$$

where σ^2 is the spatial variance associated with the analyte band and L_D is the separation distance. By combining Equation 1.22 with the Einstein-Smoluchowski Equation (Equation 1.3), plate height can be calculated as:

$$H = \frac{2D}{u} \tag{1.23}$$

Smaller plate heights are indicative of more efficient separations since it indicates that peak variances remain small even though the analyte band has traveled a considerable distance.

The number of theoretical plates is related to plate height by the following equation:

$$N = \frac{L_D}{H} = \frac{\left(L_D\right)^2}{\sigma^2} \tag{1.24}$$

The number of theoretical plates is a dimensionless number that is the most commonly used indicator of separation efficiency; larger plate numbers correspond to more efficient separations. Alternatively, the number of theoretical plates can be calculated in CE systems by combining Equation 1.18, Equation 1.23 and Equation 1.24:[64]

$$N = \left(\frac{\mu_{app} V}{2D}\right)\left(\frac{L_D}{L}\right) \tag{1.25}$$

It is evident from these equations that increasing the efficiency of a separation requires increasing both the velocity of the analyte bands and increasing the distance over which they are separated. Analyte velocity is an important factor considering that molecular diffusion is the dominant contributor to peak variance – the faster the analyte band moves through the channel, the less time it has to broaden out.

However, faster separations require longer separation distances so that all the analytes in a mixture can be resolved. Resolution (R_s) is a parameter that describes how well analyte peaks are separated from one another. The resolution between two peaks, called A and B here, is calculated generally as:

$$R_s = \frac{2\left[\left(t_r\right)_B - \left(t_r\right)_A\right]}{\left(w_b\right)_A + \left(w_b\right)_B} \tag{1.26}$$

where t_r is the migration time of the analyte peak and w_b is the temporal width of the peak at its base. In order for two peaks to be considered baseline resolved, their R_s must be 1.5 or greater. Resolution in an electrophoretic separation can also be expressed in terms of mobility and the separation efficiency:[64]

$$R_s = \frac{\sqrt{N}}{4}\left(\frac{\Delta\mu_{A,B}}{\mu_{ave} + \mu_{eo}}\right) \tag{1.27}$$

where $\Delta\mu_{A,B}$ is the difference in the mobility between peaks A and B and μ_{ave} is the average mobility ($\mu_A + \mu_B$ / 2). It is evident from this equation that the resolution between a cationic species and an anionic species will be much greater than the resolution for two analytes that are attracted to the same electrode.

1.4. Introduction to Smart Materials and Smart Systems

In the past century, a wide array of synthetic materials has been developed in order to produce structures with a specific set of physical properties. For instance, the formulation and processing conditions used to make plastics can be changed to bestow the finished product with specific degrees of softness/hardness, rigidity/pliability, and opacity. The property sets chosen for these materials are meant to best serve the structure in its application over a broad range of environmental conditions. The performance of such "general-use" materials is vastly different from biopolymers such as proteins and DNA. Not only do these molecules serve as physical structures, but many can also sense the physical and chemical state of their environment and change their own properties accordingly. Indeed, such "smart" behavior is necessary in order to streamline cellular processes, which must be done quickly and with as few operating components as possible.

Lately, there has been a significant effort to create structures that possess multiple functionalities or property sets and the ability to transition reversibly between them as the local environment changes. These structures have the possibility of functioning in two ways. In the first, the smart structures operate strictly as sensors, providing information as to their current state or environment (Signal In, Answer Out). In the second, the smart structures can not only sense their local environment, but also respond to external stimuli in an automatic and predetermined manner (Signal In, Action Out). Smart materials and smart systems are highly desirable for commercial and engineering purposes because they can significantly improve safety and conserve natural resources by collecting and analyzing information that conventional, insensitive ("dumb") systems cannot. Currently, there are a large variety of smart materials that have been developed, responding to a diverse group of external stimuli: mechanical force, temperature, magnetic fields, electrical fields, pH, and light. A change in one of these conditions

is recognized by the material, which can transduce the energy from the stimulus into a change in shape (piezoelectrics, shape memory materials, electroactive polymers), color (halo-, photo-, electro-, and thermochromic materials), light emission (light emitting diodes, photodiodes), electric field strength (piezoelectrics) and viscosity (non-Newtonian fluids).

1.4.1. Electroactive Polymers (EAPs)

Electroactive polymers (EAPs) are a class of organic smart materials that change shape in the presence of an electric field. The shape change that occurs is a scaled response that allows these polymers to be used as both sensors and actuators. As actuators, these polymers are capable of undergoing large displacements and finishing that displacement in a "catch state". A catch state is a "locked" conformation that persists for the duration of the electric field, assuming its magnitude remains constant. EAPs also possess high energy densities as they are lightweight materials and power consumption is very low since energy isn't expended while the EAP is in its catch state. For these reasons, EAPs have become materials of interest for the robotics industry since their motive behavior appears to closely replicate that of skeletal muscle. Additionally, EAPs are being investigated and optimized for use in a diverse set of applications that includes pumps, motors, acoustics, medical prosthetics, micro air vehicles (MAVs) and haptic devices.[69-77]

1.4.1.1. Ionic EAPs

Ionic EAPs are one of the two major classes of electroactive polymers. When an electric field is applied in the presence of an ionic EAP, the conformational changes that occur are propagated by the movement of ions in an electrolyte solution with which the polymer is in contact. Effective actuation for materials such as ionic gels[78] and ionic polymer-metal composites (IPMCs)[79-81] is realized when the polymer is sandwiched between two electrodes. In response to an electric field, the flux of mobile ions toward a particular electrode causes local regions of the polymer to shrink or swell by either physical or chemical mechanisms. In contrast, materials with low electrical resistivity such as conducting polymers (CPs)[82, 83] and carbon nanotubes (CNTs)[84] are able to act as electrodes in actuation systems. Upon application of an electric field, deformation of these materials will occur due to migration of ions into the polymer matrix or charge injection, which increases the bond length between atoms in the polymer backbone.

Due to their reliance upon the movement of ions, ionic EAPs must be kept wet during operation. Since the electrical resistance of these systems is so low, potentials used to create actuation are typically between 1 and 5 V. Application of larger potentials increases the risk of hydrolysis, which can delaminate metallic electrodes and disrupt ion movement through gas production. Asymmetric shrinking or swelling between paired EAP strips usually leads to a bending action as opposed to a compressive or elongating action. Thus, while ionic EAP actuators typically produce large deformations, poor coupling efficiencies result in low actuation forces. Additionally, the migration of ions back and forth between the electrolyte and the polymer results in large response times, ranging from 10^{-1} to 10^{2} s.

1.4.1.2. Electronic EAPs

Unlike ionic EAPs, the conformational changes produced by electronic EAPs are the result of static charge generation. The application of an electric field causes polarizable functional groups to reorient themselves in order to align with the field. In doing so, the conformational changes to each individual polymer molecule collectively produce a conformational change to the bulk polymer matrix. This phenomenon is known as electrostriction. Additionally, the application of the electric field produces a separation of charge on opposite sides of the polymer. The presence of static charges generates Maxwell stress, which seeks to deform the polymer in the direction of the field. Usually, one of these actuation mechanisms dominates the system; this is dependent upon both the chemical constituency and the physical nature of the polymer. The bulk resistivity of electronic EAPs is very large, and so the strength of the electric field must be large in order to produce significant deformations. Typical field strengths are on the order of 60-150 V/μm, which is close to the dielectric breakdown strength for most of these polymers. Such large voltages not only have the potential to destroy the EAP, but pose a safety risk to anyone coming into close contact with the device. Despite the necessity of high voltages, electronic EAPs can be stably operated in air over a wide range of temperatures (from as low as -125 °C to 250 °C) and exhibit fast response times (10^{-6} – 10^{-3} s).

1.4.2. Dielectric Elastomers

Dielectric elastomers (DEs) are a subclass of electronic EAPs that are electrically insulating and possess high elasticity. Comprised mainly of silicones and acrylics, DEs are

lightweight and mechanically robust. A schematic representation of an elastomer solid is shown in Figure 1.10. In this figure, the long strands represent long-chain polymer molecules and the bars represent shorter-chain crosslinking chains that covalently bond two or more long-chain segments together. As an elastomer at rest (Figure 1.10a) is stretched, the flexible long-chain segments unfold and slide over one another in order to accommodate the stress (Figure 1.10b). It is evident that as the polymer chains extend along the axis of the applied strain, the polymer chains perpendicular to this axis are pulled in towards the center, reducing the elastomer thickness in this dimension. Indeed, elastomers are generally regarded as being incompressible, *i.e.* having a Poisson's ratio of approximately 0.5. When the applied stress ceases, the long-chain segments relax and the elastomer returns to its original shape.

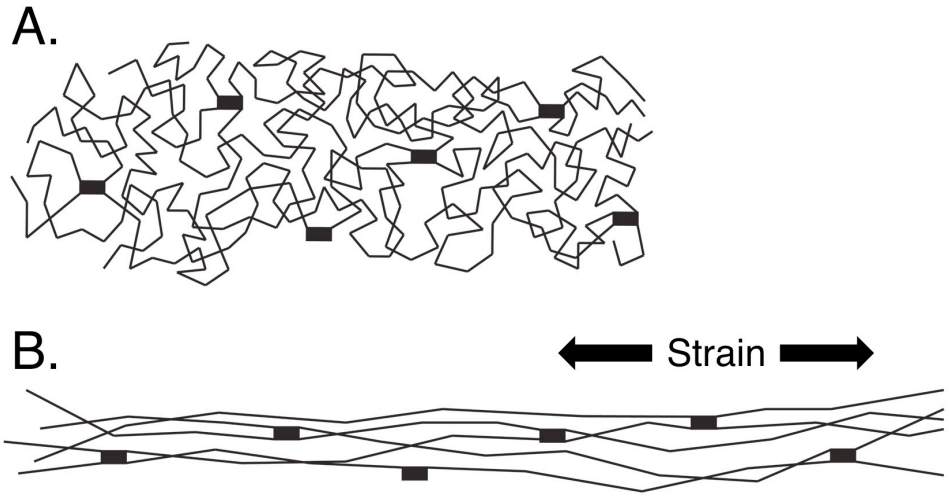

Figure 1.10 Schematic of an elastomer solid (A) at rest and (B) under strain.

The high restoring force of the polymer ensures that there is very little hysteresis when transitioning between strained and unstrained states. In order to ensure that the polymer has a reproducible viscoelastic stress response, the right amount of cross-linking is critical. If not enough cross-linkages are present, the restoring force of the polymer will be too low to successfully return it to its original shape; this permanently damages the polymer. If too many covalent cross-linkages are present, the polymer will more closely resemble a crystalline lattice, which greatly reduces the flexibility of the long-chain polymer segments.

The simplest method of fabricating a DE actuator is by sandwiching a thin layer of the elastomer between two electrodes (Figure 1.11a). The thickness of the DE layer is generally

between 20 and 200 μm. Below 20 μm, the resultant strains will be too insignificant; above 200 μm, the use of extremely high voltages is required. The thin layers of elastomer required for DE fabrication are cheap and easy to produce. Film processing is reproducible at small scales using molding and spin-coating procedures and would be amenable to extrusion techniques for large-scale fabrication. A potential difference between the electrodes results in the formation of an electric field across the thickness of the DE layer.

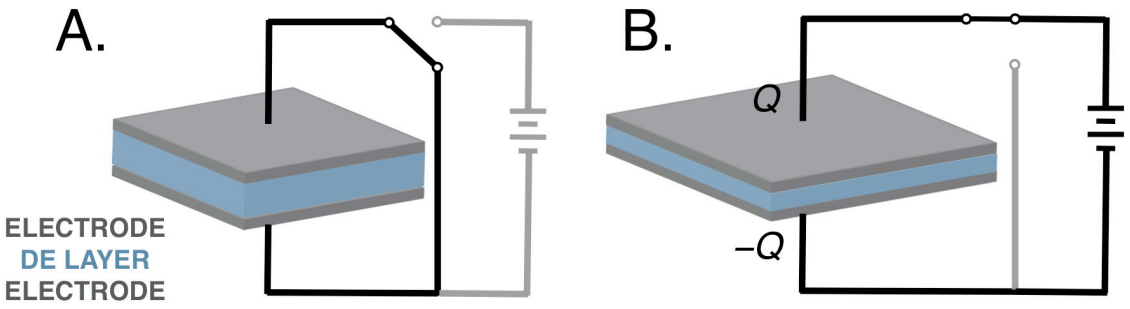

Figure 1.11 Schematic of a DE actuator. In (A), there is no electric field present and the DE layer is at rest. In (B), an electric field is applied across the electrodes and the DE layer is deformed.

Since the elastomer is anchored to the electrodes, at least one of the electrodes must have a high degree of compliance, *i.e.* be able to move and stretch in order for energy to be efficiently transduced between the electric field and the elastomer. Pelrine and co-workers described the ideal electrode material for DE actuator fabrication as one that is highly conductive, perfectly compliant, patternable, and able to be constructed as a very thin layer or coating.[85] It is highly desirable for the electrode material to be at least as compliant as the DE layer in order to provide optimal energy coupling between the electric field and the DE. While evaporated or sputtered metallic electrodes have high conductivity and reproducibly small thicknesses, these electrodes are not ideal because their elastic moduli are 3 to 5 orders of magnitude larger than those of elastomers. Therefore, they can only withstand strains of approximately 2 to 4% before cracking results in the irreversible loss of conductivity. More compliant electrode materials, including graphite powder[85, 86], graphite spray[86], carbon fibers[85], carbon grease[86, 87], silver grease[88], electrolyte solutions[86], ionically conductive polymers[85] and ion-implanted electrodes[89, 90], have been successfully implemented in DE actuators. All of these electrode materials have different physical and electrical properties, which may make the use of one advantageous over the others

for a specific application. Carpi and co-workers evaluated the use of four different electrode materials and saw that the choice of electrode material significantly contributed to the performance of the actuator.[86] The authors attributed these results to the ability of different electrode materials to hold different amounts of charge per unit area, but the lack of perfect compliance may also be a significant factor, as stiffer electrodes will resist actuation.

Electronically, this configuration is represented by a parallel plate capacitor where the DE is the dielectric. If the area of the capacitor is significantly larger than the thickness of the DE layer, fringing effects from the electric field can be ignored. When an electric field is created between the electrodes, it creates a separation of charge with positive charges on one side of the DE layer and an equal number of negative charges on the other side. The coulombic forces between the charges in this system act on the DE layer in two ways. First, unlike charges on opposite surfaces of the DE create an attractive force parallel to the electric field, which seeks to compress the elastomer in the *z*-direction. Second, the presence of like charges on the surface of each electrode produces a repulsive force perpendicular to the electric field, which acts to stretch the elastomer in both the *x*- and *y*-directions. Both of these aspects of the DE deformation can be seen in Figure 1.11b. For the sake of notation, the direction parallel to the electric field is the longitudinal direction and the direction perpendicular to the field is the transverse direction.

In addition to the simple, planar configuration that was described above, many different DE actuator configurations have been fabricated in the quest to improve the magnitude of the actuation magnitude and to produce a variety of motions. For instance, multiple electrode-DE units can be stacked on top of one another in order to increase the total deformation.[85] Roll[74, 91] and tube[85, 92] configurations have been used to convert the relatively insignificant compressions of planar actuators into more significant elongating strains. Unimorph and bimorph configurations use non-uniform strains to produce bending motions on a planar substrate.[85, 93] Lastly, diaphragm configurations fix a planar DE element to a rigid frame that impedes transverse strain.[71, 93] Instead of just a simple compressing motion, the diaphragms create a "bulging" motion when the DE is actuated.

1.4.3. Energy, Stress and Strain in DE Actuators

1.4.3.1. Capacitance and Energy

As mentioned previously, a DE actuator is electronically equivalent to a parallel plate capacitor. A capacitor is a simple device that stores energy when charges are separated between the two plates, or electrodes. That is, when charge Q exists on one electrode and a complimentary charge $-Q$ exists on the other. The energy is stored in the electric field that exists between the two plates as a result of the potential drop across them. The energy can be stored in the capacitor until it is discharged, at which point it can be used to perform work in the system. The capacitance defines how much charge a capacitor can hold for a given potential drop across the plates. Therefore, the capacitance (C) of a DE actuator is calculated as:

$$C = \frac{Q}{V_{cap}} = \frac{\varepsilon_0 k A_0}{z_0} \tag{1.28}$$

where V_{cap} is the potential drop across the DE layer, ε_0 is the permittivity of free space, k is the dielectric constant of the elastomer, A_0 is the active or overlap area of the electrodes and z_0 is the distance between the electrodes, *i.e.* the native thickness of the DE layer.

When charged, the total electrical energy stored in the capacitor (U_e) is defined as:

$$U_e = \frac{Q^2}{2C} = \frac{z_0 Q^2}{2\varepsilon_0 k A_0} \tag{1.29}$$

This energy is important because it represents an upper limit to the amount of mechanical work that can be done on the DE layer by the electrical field. When work is done on the DE layer by the electrical field during capacitor charging, the conformational changes dz and dA occur. From this point on, the physics of these systems will be described only for the case of a DE unit operating in actuator mode. The DE unit can also be operated in generator mode, in which work is done on the field by an external force acting on the DE layer, but that specific case is not of interest for this thesis. By looking at Equation 1.29, it becomes obvious that a change in active area and DE thickness results in a change in the energy of the capacitor. As seen in Equation 1.30, the change in energy (dU_e) for the actuator is a sum of two actions.[94]

$$dU_e = \left(\frac{Q}{C}\right)dQ + U_e\left[\left(\frac{1}{z_0}\right)dz - \left(\frac{1}{A_0}\right)dA\right] \tag{1.30}$$

The first term in this equation represents the amount of electrical energy that flows into the capacitor from an external source. In actuator mode, this source is a high-voltage power supply. The second term represents the amount of energy that is converted from the electric field into mechanical work. Since elastomers are assumed to be incompressible materials, the volume of the DE layer remains constant as the capacitor is charged ($A_0 z_0 = Az$). Taking his into account, Equation 1.30 can be simplified into either of the following equations:[94]

$$dU_e = \left(\frac{Q}{C}\right)dQ - 2U_e\left(\frac{1}{A_0}dA\right) \tag{1.31$_1$}$$

or,

$$dU_e = \left(\frac{Q}{C}\right)dQ + 2U_e\left(\frac{1}{z_0}dz\right) \tag{1.31$_2$}$$

It is evident from these equations that as the DE layer compresses longitudinally ($dz < 0$) and expands transversely ($dA > 0$), the change in electrical energy in the capacitor decreases. This decrease symbolizes the conversion of electrical energy to mechanical energy in the system.

1.4.3.2. Electrostriction

When in the presence of an electric field, polar molecules will reorient themselves such that partial positive charges and partial negative charges minimize their distance to the electrodes with $-Q$ and Q charge on them, respectively. This realignment creates an electric field that opposes the field between the electrodes. The magnitude of the induced electric field is dependent upon the polarizability of the DE layer. With a non-polar polymer, the electrical domains of the polymer are randomly aligned in the absence of an electric field. When an electric field is applied, the formation of dipole moments causes reorientation of the electrical domains and multiple segments of the backbone synchronously flex. The realignment of non-polar molecules in an electric field can be seen in Figure 1.12.

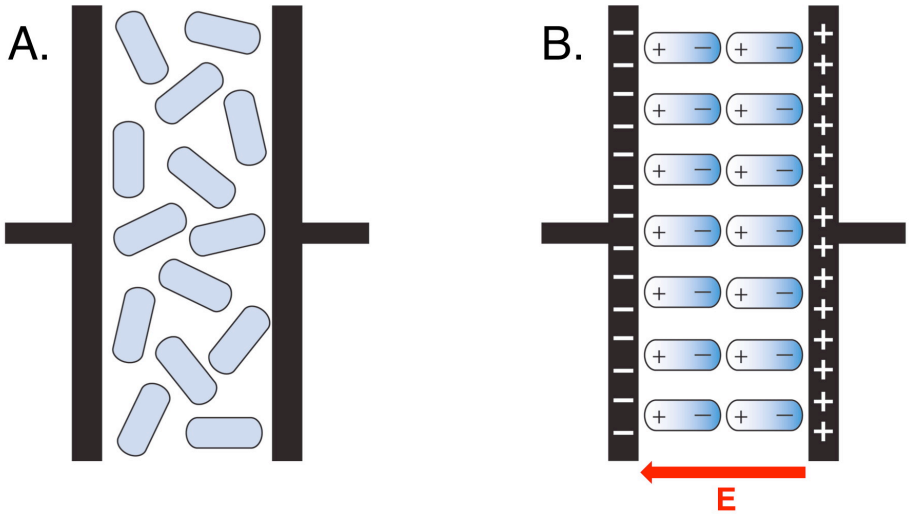

Figure 1.12 The alignment of non-polar molecules acting as the dielectric in a parallel-plate capacitor. In the absence of an electric field, the molecules are randomly aligned (A). When a field is applied, the molecules line up in the field according to their induced dipole moments (B).

The strain (S) that the DE layer undergoes during this realignment process is defined as:[77]

$$S = Q_s P^2 \tag{1.32}$$

where Q_s is the charge-related electrostrictive coefficient and P is the polarization of the material. For a linear dielectric polymer, the polarization is defined by the following equation:[77]

$$P = \left(\varepsilon - \varepsilon_0\right) E_{cap} \tag{1.33}$$

where ε is the relative permittivity of the DE layer, which is the permittivity of free space (ε_0) multiplied by the dielectric constant (k). Since the polarization is directly proportional to the magnitude of the electric field, when Equations 1.32 and 1.33 are combined, it is evident from the resulting expression (Equation 1.34) that the electrostrictive strain has a quadratic dependence upon the electric field.[77]

$$S = Q_s \left[\left(\varepsilon - \varepsilon_0\right)^2 E_{cap}^2\right] = M E_{cap}^2 \tag{1.34}$$

In this expression, M is known as the electric field-related electrostrictive coefficient. While all polymers are subject to electrostriction in the presence of an electric field, insulating polymers like DEs typically experience only small strains due to their low polarizability. Moreover, DEs

do not exhibit linear dielectric behavior, so the quadratic relationship between S and E_{cap} in Equation 1.34 does not hold for all values of E_{cap}.

1.4.3.3. Maxwell Stress

In addition to electrostriction, the dielectric experiences conformational changes due to the coulombic forces that are present once charges have accumulated on opposite sides of a charged capacitor. As mentioned previously, the coulombic forces in this system act simultaneously to compress the DE longitudinally and stretch it transversely. The amount of stress generated between the two electrodes, called Maxwell stress and designated as p (pressure), is defined as:[85]

$$p = k\varepsilon_0 E_{cap}^2 = k\varepsilon_0 \left(\frac{V_{cap}}{z_0} \right)^2 \tag{1.35}$$

The Maxwell stress generated in a DE unit is twice the amount of force generated by a parallel plate capacitor with fixed, rigid electrodes. This is because the compliant electrodes in the DE unit allow the longitudinal compression to be coupled directly with the transverse stretching. Analogous to electrostriction, the Maxwell stress is quadratically proportional to the magnitude of the electric field. For a linear, isotropic solid with no mechanical constraints, the strain that the DE layer experiences as a result of these forces is defined as:[85]

$$S = -sp = -\frac{k\varepsilon_0}{Y} E_{cap}^2 \tag{1.36}$$

where s is the elastic compliance of the polymer, which is also the inverse of the Young's modulus (Y). The strain produced as a result of Maxwell stress is the dominant actuation mechanism for DEs since they possess large elastic compliances. The negative sign in this expression simply denotes that this is a compressive strain in the longitudinal direction. The strain described in Equation 1.36 represents and Hookean response to stress, in which the Young's modulus acts as the spring constant of the material. Based on experimental data, this model accurately describes the relationship between stress and strain for elastomers only at infinitesimal strains. At finite strains, the Hookean model breaks down as elastomers tend to increasingly resist compressive strains and become more responsive to tensive strains. Indeed, the physical response of the DE to stress is very complex since the Young's modulus of an

elastomer changes as a function of strain.[70, 95] In order to more accurately describe the non-linear behavior of elastomeric materials under stress, the Neo-Hookean, Mooney-Rivlin[95] and Ogden[96] models have been developed.

The model that is most frequently used to describe the behavior of elastomers under stress is the Mooney-Rivlin model. The general relationship between stress and strain can be described by the following equation:[97]

$$p = \left(C_1 + \frac{C_2}{\lambda}\right)\left(\lambda - \frac{1}{\lambda^2}\right) \tag{1.37}$$

where C_1 and C_2 are constants and λ is the extension ratio. The extension ratio is defined as the ratio of the strained polymer thickness (z) to the length of the resting polymer thickness (z_0). This term is related to the strain by the following equation:

$$S = \lambda - 1 \tag{1.38}$$

By combining Equations 1.35 and 1.37, we see that as an electric field is applied across the DE layer λ deviates from unity, signifying deformation of the polymer. The constants C_1 and C_2 have to be experimentally determined for a given elastomer material, but values for silicones commonly lie between 0.3 to 1.2 ($\times 10^5$ Pa) for C_1 and 0.3 to 1.1 ($\times 10^5$ Pa) for C_2.[98] Figure 1.13 shows three different models of stress-strain behavior for elastomers: the linear Hookean model (red trace) and the non-linear Neo-Hookean (blue) and Mooney-Rivlin (green) models.

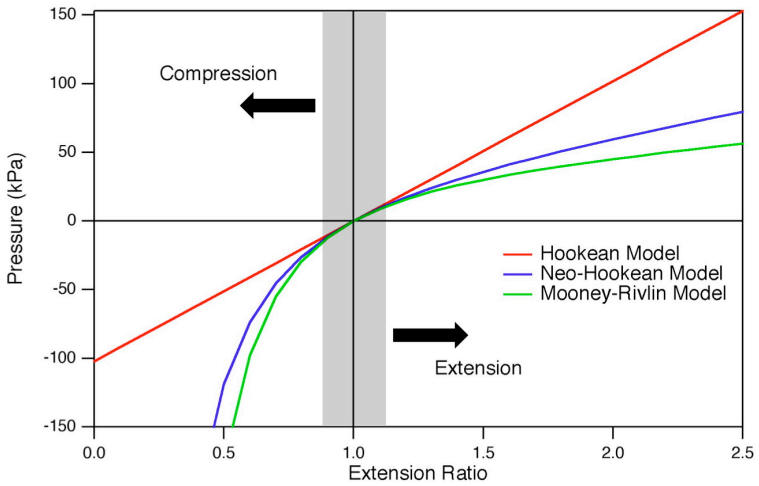

Figure 1.13 Stress-strain behavior according to the Hookean, Neo-Hookean and Mooney-Rivlin models.

The Neo-Hookean model is simply a special case of the Mooney-Rivlin model, in which the first term in Equation 1.37 is replaced by a constant, G, which is the sum of the Mooney-Rivlin constants, C_1 and C_2. All the response curves generated in the above figure were for the same material having C_1 = 17.5 kPa, C_2 = 16.5 kPa, G = 34 kPa and Y = 102 kPa. Data obtained by Gottlieb *et al*.[99] and replotted by Macosko shows that the Mooney-Rivlin model provides a more accurate description of the elastomer response than the Neo-Hookean model does.[95] In Figure 1.13, the region of strain represented by area shaded gray close to $\lambda = 1$ represents infinitesimal strain, where the Hookean model agrees quite well with physical response of the polymer for a given stress.

For the purpose of DE actuation, it is desirable to maximize the amount of mechanical energy converted from a given amount of electrical energy. Although incapable of adequately describing the stress response at finite strains, it is evident from Equation 1.36 that increasing both the dielectric constant and the elastic compliance of the DE layer will more efficiently convert electrical energy to mechanical energy and increase the DE strain. Increasing these variables, however, limits the performance of the actuator in other aspects of its operation, which can be detrimental depending upon he application for which the actuator is used. For instance, increasing the elastic compliance decreases the response frequency of the DE and also produces lower output forces. Likewise, an increase in the dielectric constant of the DE layer decreases its dielectric strength, which limits the magnitude of the electric field that can be applied across the electrodes prior to failure of the DE layer, as will be discussed below.

1.4.3.4. DE Layer Failure and Pre-strain

Unfortunately, there are several modes by which DE actuators can undergo catastrophic failure, *i.e.* be rendered permanently inoperative. Dielectric breakdown, the first of these mechanisms, is due to the insulating nature of DEs. As such, DEs require the use of high electrical potentials in order to produce significant strains. These large electric field strengths are often very close to the dielectric strength of the polymer, which is the largest field strength that a material can withstand before it behaves like a conductor. When the electric field strength exceeds the dielectric strength, electrons bound to the polymer molecules become energetic enough to escape the electron cloud and accelerate towards the positively charged electrode. In doing so, these unbound electrons collide with other electrons, imparting their energy upon them and freeing them in the process. This avalanche of electrons produces an electrical pathway

between the anode and the cathode as a hole is "burned" completely through the DE layer (Figure 1.14).

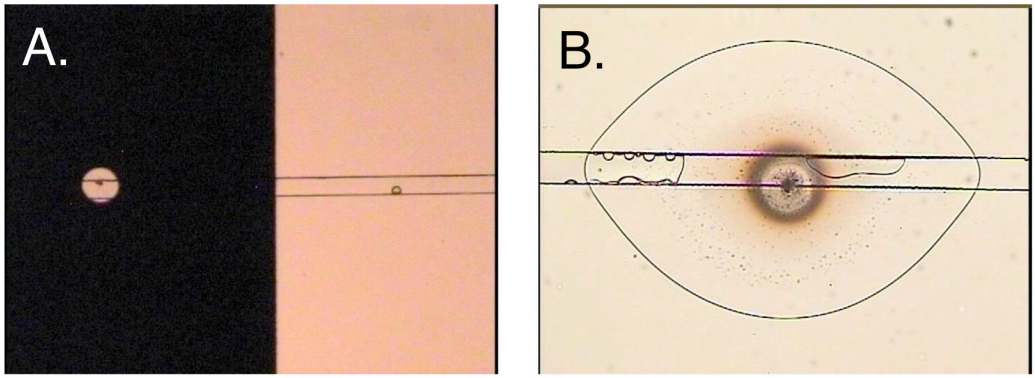

Figure 1.14 Two different examples of DE failure on a microfluidic device caused by dielectric breakdown. The "burn" regions are evident from their circular appearance on both chrome (A) and ITO (B) electrodes. Bubbles are caused by the hydrolysis of water upon DE failure.

In addition to electrical failure, the DE layer can become physically unstable during its operation. For instance, if the Maxwell stress is exceedingly great, the DE layer will be stretched further in the transverse direction than the polymer chains can physically allow and the DE will tear. The above failure mechanism, however, is not very common for DE actuators since elastomers can withstand strains in excess of 300%. Instead, a phenomenon called "pull-in" failure is more likely to occur during actuation. As the DE layer is compressed in the longitudal direction, it will collapse in on itself should the Maxwell stress become greater than the restoring force of the dielectric. At this point, a pull-in failure will resemble dielectric breakdown since the thickness collapse will cause a huge increase in the electric field strength across the DE. According to the Hookean model, this type of failure becomes prevalent as the thickness strain in the DE layer approaches -33%.[94] However, the tendency for elastomers to resist increasingly compressive stresses allows for greater thickness strains to be achieved without failure. Lastly, isolated instances of dielectric breakdown at electric field strengths lower than the dielectric strength are indicative of local regions in the DE layer where the compression is greater than the surrounding polymer matrix. This may be evidence for the presence of cavities, impurities or other types of defects that produce local electric field anomalies.

One way in which dielectric breakdown can be limited is by pre-straining the elastomer during operation. This has been done previously by stretching the DE across a rigid frame,

where it is fixed.[75] It has been shown that pre-straining films prior to electromechanical actuation produces a significant increase in the dielectric strength of the DE.[75, 100] While the exact reason for this behavior is currently unknown, it has been suggested that pre-straining the film isotropically (biaxially) and anisotropically (linearly) causes the long-chain polymer segments to align in the plane of the film.[101] This alignment could provide a higher collision cross-section that enables free electrons to be recaptured by polymer strands more effectively at higher field strengths. Moreover, pre-straining the DE layer anisotropically will cause the polymer to effectively stiffen in the high-strain direction. When the DE layer is electromechanically actuated, the transverse extension occurs primarily in the low pre-strain direction. Kofod determined that DE stiffening is only significant at strains smaller than those in the "plateau" region of its stress-strain response curve.[102] Furthermore, he showed that pre-strain does not affect the electromechanical coupling of the actuator, so any enhancements in performance are related to the change in the dielectric strength and the physical dimensions of the actuator.[102]

1.5. Integrating Smart Technology and Microfluidics

While more and more processes have been integrated on microfluidic devices, the way in which researchers interact with the microchip has remained the same. That is, the mechanisms for performing operations within the channel network are often external to the microchip platform and require "access ports" similar to the chemical reagents. The reliance upon large, off-chip equipment prohibits the development of self-contained, portable systems that can be used for "point-of-care" analysis. The angle that we have chosen to pursue in an attempt to reduce the footprint of miniaturized analysis systems is based upon the exploitation of PDMS as a smart material. The use of smart materials and smart technology in conjunction with microfluidics is beneficial because these technologies each seek to streamline the operating process and conserve the resources necessary for operation.

Chapter 2 - Demonstration of an Integrated Electroactive Polymer Actuator on a Microfluidic Electrophoresis Device

Reproduced in part by permission of the Royal Society of Chemistry.
Published as: Price, A. K.; Anderson, K. M.; Culbertson, C. T. *Lab Chip* **2009**, *9*, 2076-2084.

Reproduced in part by permission of the American Chemical Society.
Published as: Price, A. K. and Culbertson, C. T. *Anal. Chem.* **2009**, *81*, 8942-8948.

2.1. Introduction

The construction of microfluidic devices incorporating siloxane-based polymers is widely reported in the current literature. The growth in the use of PDMS for microfluidic applications has been driven by its ready commercial availability, its low cost, and its ease and quickness of fabrication. However, it is the high elasticity of PDMS that makes it the polymer of choice in devices that feature integrated actuation systems for fluid manipulation. Actuators are becoming an increasingly popular component of micro-Total Analysis Systems (μ-TAS, or microfluidic devices). Their popularity stems from the desire to fully integrate multiple fluid-handling architectures on a single device in order to perform multi-step analyses. To date, numerous devices that incorporate pneumatic,[9, 10, 103] thermopneumatic,[104] piezoelectric,[105, 106] shape memory alloy,[107] electrothermal,[108, 109] electrochemical,[110] electrostatic[111, 112] or magnetic actuation[113] have been demonstrated. The majority of these actuation systems derive their function from the reversible deflection of a polymer membrane, which produces a volume change in a portion of the native channel network. Thus, these miniaturized actuators have found use as microvalves and micropumps. However, each of the aforementioned actuation methods commonly suffers from a variety of problems, including complicated and expensive fabrication techniques, a dependence upon large, off-chip equipment, high power consumption, slow response times and limited effectiveness.

While it seems that an overwhelming number of actuator-microchip couplings have been demonstrated to this point, the ability of PDMS to function as a smart material has not been commonly exploited along with its fluid-handling capabilities. To our knowledge, there have

only been two reports in the literature that investigate electroactive DE actuation configurations in order to perform operations on microfluidic devices. Loverich *et al*. developed a pump based on the operation of a pre-strained acrylic diaphragm actuator that was integrated with a PDMS microfluidic network.[87] Actuation of the DE unit resulted in a downward displacement of the top half of the diaphragm, which caused the microfluidic compression chamber to increase in volume. This pump was capable of producing flow rates up to ~ 80 μL/minute and self-priming from an initial dry state. The main disadvantage with this configuration is that the device fabrication is exceptionally complicated. Also, repeated actuation over time resulted in dielectric failure or it caused the carbon grease electrode inside the actuator balloon to shift, which caused a break in electrical connectivity. Sadler *et al.* described and modeled a configuration that featured a linear array of patterned electrodes that are fabricated inside a microfluidic channel but separated from the fluid by a thin (~ 50 nm) PDMS film.[114] The thickness of the film changes as a result of AC fields applied between adjacent electrodes. These high-frequency AC waveforms can be ordered to produce fluid pumping or randomized in order to induce fluid mixing. However, it is not evident that a prototype device with this actuator configuration has ever been fabricated or tested.

In this chapter, we introduce a microfluidic device that incorporates a novel integrated DE actuation (IDEA) unit. The general hypothesis is that a channel filled with an electrolyte buffer is capable of acting as one of the electrodes necessary for forming a capacitor. By applying and removing an electric field across the DE between a patterned electrode and the electrolyte-containing channel, actuation and relaxation of the DE film will generate a volume change in the fluidic channel opposite the patterned electrode. Our device consists of a PDMS fluidic layer, a thin, capacitive PDMS DE layer and a patterned electrode base. As a proof of concept, we demonstrate the operation of an IDEA and evaluate its physical performance by producing injections for electrophoresis on a standard cross channel architecture (Figure 2.1). As opposed to conventional gated injections,[115] in which the potentials applied to multiple reservoirs are changed at programmed intervals, the injections on our device originate from the change of a single potential applied to a patterned electrode that is isolated from the channel network.

2.2. Materials and Methods

2.2.1. Chemicals

Sodium borate was obtained from Fisher Scientific (Pittsburgh, PA). Sodium dodecyl sulfate (SDS) was obtained from Sigma Chemical Co. (St. Louis, MO). 2',7'-dichlorofluorescein (DCF) was obtained from Acros Organics (Morris Plains, NJ). PDMS (Sylgard 184 and Sylgard 527 silicone elastomer kits) was obtained from Dow Corning (Midland, MI). All of these chemicals were used as received. The distilled, deionized water used to prepare every solution was purified with an E-pure system (Barnstead, Dubuque, IA). Solutions were filtered immediately before introduction to the microchip reservoirs using syringe-driven 0.45 mm PVDF filters (Fisher Scientific).

2.2.2. Microchip Fabrication

2.2.2.1. Masks

The photomasks necessary for device fabrication were produced by a photoplotting process at 40,000 dpi (dots per inch) by Fineline Imaging (Colorado Springs, CO). The mask designs were created in AutoCAD2006LT (Thompson Learning, Albany, NY) and sent to the manufacturer for production. For this study, two sets of masks were used – one mask for the fabrication of the fluidic network and then a series of masks that were used to create chrome electrodes of different dimensions. The mask used for the fabrication of the channel network consists of two intersecting lines with widths of 50 μm and lengths of 6 cm. These lines intersect such that two arms of the resultant cross have lengths of 1 cm and the other two have lengths of 5 cm (Figure 2.1). The other masks consisted of electrode patterns that possessed widths of 3 mm and lengths of either 1 mm, 5 mm, 10 mm, 25 mm or 40 mm. These lengths defined electrodes that produced active capacitor areas of approximately 0.05, 0.25, 0.5, 1.25 and 2 mm^2 on the DE film when coupled with the channel dimensions.

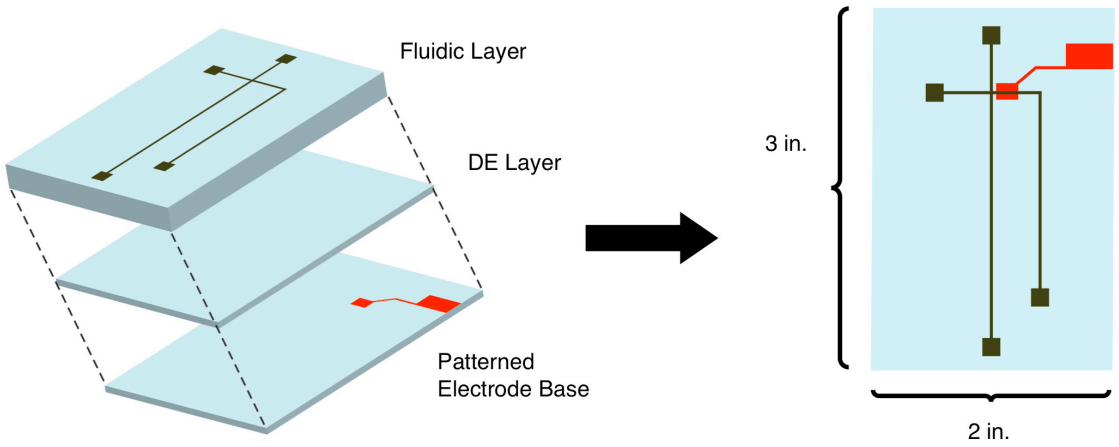

Figure 2.1 Illustration showing the three layers that comprise an IDEA-µCE device.

2.2.2.2. Electrode Fabrication

4 x 4 inch photomask blanks (Telic Co., Valencia, CA) were used to fabricate the electrode bases. These blanks are white crown glass substrate (0.9 mm thick) coated with 120 nm of chrome and 530 nm of AZ1500 positive photoresist. A 40K dpi photomask displaying the desired electrode pattern was placed on top of the blank and then exposed to approximately 200 mJ/cm^2 of UV radiation from a near-UV flood exposure system (Newport Oriel, Stratford, CT). After development of the weakened photoresist, the slide was placed in an acidified ceric sulfate solution until the unprotected chrome was etched away. After rinsing with copious amounts of water, the electrode base was rinsed with (in order) ethanol, acetone and ethanol again to remove the remaining photoresist. Due to the size of the original photomask blank, two different electrode bases could be fabricated simultaneously. A dicing saw (Sherline model 5410, Vista, CA) was used to cut the blank into two 2 x 3 inch slides containing electrodes.

2.2.2.3. SU-8 Mold Fabrication

The fabrication of molds using SU-8 photoresist was based on previously published methods.[34] Briefly, a 4 inch silicon wafer (Silicon Inc., Boise, ID) was coated with SU-8 2010 negative photoresist (MicroChem Corp., Newton, MA) using a spin-coater (Laurell Technologies, North Wales, PA). The SU-8 was spun at 500 rpm for 5 seconds followed by 1000 rpm for 30 seconds. The photoresist was baked on a hotplate at 90 ºC for 5 minutes prior to UV exposure. An exposure dose of ~ 180 mJ/cm^2 using a near-UV flood exposure system was

delivered to the substrate through a negative mask containing the channel pattern. Following this exposure, the wafer was baked at 90 ºC for 5 minutes and developed in propylene glycol monomethyl ether acetate (PGMEA). This protocol produces SU-8 structures that are approximately 20 µm tall. The thickness of the photoresist was measured with a XP-2 profilometer from Ambios Technology (Santa Cruz, CA) and this structure height corresponded to the depth of the resulting PDMS channels.

2.2.2.4. Device Fabrication

To produce a device with a DE layer approximately 40 µm thick, a 20:1 or 10:1 (w/w, elastomer base/curing agent) PDMS (Sylgard 184) mixture was poured onto an electrode base and spun at 2000 rpm for 45 seconds. To produce a DE layer the same thickness with a 3:1 mixture of Sylgard 527/Sylgard 184, the activated polymer was poured onto an electrode base and spun at 1000 rpm for 45 seconds. Also, a 10:1 PDMS mixture was poured onto the mold containing the fluidic channels. Both of these PDMS segments were allowed to partially cure for less than 15 min at 80 °C. At this time, the PDMS layer containing the fluidic channels was peeled off of its mold and aligned over the PDMS layer covering the electrode such that the patterned electrode (abbreviated PE in Figures) was directly below a portion of the sample waste channel near the intersection (Figure 2.2c). The two layers were brought into conformal contact, and cured together at 80 °C for at least 1 hour. Afterwards, reservoirs were punched in the PDMS to allow access to channels, glass reservoirs were attached and a wire was epoxied onto the device to provide electrical contact between the chrome electrode and a high-voltage power supply. Colloidal silver (Ted Pella, Inc., Redding, CA) was applied to ensure electrical contact between the wire and the patterned electrode.

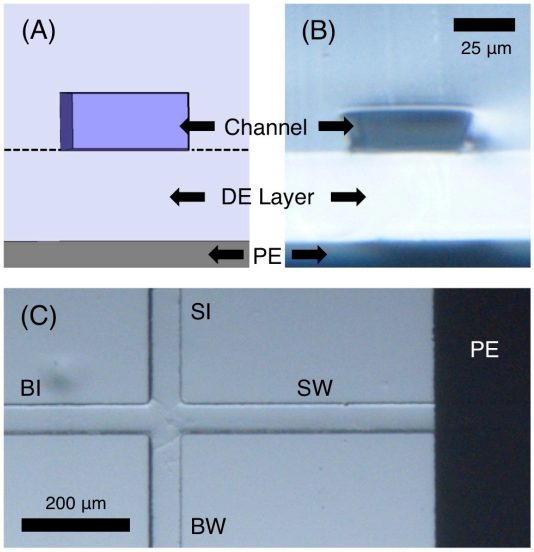

Figure 2.2 Panels (A) and (B) show a cross-sectional illustration and micrograph that depict the configuration of the DE layer and the channel. Panel (C) shows a micrograph of the intersection area.

2.2.3. Microscopy

The thickness of the DE layer was measured by visualizing a cross-section of the PDMS component (Figure 2.2b) of the device on a Nikon SMZ1500 stereomicroscope (Nikon Instruments Inc., Melville, NY). Images were captured using a Nikon Digital Sight camera and analyzed using Nikon ACT-2U software. For recording injection sequences, the microchip was placed on the stage of a Nikon Eclipse TE2000-U inverted microscope. Voltages were applied to the fluid reservoirs through platinum electrodes connected to a Bertan high-voltage (0-10 kV) power supply (Hauppauge, NY). The HV power supply consists of five separate units that are independently controlled by Labview software (National Instruments, Austin, TX). An epiluminescence system consisting of a mercury arc lamp and Nikon B-2A filter block were used to produce 450-490 nm light. The light was focused on the cross chip intersection with a 10 × objective (Nikon) and the subsequent fluorescence emission was collected with that same objective and captured by a high resolution Sony CCD color video camera. Movies were recorded and analyzed using Roxio Videowave movie creation software.

2.2.4. DE Elasticity Determination

Elasticity measurements were performed on rectangular sections of polymer 2.5 cm long with a uniform cross-sectional area as previously reported.[116] Briefly, one end of the polymer was attached to the ceiling and mass was added to the other end of the polymer until either the polymer sheared or the attachment clips failed. Compressive elasticity was assumed to be roughly the same as tensile elasticity.

2.2.5. Separation and Detection

2.2.5.1. Electrophoresis Parameters

The microchip channels were prepped only with the run buffer. The run buffer used in all experiments consisted of 5 mM sodium borate with 1.5 mM SDS (pH = 9.2). Voltages were applied to the sample introduction (SI) and buffer introduction (BI) reservoirs according to Kirchoff's current laws and the buffer waste (BW) and sample waste (SW) reservoirs were connected to ground. Injections were made solely by altering the potential applied to the patterned electrode while the potentials applied to the buffer and sample intro reservoirs were held constant. The response of the fluid flow to the charging and discharging of the capacitor has been investigated visually on the inverted microscope. The potential drop across the DE layer, V_{cap}, is expressed by the following equation:

$$V_{cap} = V_{pe} - V_{channel} \tag{2.1}$$

where V_{pe} is the potential that is applied to the patterned electrode and $V_{channel}$ is the average potential that exists in the channel above the electrode. The potential is dependent upon the potentials applied in the buffer and sample reservoirs (Figure 2.3). In order to have a negligible electric field across the DE layer, V_{pe} was held roughly equal to $V_{channel}$. This condition represents the uncharged or discharged state of the EAP capacitor. Increasing or decreasing V_{pe} a predetermined amount produced the charged state of the DE capacitor. Due to the fact that $V_{channel}$ is a non-zero value, V_{cap} can be either positive or negative without changing the polarity of the high voltage power supplies.

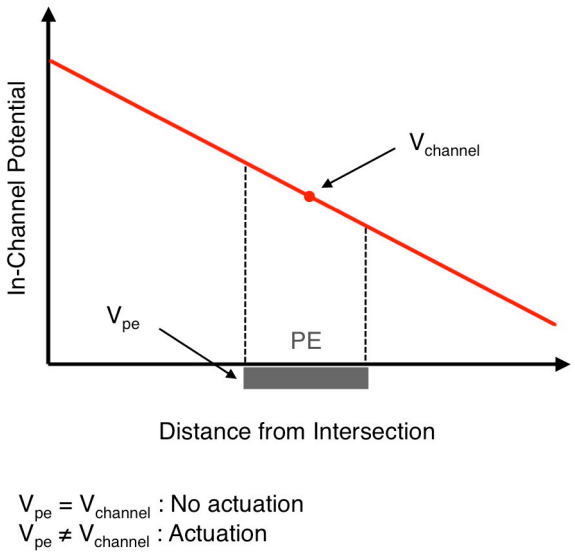

Figure 2.3 Graphical representation of how the in-channel potential decreases from the intersection to the sample waste reservoir. $V_{channel}$ is calculated as the average potential in the channel above the patterned electrode.

2.2.5.2. Single-Point Detection Apparatus

A 10 mW Nd:YAG laser (BCL-010, CrystaLaser, Reno, NV) that produced light at 473 nm was used as the excitation source in these experiments. The laser beam was reflected off of a 500 nm long pass dichroic mirror (Omega Optical, Brattleboro, VT) and focused through a 40 × objective (Creative Devices, Neshanic Station, NJ) into the microchip. The microchip was immobilized on a plexiglass holder (made in-house) that was mounted on a 1-inch *x*-*y* translation stage working in tandem with a *z*-axis optical holder for the objective (Thor Labs, Newton, NJ). Fluorescent emission was collected back through the objective and passed through the dichroic mirror. Prior to detection, the light was spatially and spectrally filtered using a 400 mm pinhole and a 545 nm bandpass filter (Omega Optical). Light intensity was transduced with a photomultiplier tube (Hamamatsu, Bridgewater, NJ) and the resulting current was amplified with a low noise current preamplifier (Stanford Research Systems, Sunnyvale, CA) using an electronic low pass filter. Data was sampled at rates between 250 and 750 Hz using a PCI-6036E multifunction I/O card (National Instruments) in a computer. All of the optical components, the microchip platform and the PMT were housed in a light-excluding box (80/20 Inc., Columbia City, IN).

A high-voltage power supply, which was made by the Electronics Design Laboratory at Kansas State University, supplied the necessary potentials to the IDEA-μCE devices. The power supply consisted of three separately controlled high-voltage units, which were each capable of producing up to 6 kV. Control of the high-voltage units and data acquisition was accomplished with a Labview software program that was written in-house. Finally, all data analysis was performed using both a Labview program written in-house and Igor Pro software (Wavemetrics, Portland, OR).

2.3. Results and Discussion

2.3.1. Analyzing the Electrical Properties of the System

In all of the experiments, a separation field strength of ~ 500 V/cm was used. To accomplish this, 3160 V was applied to the BI reservoir and 2800 V was applied to the SI reservoir (Figure 2.4a). Both of the waste reservoirs were connected to ground. In accordance with Kirchoff's and Ohm's laws, the potential present at the channel intersection was approximately 2475 V (less than ± 5% error) with this configuration. To a first approximation, $V_{channel}$ was calculated as the average potential present in the sample waste channel across the length of the patterned electrode (Figure 2.3). This calculation assumed that the voltage in the channel dropped 500 V per centimeter between the intersection and sample waste reservoir. For devices with capacitor areas of 0.05, 0.25, 0.50, 1.25 and 2.00 mm^2 we used $V_{channel}$ values of 2480, 2360, 2240, 1840 and 1480 V, respectively. Figure 2.4b shows the microfluidic network of the IDEA-μCE device drawn as a circuit diagram. By taking into account the cross-sectional area and length of the channels, the magnitude of the potentials applied to the SI and BI reservoirs and the conductivity of the run buffer, it was determined using Kirchoff's and Ohm's laws that R1 – R5 are on the order of 1 – 600 MΩ with currents between 1 – 5 μA. The capacitance of the IDEAs can be calculated using Equation 1.28, which produced values of 29.3, 147, 293, 733 and 1170 femtoFarads for each of the IDEA areas listed above (assuming an IDEA with $k = 2.65$ and $z_0 = 40.0$ μm).

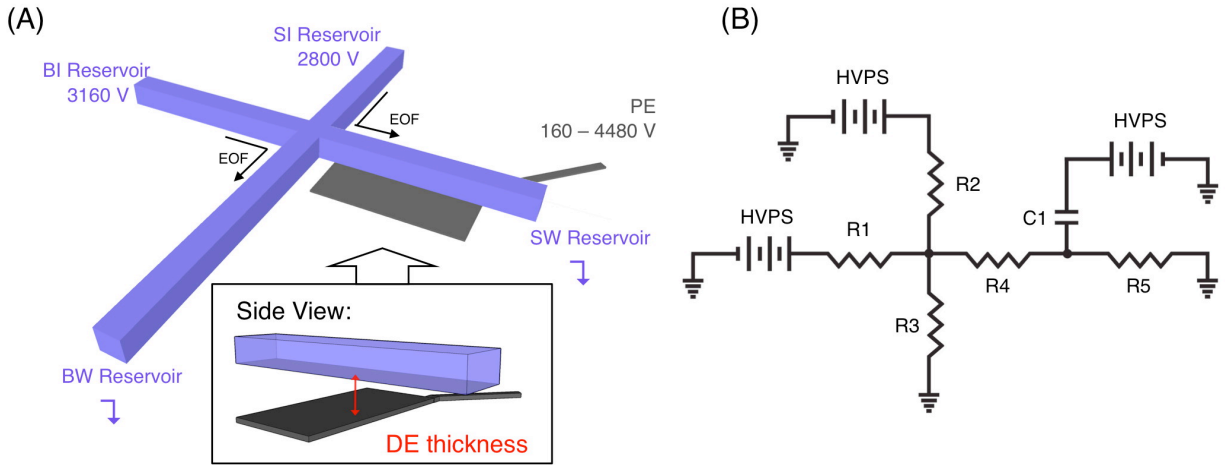

Figure 2.4 (A) Schematic diagram showing the intersection region of an IDEA-µCE device as well as the potentials applied to the reservoirs and the patterned electrode. (B) Simple circuit diagram of the IDEA-µCE device. Each of the microfluidic channels act as resistors and the IDEA acts as a capacitor.

2.3.2. Control of Injections Using IDEA Unit

The illustrations and fluorescence micrographs in Figure 2.5 show the progression of a standard voltage sequence applied to the patterned electrode in order to make an injection. At first, V_{pe} is held roughly the same as $V_{channel}$. In this configuration the IDEA is in its relaxed state since the electric field across it is negligible (time point 1). When V_{pe} is changed and the capacitor is charged, the DE layer is compressed and stretched. The DE deformation results in an increase in the volume of the channel above the actuator and causes additional buffer to be hydrodynamically pulled into the sample waste channel (time point 2). Once the additional volume is filled, the stream paths at the intersection quickly return to their original positions because the linear flow rate of each stream is directly related to the in-channel field strength (Equation 1.17), which does not change significantly when the capacitor is charged. When V_{pe} is changed back to the same voltage as $V_{channel}$, the capacitor is discharged and the DE relaxes back to its original shape. This returns the channel to its original volume, which expels extra fluid into the buffer introduction channel and separation channel (time point 3). Once the excess volume is expelled, the stream paths again return to their original positions. The analyte that is forced into the buffer introduction channel and separation channel is injected (time point 4).

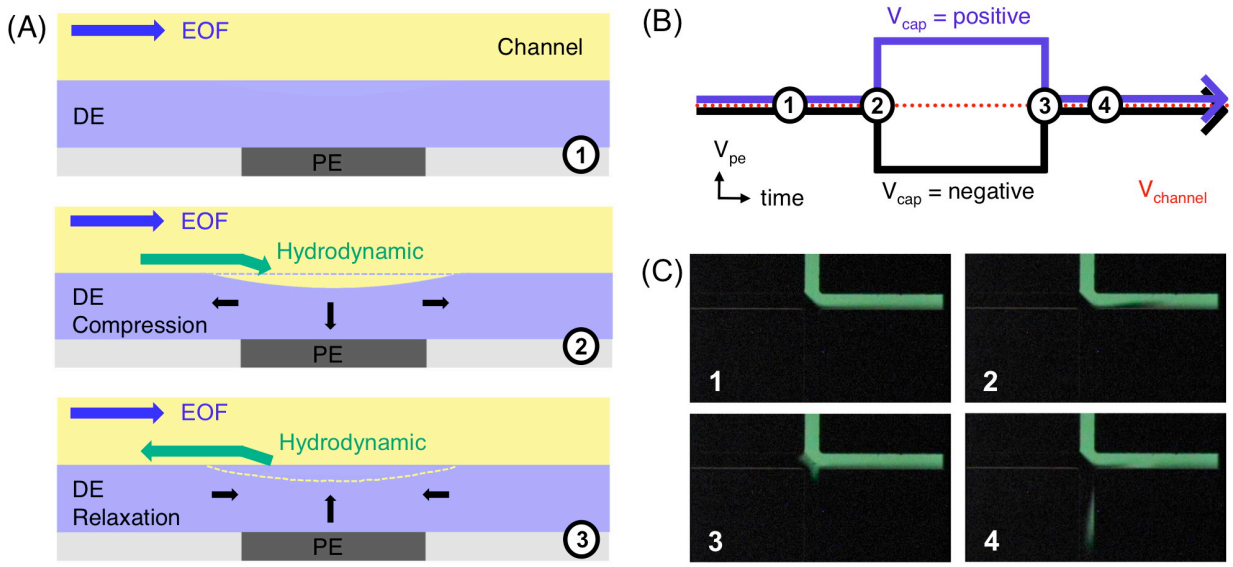

Figure 2.5 Representation of how the potential sequence applied to the patterned electrode (B) produces a hydrodynamic injection. The panels in (A) show how the volume of the sample waste channel opposite the patterned electrode changes as V_{pe} is altered between time points 1 and 3 in (B) as the DE layer compresses and relaxes. Fluorescence micrographs 1-4 in panel (C) show the injection process at each of the time points depicted in (B).

2.3.3. Dependence of Injection Volume on V_{cap} and IDEA Area

To determine how the magnitude and sign of V_{cap} impacted the injection process, a set of experiments was designed in which the injection plug size was analyzed both visually and quantitatively. The fluorescence micrographs in Figure 2.6 were taken on a device with a 20:1 Sylgard 184 DE layer and an IDEA area (A_{el}) of 0.5 mm^2. This IDEA size was chosen because it produced a range of injection volumes that fit nicely within the camera frame. The micrographs of the channel intersection were obtained less than 66 ms (two video frames) after discharging the capacitor, and show the extent of hydrodynamic DCF movement against the electrokinetic flow generated from the BI reservoir. As $|V_{cap}|$ increased, the injections became larger. This progression was due to increasingly larger changes in channel volume that were induced by the application of the electric field across the DE.

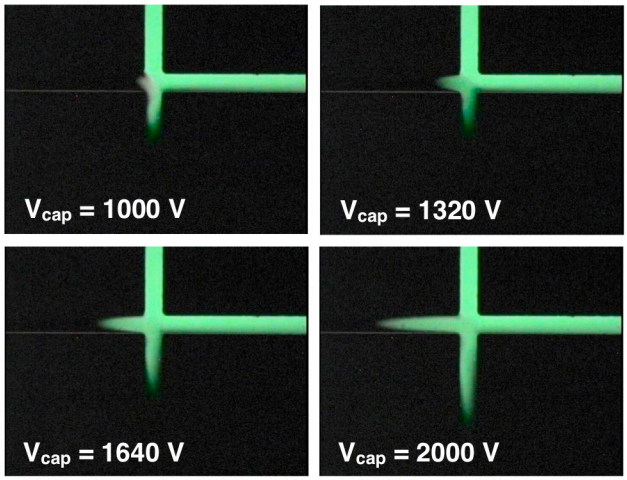

Figure 2.6 Fluorescence micrographs showing the extent of DCF displacement upon the discharging of the capacitor. Potentials where applied across an IDEA with a 0.5 mm^2 area.

To investigate the relationship between injection size and V_{cap} more quantitatively, injections were performed on a single-point laser setup. In the injection sequence, V_{cap} was initially held at approximately zero. After an arbitrary dead time, the capacitor was charged ($V_{cap} \neq 0$) and remained charged for 1 second before being discharged. This sequence was repeated to produce between 3 and 5 injections per run. Peaks of the analyte, a 10 μM DCF solution, were detected 0.508 cm downstream of the intersection. Also, the distance separating the channel intersection and the electrode (Figure 2.2c) was between 450 and 550 microns for every device investigated by single-point LIF detection. For each device with a different IDEA area, two runs of triplicate injections were recorded.

As a simple illustration of performance, Figure 2.7 shows that the response of the actuator (represented by peak area) increases as the magnitude of the electric field across the DE (blue markers) increases. This data was derived from a single run that consisted of 4 injections with successively larger V_{cap} (black trace). As seen in the graph, the peak areas appear to increase quadratically (blue trace) with the magnitude of the electric field that is applied across the DE. This data is consistent with the results that other researchers have observed regarding the relationship between electric field strength and strain for DEs in simple EAP configurations.[71, 85, 117, 118]

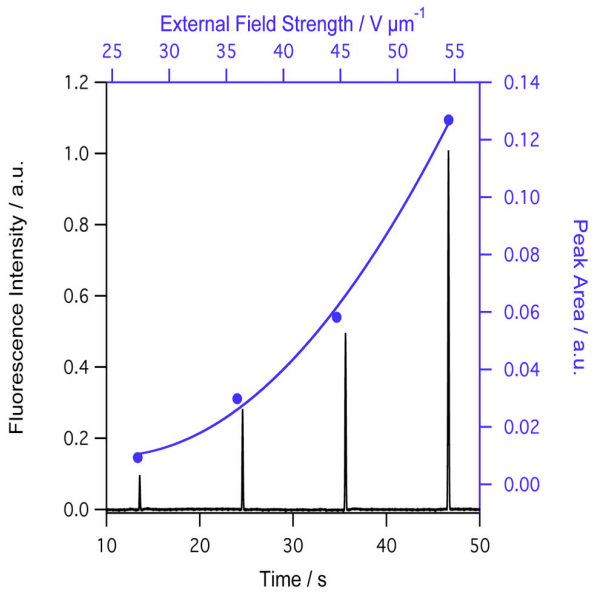

Figure 2.7 The relationship between IDEA response and external field strength. The raw data (black trace) consists of four injections of 10 µM DCF that possess progressively larger V_{cap}. The IDEA consisted of a 3:1 Sylgard 527/Sylgard 184 DE layer and had an area of 0.05 mm^2. Separations were carried out at ~ 500 V/cm with a separation length of 0.5 cm.

Of particular note is that the quadratic behavior we have observed is consistent with data obtained for EAP configurations that use thickened electrolyte solutions as the compliant electrodes.[86] Moreover, this quadratic behavior is also consistent with the Mooney-Rivlin model for thickness strains between 0% and -40%.[70, 95] However, the exact relationship between actuation volume and injection volume is complicated and there are several reasons for this. First, the magnitude of the electroosmotic flow originating from the SI and BI reservoirs opposes the flow of expelled fluid towards the intersection, which limits the amount of analyte injected. Second, the volume of fluid expelled from the actuator region moves toward both the intersection and the sample waste reservoir. Of course, the amount of fluid flow in each direction is highly sensitive to the hydrodynamic resistance in the channel upstream and downstream from the actuator region. Third, we hypothesize that Δz (Equation 1.35) is not uniform across the width of the channel. Investigations into the cross-sectional geometry of the actuated channel region are discussed in Chapter 4. Fourth, the electric field across the DE is not uniform over the entire area of the actuator. This is because the in-channel potential gradient

that produces electroosmotic flow is matched on the other side of the capacitor with a constant voltage at the patterned electrode (Figure 2.3). This means that the average Δz will not be the same on the injection cross side of the actuator as on the SW reservoir side of the actuator.

Figure 2.8 shows how the IDEA response (peak area) behaves as a function of both V_{cap} and IDEA area. Here, the y-axis is plotted as a log value to accentuate the differences between peaks with small areas. For any particular IDEA area, the change in peak area appears to increase quadratically as a function of the electric field across the DE. The peak area is also seen to increase as a function of the IDEA area.

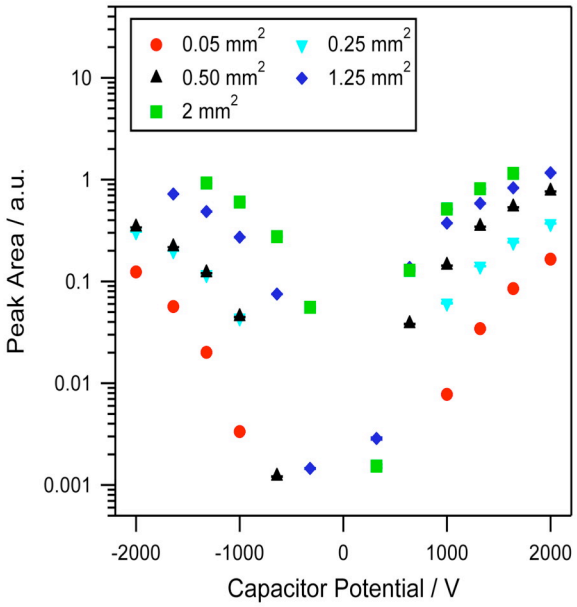

Figure 2.8 The general relationship between IDEA response and the area of the actuator. Peaks of DCF were produced at ~ 500 V/cm and detected 0.508 cm downstream of the intersection. Error bars are included and are smaller than the size of the symbols.

The data in Figure 2.8 also demonstrate two other important characteristics about the device performance. First, the range of voltage drops ($|V_{cap}|$ = 320 to 2000 V) applied to the 1.25 and 2 mm^2 IDEAs generated injection plugs whose volumes could be tuned over approximately 3 orders of magnitude (from 0.0015 to 1.15 peak area units). Second, the positive and negative values of V_{cap} prior to capacitor discharging produced peaks with different areas even though the magnitude of the Maxwell stress should not be dependent on the polarity of the electric field across the DE layer. While the cause of this discrepancy is currently unknown, it may be related

to the fact that PDMS is thought to specifically adsorb anions, and this may affect the inductive charge generation at the surface of this "liquid electrode".

2.3.4. Dependence of Injection Volume on the Elasticity of the DE

In addition to the size of the IDEA area and the magnitude of the electric field across the DE layer, IDEA response was also examined as a function of DE layer composition. Devices were fabricated using three different DE compositions: 10:1 Sylgard 184, 20:1 Sylgard 184, and 3:1 Sylgard 527/Sylgard 184. With these DE compositions, differences in the amount of cross-linking and silica content create polymers that have different amounts of elasticity. Stress-strain curves for the two Sylgard 184 polymer compositions were recorded (Figure 2.9).

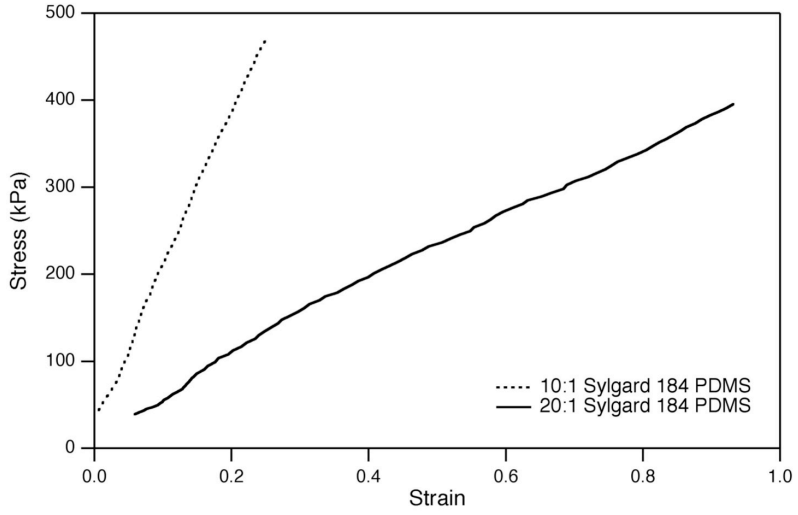

Figure 2.9 Representative stress-strain curves for two compositions of Sylgard 184 PDMS. The first of these (dashed) had a 10:1 of elastomer base to curing agent and the second (solid) had a 20:1 ratio.

At a strain of 10%, it was determined that the 10:1 PDMS had a secant modulus of 2.3 ± 0.3 MPa and the 20:1 PDMS had a secant modulus of 0.52 ± .03 MPa. This means that the 20:1 elastomer is more deformable than the 10:1 elastomer. The secant modulus of the 3:1 Sylgard 527/Sylgard 184 elastomer could not be measured because of its low tensile strength, but a Shore Durometer measurement gave a hardness value of 14 compared to 29 and 58 (all values on scale A) for the 20:1 and 10:1 Sylgard 184, respectively. The results of the Shore Durometer readings show that the 3:1 Sylgard 527/Sylgard 184 composite is the softest material of the three. Galler *et al*. reported that a 13:1 composite of Sylgard 527/Sylgard 184 had a Young's modulus of

0.068 MPa.[119] We expect that the secant modulus of the 3:1 Sylgard 527/Sylgard 184 mixture we used is between 0.52 MPa and 0.068 MPa, making it more deformable than either of the 10:1 or 20:1 PDMS DEs.

Figure 2.10 shows the size of injections on the three devices with different DE layer compositions. Each device had a 0.25 mm^2 IDEA and the intersection-external electrode distance for all three devices was between 460 and 585 microns. In order to examine the effects of DE elasticity on the IDEA response, injections of 20 μM DCF were performed at a field strength of ~ 500 V/cm. This data was obtained by plotting spatial peak variance as a function of migration time for a set of 5 different separation distances. As can be seen in Figure 2.10, the injection size at a specific external field strength varies inversely with the elastic modulus of the dielectric. In addition, the response of IDEAs made from softer elastomers increased more rapidly as a function of electric field strength across the DE layer. These observations are consistent with the predicted relationship between the theoretical thickness strain and the electric field strength for DE layers with differing elasticity.[77, 120]

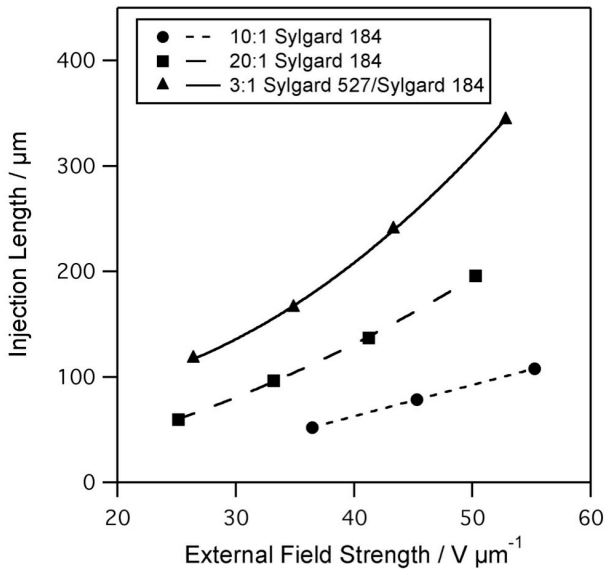

Figure 2.10 The relationship IDEA response and the elasticity of the DE layer. Injections of 20 μM DCF were performed using IDEAs with a 0.25 mm^2 area.

2.3.5. Addressing Alternative Explanations

2.3.5.1. Direct EOF Control

While we fabricated these devices to operate specifically as a DE actuation system, other groups have previously shown the ability to manipulate flow in microfluidic channels using other effects that are generated through the application of electric fields external to the channel manifold.[121, 122] Direct EOF control is a capacitive effect in which charge accumulation at the inner wall of the conduit results in a net change in the surface charge density (Equation 1.16). As such, a shift in the magnitude of the zeta potential alters the EOF velocity of the solution (Equation 1.17). Taken as a whole, the results presented in this chapter indicate that the observed flow modifications are primarily the behavior of an electromechanical actuator as opposed to direct EOF control. In fact, the ability to distinguish whether the externally applied voltage results in actuation of a DE actuator or direct control of the EOF is quite straightforward. First, the magnitude of the effect appears to vary quadratically with V_{cap}/E_{cap} (Figure 2.7 and Figure 2.8). This behavior is consistent with Mooney-Rivlin approximations for EAPs undergoing thickness strains between 0% and -40%. Conversely, the response of the EOF to direct control varies as a function of the inverse hyperbolic sine of V_{pe},[66] which means that the response would approach a constant state as $|V_{cap}|$ is increased. Second, direct control of EOF is not able to affect a significant response in unmodified channels or tubing for solutions with a pH greater than 6.[66] This is due to the fact that the surface charge density at high pH dominates the value of the zeta potential. Our experiments were performed at pH 9.2, which is too great for significant flow alterations by means of direct control. Third, we witnessed a "draw-in" event when the capacitor was charged (time point 2, Figure 2.5) and an injection event when the capacitor was discharged (time point 3, Figure 2.5), regardless of the polarity of V_{cap}. Under direct EOF control, the type of event observed during charging or discharging would change when the polarity of the field is changed, as one would expect an increase in the EOF when V_{cap} is positive and a decrease in EOF when V_{cap} is negative. Fourth, we only observed transient flow modifications during the charging and discharging events whereas with direct EOF control the flow modifications are stable.[123] Fifth, we observed that the response of the actuator is dependent upon the elasticity of the dielectric material separating the channel and the patterned

electrode (Figure 2.10). One would not expect the size of the injections to depend upon the mechanical properties of the channel material with direct control of EOF.

2.3.5.2. Current Leakage

A second form of external electric field effect has been reported where a significant current leakage occurs between two channels on a hybrid PDMS-glass device. The current leakage occurs due to surface irregularities present at the glass-PDMS interface.[124, 125] We do not see any current leakage in this manner as there is no interface that can act as a conduit between the patterned electrode and the channel. Application of an electric field between the channel and the patterned electrode does not change the current measured on any of the electrodes at the termini of the channels or on the patterned electrode (Figure 2.11). Furthermore, the currents required to produce large flow perturbations that Horiuchi and Dutta have observed would generate dielectric breakdown through the continuous DE layer on our IDEA-μCE devices. Dielectric breakdown across the DE will occur on our devices at electric field strengths of ~70 V/μm. Up to the breakdown point where the device fails, current leakage is insignificant.

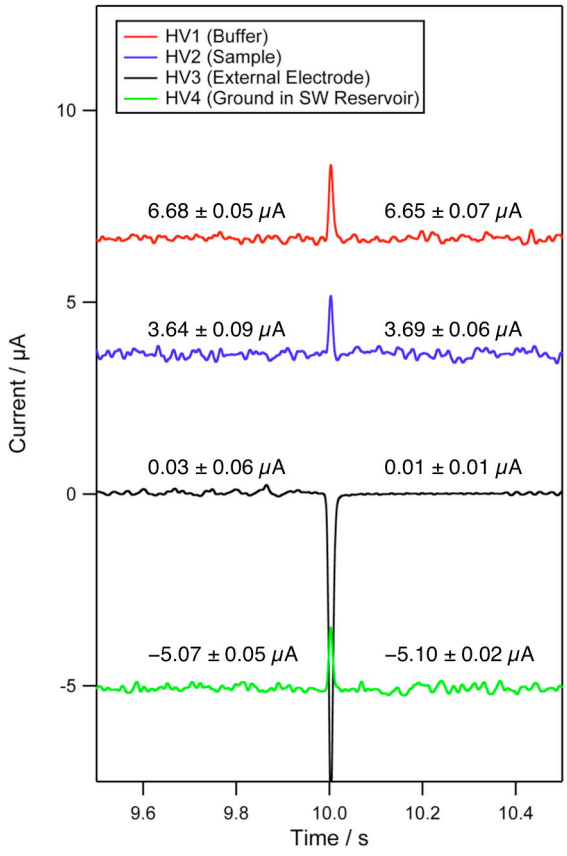

Figure 2.11 Current measurements at 4 different electrodes on an IDEA-μCE device. The IDEA has an area of 0.50 mm^2 and a 20:1 PDMS DE layer. Initially, V_{cap} = 0 V. At t = 10 s, the capacitor is charged such that V_{cap} = -1000 V. The current spikes that occur at t = 10 s are due to the charging of FETs inside of the HV power supply.

2.3.6. Conclusions

A novel method of integrating an electromechanical actuator with a microfabricated fluidic network has been demonstrated. A multi-layer fabrication method is used to create a device in which the fluidic network of the chip is separated from a patterned electrode by a thin DE film, which produces a capacitor. Application of an electric field across the capacitor produces Maxwell stress, which compresses the DE layer and increases the volume of the channel in this region. As a result, buffer is pulled into the sample waste channel. When the capacitor is discharged, the DE layer relaxes back to its original state and fluid from the sample waste channel is expelled into the buffer introduction channel and separation channel. The response of the fluid is fast and it should theoretically behave the same irrespective of whether

the fluid is hydrodynamically pumped, electrokinetically pumped or static, which makes this system well-suited for a wide variety of rapid, integrated processes.

The magnitude of the IDEA response due to the charging and discharging of the capacitor is dependent upon the magnitude of $|V_{cap}|$, the active area of the capacitor, and both the physical and electrical properties of the DE layer. Injections produced on a proof-of-concept μCE device are rapid, reproducible and tunable over a wide range of volume. This IDEA was only used to momentarily modify bulk fluid flow. It is not a pump or a valve but one could envision such designs using this principle. We will report on such actuator functions in the near future. Furthermore, the devices are pseudo-disposable; the fluidic network and dielectric layer can be peeled up and discarded, making these devices amenable to single-use applications.

Chapter 3 - Generation of Nonbiased Hydrodynamic Injections on Microfluidic Devices Using Integrated Dielectric Elastomer Actuators

Reproduced in part by permission of the American Chemical Society.
Published as: Price, A. K. and Culbertson, C. T. *Anal. Chem.* **2009**, *81*, 8942-8948.

3.1. Introduction

Sample introduction is a crucial, yet often overlooked step in chemical analysis. A successful sample introduction method does not introduce significant dispersion and maintains the natural abundance of species as they existed prior to sampling. In a μCE separation, injections are typically produced electrokinetically at a channel intersection or junction by the manipulation of the potentials that are applied to the fluid reservoirs. Injections can be produced in many different schemes according to the channel geometry and voltage configuration; the most common among these are pinched,[126] double-tee,[4, 127] and gated injections.[115, 128] Pinched and double-tee injections are typically limited by invariable, design-dependent volumes and bi-directional flow in the sample, separation and waste channels whereas gated injections feature variable volumes defined by ∂t and unidirectional flow in each channel. These characteristics make gated injections more suitable for continuous flow sampling[129-131] and 2-D separations.[132-134] However, gated injections suffer greatly from sampling bias, which is an artifact of electrophoretic migration in an electric field. Sampling bias is an undesirable effect because the detected amounts of injected analyte do not represent the true composition of the sample and it makes low-mobility analytes very difficult to detect.[135] The sampling bias produced at a channel intersection during gated injections has two components: a linear flow component and a transradial flow component.[136, 137] The linear component is governed by the fact that analytes with different masses and charges will move at different velocities within the field, such that when the "gate" is opened, faster-moving analytes will be preferentially included in the injection. The transradial component is caused by a discrepancy in the turning radius experienced by analytes with a higher apparent Péclet number compared to those with a lower apparent Péclet number as they turn 90° from the sample channel to the sample waste channel. As a result,

analytes with larger diffusion coefficients (small molecules) extend further into the intersection than large molecules and are therefore preferentially injected. Likewise, when separating mixtures of analytes with very similar diffusion coefficients, those with larger mobilities will be preferentially injected.

Sampling bias in gated injections can be reduced significantly by using large injection times,[136] but increasing the variance associated with the injection decreases the separation efficiency and resolution. Hydrodynamic or pressure-based flow can be used to overcome biasing but its implementation on microfluidic devices is not straightforward due to limited fluid access. Hydrodynamic injections for μCE analysis have been accomplished using hydrostatic pressure from a discrepancy in reservoir height levels,[138-140] diffusion,[137] pressurization of the reservoir using pneumatic[141] and mechanical actuation,[142, 143] syringe pumps[144-147] and pneumatic valving.[144, 148-150] While all have demonstrated some measure of success in reducing sampling bias, these configurations tend to increase the complexity of the channel network architecture, and in some cases produce a limited range of injection volumes[137-139, 142, 147, 150] or significantly increase the time of analysis.[137-140] Importantly, many of the schemes used to produce hydrodynamic injections on microchips are dependent upon the increased coupling of macroscale and microscale components. That is, the microfluidic analysis system is connected to large, off-chip equipment such as syringe pumps, pneumatic feed lines, solenoid valves, gas cylinders, vacuum pumps or electromagnetic actuators.

In Chapter 2, we demonstrated that IDEAs are capable of producing injections when the actuator was fabricated in the proximity of a channel intersection. Producing injections of analyte was a convenient method of investigating how the physical parameters of the system (field strength, IDEA area and DE elasticity) affected performance of the actuator. These IDEA-μCE devices used a typical 4-reservoir cross-channel configuration. The actuator in our device was directly coupled to the fluidic network, such that the channel volume directly opposite a patterned electrode increased when the DE was strained via capacitive Maxwell stress. Instead of varying the potentials applied to the reservoirs to inject plugs of analyte, *i.e.* electrokinetic sampling, injections in this system occurred when the DE transitioned from a strained to an unstrained state. During this transition, the excess fluid was hydrodynamically pushed out of the actuator region and a fraction of this amount was dispensed into the separation channel. In this chapter, we characterize the injections specifically for the purpose of analytical separations as

opposed to an indicator of actuator performance. The concentration profile, efficiency, reproducibility and sampling bias of the IDEA-derived injections are investigated.

3.2. Materials and Methods

3.2.1. Chemicals

Sodium borate, sodium bicarbonate and dimethyl sulfoxide (DMSO) were obtained from Fisher Scientific (Pittsburgh, PA). Sodium dodecyl sulfate (SDS) was obtained from Sigma Chemical Co. (St. Louis, MO). 2',7'-dichlorofluorescein (DCF) was obtained from Acros Organics (Morris Plains, NJ). PDMS (Sylgard 184) was obtained from Dow Corning (Midland, MI). All of these chemicals were used as received. Arginine, proline and glutamic acid were obtained from MP Biomedical (Solon, OH). Fluorescein-5-isothiocyanate (FITC) was purchased from Invitrogen (Molecular Probes, Carlsbad, CA). Derivitization of the amino acids with FITC was performed as recommended by the fluorophore manufacturer according to instructions packaged with the probe. The labeling reaction was accomplished by combining an excess of amino acid solution with amine-reactive FITC. Briefly, each amino acid was dissolved in 150 mM sodium bicarbonate buffer (pH = 9.1) at a concentration of 5 mM. To make the labeling component, 1 mL of DMSO was added to the vial containing 5.3 mg of FITC. The amino acid solution (450 μL; a 3.3x molar excess) was then added to 50 μL of FITC/DMSO solution in a microcentrifuge tube and the reaction was allowed to proceed on a shaker for ~ 4 hours in the dark. This protocol yielded a stock solution of fluorescein thiocarbamyl (FTC)-labeled amino acids at a concentration of 1.36 mM. The distilled, deionized water used to prepare every solution was purified with an E-pure system (Barnstead, Dubuque, IA). Solutions were filtered immediately before introduction to the microchip reservoirs using syringe-driven 0.45 μm PVDF filters (Fisher Scientific).

3.2.2. Microchip Fabrication

The fabrication of IDEA-μCE devices has been described previously in Section 2.2.2. All of the IDEA-μCE devices used in this chapter possess DE layers composed of 20:1 Sylgard 184 PDMS. Regular μCE devices without IDEA units were fabricated using the same procedure described previously except a 2 x 3 inch microscope slide (Corning Inc., Corning, NY) was used as the base.

3.2.3. Separation and Detection

3.2.3.1. Electrophoresis Parameters

The microchip channels were prepped only with the run buffer. In the set of experiments presented here, voltages were applied in two different schemes. The injection process on devices featuring IDEAs has been described previously in Section 2.2.5.1. Gated electrokinetic injections were performed on devices that lacked patterned chrome electrodes. These devices were used as controls with which to compare our results from the devices containing an IDEA. Gated injections have been described in detail elsewhere[151] and consisted of a "load" phase where the potential applied to the buffer reservoir was slightly greater than that applied to the sample reservoir. In the "inject" phase, the potential applied to the buffer reservoir was decreased for a programmed amount of time (the gate) and then returned to its original "load" phase value.

3.3. Results and Discussion

Injections produced by IDEAs possess qualities that are desirable for chemical analysis on microchips. The speed of the injection is primarily dependent on how quickly the excess fluid is expelled into the separation channel; this depends upon injection volume but is typically less than 200 ms. Comparatively, the response times associated with EAP relaxation (~ 2 μs), dielectric actuator capacitor discharging (RC time constant, ~ 10-20 μs) and voltage ramping (power supply slew rate, ~ 2 ms) are less than 3 ms combined. Thus, the overall time required for the injection remains a small fraction of the total analysis time for a run. Like electrokinetically-gated injections, IDEAs are capable of dispensing a range of plug volumes. In Chapter 2, we demonstrated injections that encompass a range of ~ 50 pL to ~ 370 pL[152] but we have achieved both larger and smaller injections (data not shown). Furthermore, EAP actuator technology is very amenable to miniaturization. IDEAs capable of manipulating the aforementioned quantities of fluid have areas less than 2 mm^2. This small footprint can be maintained in the off-chip equipment necessary for device performance as well since small (< 1 inch cubed) HV power supplies are commercially available.

3.3.1. Analysis of the Injection Concentration Profile

When sample is injected into a separation column, the concentration profile of the sample plug can be best described as either a Gaussian profile or an impulse profile.[67] Unlike the Gaussian profile (seen in Figure 1.9), an impulse profile has a rectangular shape (it is also called a "top hat" profile). Electrokinetic-gated injections initially possess an impulse concentration distribution due to the flat fluid front that is formed by electroosmotic flow as it advances down the channel. The variance associated with injections featuring an impulse profile is defined as:

$$\sigma_{inj}^2 = \frac{l_{inj}^2}{12} \qquad (3.1_1)$$

where l_{inj} is the length of the injection. Conversely, hydrodynamic injections possess a Gaussian concentration distribution due to their parabolic flow profile. As such, the variance of an injection band with a Gaussian profile is defined as:

$$\sigma_{inj}^2 = \frac{l_{inj}^2}{16} \qquad (3.1_2)$$

Over the course of a separation, the dispersion associated with the injection is typically negligible compared to the dispersion of sample diffusion. This is especially true for long separations, but injection dispersion can be problematic for rapid separations.

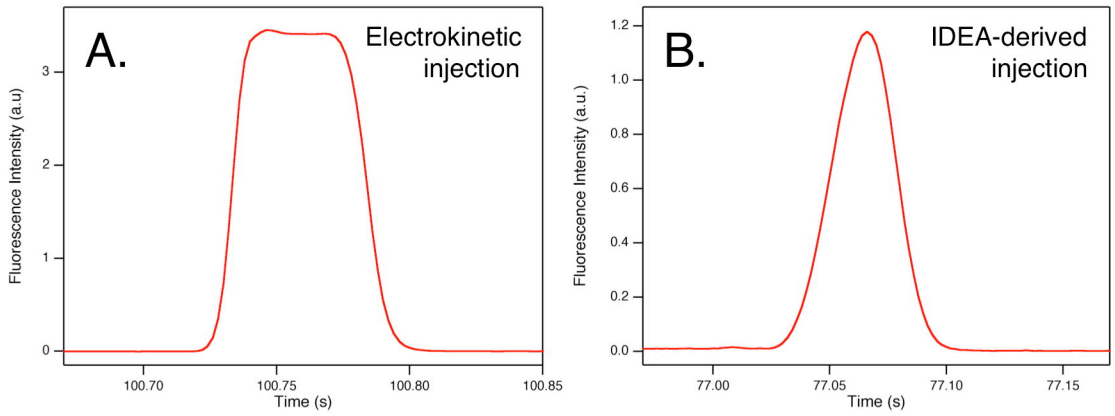

Figure 3.1 Electropherograms showing the profile of (A) an electrokinetic injection and (B) an IDEA-derived injection. Each injection of DCF has approximately the same width (0.082 seconds).

Figure 3.1 shows representative profiles for both an electrokinetic injection and a hydrodynamic injection produced by the discharging of an IDEA. For each type of injection, the

sample was 15 μM DCF in the run buffer, which was 5 mM sodium borate and 1.5 mM SDS (pH = 9.2). Electrokinetic injections and IDEA-derived injections were performed on the same device, which featured a 0.50 mm^2 IDEA with a mean thickness of 40.48 μm. Gated electrokinetic injections were performed by lowering the potential in the BI reservoir from 3160 V to 1960 V for 0.08 seconds. No electrode was attached to the patterned electrode during these runs. IDEA-derived injections were performed by changing V_{cap} from −1240 V to 0 V. Injections were performed in pentuplicate. Plugs of analyte were separated at a field strength of ~ 500 V/cm and detected just 100 μm downstream of the channel intersection. The short separation distance helps preserve the integrity of the concentration profile for the injection plug.

In order to numerically evaluate the concentration profile of the injection plugs, we considered the area of a perfect Gaussian peak (A_{gauss}) as:[153]

$$A_{gauss} = \sqrt{2\pi}\left(h\sigma\right) \tag{3.2}$$

where h is the height of the peak. This area is compared to the area of a rectangle with the same height and width as the Gaussian peak. In this case, however, the width of the Gaussian peak is not the same as w_b (described in Section 1.3.3.3.). This is because w_b intersects the Gaussian curve at ~ 13% of its height. Instead, the width used in this analysis is 8σ, which is exactly twice the length of w_b. Thus, the area of the rectangle used in this analysis is defined as:

$$A_{rect} = 8\sigma h \tag{3.3}$$

The percentage area that a perfect Gaussian curve will occupy in this rectangle can be calculated by the following equation:

$$\%A = \frac{\sqrt{2\pi}\left(h\sigma\right)}{8h\sigma} \times 100 = \frac{\sqrt{2\pi}}{8} \times 100 \tag{3.4}$$

which is ~31.3%.

The injections featured in Figure 3.1 were selected for analysis because they each have widths of approximately 0.082 seconds. Just by visual inspection, it is obvious that the electrokinetic injection has a more rectangular or “impulse” profile while the IDEA-derived injection is more reminiscent of a Gaussian profile. The area of each injection was determined by using the “print area” command in IGOR Pro. These calculated areas were then compared to the area of a corresponding rectangle with a width of ~ 0.082 seconds and a height as determined

from the electropherogram (units of volts) using Equation 3.4. It was determined that the area ratio of the electrokinetic injection is 62.32 ± 0.16 % while the area ratio of the IDEA-derived injection is only 40.31 ± 0.28 %. Thus, the area ratio of the IDEA-derived injection is much closer to the 31.3 % area ratio of a perfect Gaussian than the area ratio of the electrokinetic injection, which is almost twice this value.

3.3.2. Effect of Possible EOF Modification Due to IDEA Operation

As mentioned in Chapter 2, electric fields applied externally to the channel manifold have been demonstrated to elicit a change in the electroosmotic flow.[123, 154, 155] We have eliminated this type of EOF control as a major contributor in the production of injections due to the action of an IDEA. However, small changes in the global EOF can cause run-to-run irreproducibility and therefore is detrimental to the long-term operation of the device. In order to investigate whether or not the stability of the EOF is affected by the operation of an IDEA unit, we performed a series of electrokinetic injections on a device with a 0.25 mm^2 IDEA unit that featured a DE layer with a mean thickness of 38.10 μm. Injections of 2.72 μM FTC-labeled arginine were performed by lowering the potential in the BI reservoir from 3160 V to 1960 V for 0.02 seconds. The run buffer consisted of 5 mM sodium borate and 1.5 mM SDS (pH = 9.2). In one run, a series of triplicate injections were separated at ~ 500 V/cm while V_{cap} was held constant at −1962 V, −1442 V and −962 V. In between each of these series, triplicate injections were separated while V_{cap} was held constant at 38 V. In a second run, the same format was used except that V_{cap} was held constant at 1038 V, 1518 V, and 2038 V while the analyte bands were eluted. Injections were detected after a separation distance of 2 cm.

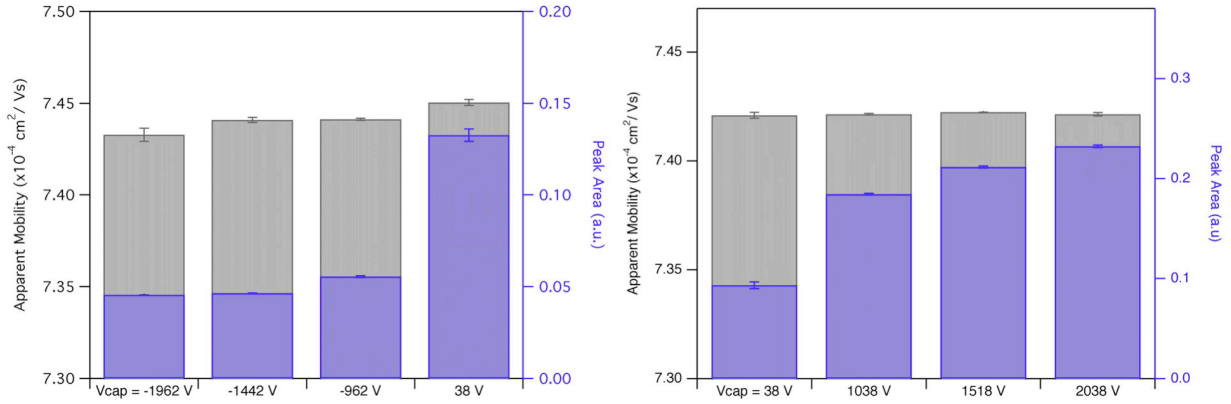

Figure 3.2 Graph showing the change in apparent mobility and peak area for electrokinetic injections of FTC-labeled arginine due to the presence of an external electric field. Changes in mobility are practically insignificant and changes in peak area are caused by the unintentional operation of the IDEA during the time gate.

Figure 3.2 shows the mean apparent mobility (μ_{app}) and peak area for each magnitude of V_{cap} investigated in the two runs. The data shows that μ_{app} does not change significantly as the magnitude of V_{cap} is changed during the experiment. In fact, the largest discrepancy (from 7.45 x 10^{-4} to 7.42 x 10^{-4} cm^2 / Vs represents only a 0.40% change in both mobility and migration time. Thus, there is no evidence that any changes in mobility during the course of an experiment can be attributed to the capacitance associated with IDEA operation instead of more common factors like temperature fluctuations and sorption. One interesting effect with this experiment, however, is the fluctuation in peak size as a function of V_{cap}. It was determined that this effect was caused by unintended IDEA operation during the time gate, since V_{pe} was held constant even while $V_{channel}$ was modified. The injections corresponding to V_{cap} = −1962 V, −1442 V and −962 V in Figure 3.2 are smaller than those for V_{cap} = 38 V because the capacitor was being charged (fluid intake) during the transition from the gate voltage to the separation field strength. The opposite is true for the injections corresponding to V_{cap} = 1038 V, 1518 V and 2038 V; capacitor discharging (fluid expulsion) causes the increase in peak size. Thus, these injections are not purely electrokinetic but instead they represent a blend of electrokinetic and hydrodynamic mechanisms.

3.3.3. Comparison of Separation Efficiency Between Electrokinetic and Hydrodynamic Injections

When determining the efficacy of a novel injection method for μCE analysis, it is necessary to evaluate separation performance and compare it to the benchmark of electrokinetic injections. Figure 3.3 shows a plot of peak efficiency as a function of migration time for six sets of pentuplicate injections. For each type of injection, the sample consisted of 2.72 μM FTC-labeled arginine, proline and glutamic acid in the run buffer, which was 10 mM sodium borate and 5 mM SDS (pH = 9.5). Plugs of analyte were separated at a field strength of ~ 500 V/cm and detected at six different locations along the separation channel. These locations corresponded to separation distances of 0.5 cm, 1.008 cm, 1.516 cm, 2.024 cm, 2.532 cm and 2.786 cm.

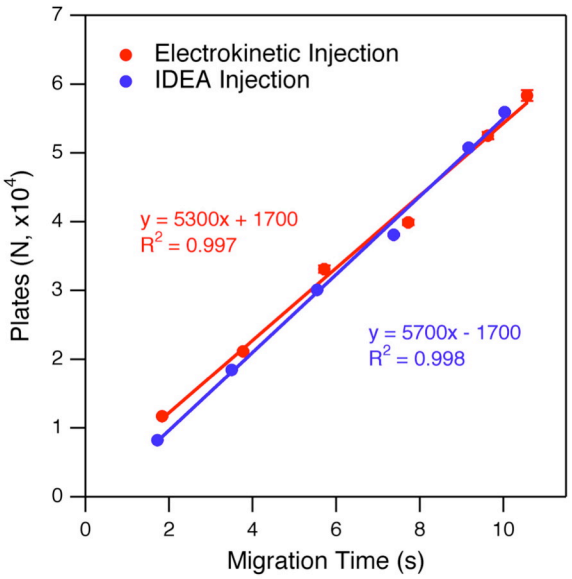

Figure 3.3 Plot showing the rate of plate generation for FTC-Arg from samples that were injected electrokinetically (red) and hydrodynamically (blue) using an IDEA unit.

Electrokinetic injections were made by lowering the potential in the BI reservoir from 3160 V to 1960 V for 0.02 seconds. IDEA-derived injections were made by changing V_{cap} from 1000 V to 0 V on a device with a 0.5 mm^2 IDEA and a mean DE thickness of 40.00 μm. The data in Figure 3.3 shows that the rate of FTC-Arg plate generation for IDEA-derived injections was analogous to electrokinetic injections under similar separation conditions. Discrepancies in migration time are probably due to environmental effects and perhaps a difference in EOF resulting from a

variance in PDMS composition between devices. Furthermore, the linearity of the data suggests that separations with both types of injection are diffusion-limited. In physical terms, this suggests that the mechanical action of the IDEA unit does not significantly impact separation performance. Data comparing the rates of plate generation for FTC-Pro and FTC-Glu as well as resolution data using each injection method can be seen in Table 3.1 and Table 3.2.

Table 3.1 Plate generation data for FTC-Pro and FTC-Glu using both electrokinetic (EK) and IDEA-derived injections.

FTC-Pro	EK	$y = 3800x + 1800$	$R^2 = 0.997$
	IDEA	$y = 4000x - 240$	$R^2 = 0.999$
FTC-Glu	EK	$y = 3000x + 1400$	$R^2 = 0.995$
	IDEA	$y = 3400x - 950$	$R^2 = 0.998$

Table 3.2 Resolution data for FTC-labeled amino acids at two separation distances using both electrokinetic (EK) and IDEA-derived injections.

$Peak_1$-$Peak_2$		EK 0.500 cm	IDEA 0.500 cm	EK 2.786 cm	IDEA 2.786 cm
Arg – Pro		4.8	4.0	11.3	10.9
Arg – Glu		8.2	6.9	19.5	19.1
Pro – Glu		3.6	3.0	8.4	8.2

3.3.4. Injection Reproducibility

Ideally, an injection technique will dispense the same amount of sample for each run under identical injection parameters and it will also maintain this same volume over a long period of time. This is especially important for continuous-sampling experiments since the correct interpretation of data often depends on reproducible injection volumes. In order to demonstrate the reproducibility of the IDEA-derived injections, 64 consecutive injections were performed on an IDEA device. The electropherograms in Figure 3.4a shows injections of 15 μM DCF in the run buffer, which was 10 mM sodium borate (pH = 9.2). The IDEA device used for this experiment had a 0.25 mm^2 IDEA and a mean DE thickness of 40.48 μm. Injections were

made by changing V_{cap} from -1320 V to 0 V and plugs of analyte were detected 0.5 cm downstream of the injection cross. The injection sequence consisted of 8-second run times with 1 second between the charging and discharging of the IDEA unit; the total run time was 580 seconds.

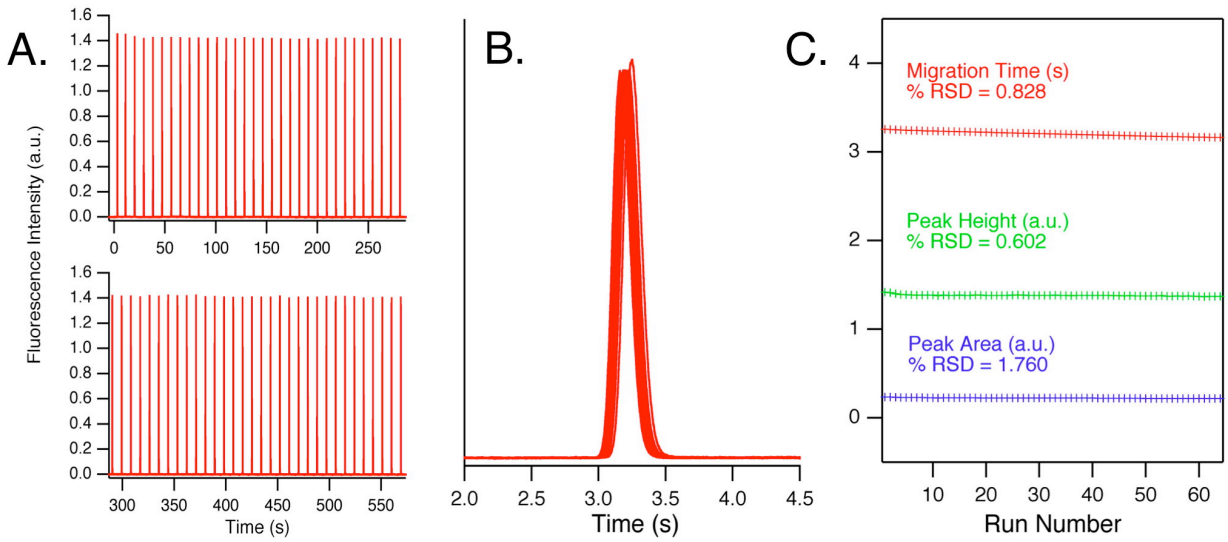

Figure 3.4 Reproducibility of 64 consecutive injections of DCF separated at ~ 500 V/cm on an IDEA-µCE device. (A) Electropherograms showing all 64 injections over a span of 9.67 minutes. (B) Overlay of DCF peaks from runs 1, 10, 19, 28, 37, 46, 55 and 64. (C) Migration time, peak height and peak area values for each of the injections with mean values of 3.204 seconds, 1.380 a.u. and 0.222 a.u. for each, respectively.

The electropherogram in Figure 3.4b shows an overlay of DCF peaks from runs 1, 10, 19, 28, 37, 46, 55 and 64. Despite the drift in migration time, it is evident that the peaks have a uniform size and Gaussian shape. The graph in Figure 3.4c plots migration time, peak height and peak area – three different indicators of injection and separation reproducibility – for each of the 64 injections shown in Figure 3.4a. The average migration time for these injections was 3.204 ± 0.027 seconds. The variation in migration time that is present between run 1 (3.255 seconds) and run 64 (3.163 seconds) is probably due to an increase in the local temperature during the course of the experiment. The average values for the peak height and peak area are 1.380 ± 0.008 and 0.222 ± 0.004. Each of the indicators of reproducibility have RSDs less than 2%, which is better than or equal to numerous other pressure-based injection strategies.[139, 142-144, 146]

The data in Figure 3.4 implies that there is minimal hysteretic behavior present with the operation of the DE actuation unit. Indeed, it has been reported that EAP actuation at low strains is very reproducible over thousands of voltage cycles.[85] The majority of the actuator reproducibility has two origins. The first is that there are no intricate or fragile moving parts, only the elastomeric EAP layer, which is mechanically robust. The second is that the volume of the injection is dependent mainly upon the magnitude of V_{cap}, and the time component to the injection is limited to allowing adequate time between capacitor charging and discharging, *i.e.* for the fluid to completely fill the excess channel volume above the IDEA unit before it is expelled into the separation channel.

3.3.5. Analysis of Sampling Bias for IDEA-derived Injections

Figure 3.5 is an electropherogram of a mixture of FTC-labeled amino acids using both a gated electrokinetic injection and an IDEA-derived injection. The sample consisted of 2.72 μM FTC-labeled arginine, proline and glutamic acid in the run buffer, which was 10 mM sodium borate and 5 mM SDS (pH = 9.5). For the purpose of comparison, the height of each arginine peak was normalized. In each injection method, the analytes were separated at a field strength of ~ 500 V/cm and detected 2.00 cm downstream of the intersection. The electrokinetic injection had a 0.02 second inject phase in which the potential in the BI reservoir was decreased from 3160 V to 1960 V. The IDEA-derived injection was performed by changing V_{cap} from -1000 V to 0 V on a device with a 0.5 mm^2 IDEA and a mean DE thickness of 40.00 μm. From the electropherogram, it is evident that the IDEA-derived injections contain a different relative chemical composition than electrokinetic injections. The noticeably larger spread of peak heights present in the electrokinetic injection suggests a large amount of sample bias. This is expected since FTC-Arg, FTC-Pro and FTC-Glu have two, three and four nominal negative charges, respectively, at pH 9.5; thus, FTC-Arg is repelled least and FTC-Glu is repelled most from the BW reservoir. Discrepancies in migration times are probably due to small differences in the EOF.

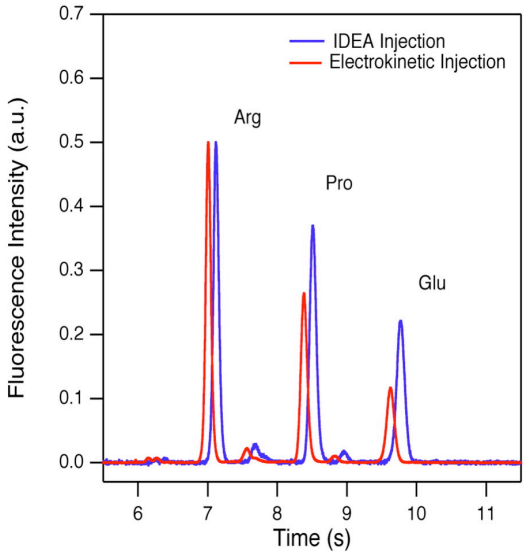

Figure 3.5 Electropherograms showing the difference in chemical composition between electrokinetic injections (red trace) and IDEA-derived injections (blue trace) for a mixture of FTC-labeled arginine, proline and glutamic acid. For visualization purposes, the heights of the arginine peaks have been normalized.

Using the same amino acid mixture, we investigated the relationship between peak area percentage and injection volume for both electrokinetic and IDEA-derived sample introduction. The peak area percentage is the ratio of one peak area to the total area of all the peaks in the separation, multiplied by 100. Figure 3.6 shows the peak area percentages obtained for each amino acid employing these two different injection methods. For all injections, the analytes were separated at a field strength of ~ 500 V/cm and detected 2.0 cm downstream of the injection cross. The electrokinetic and IDEA-derived injections were performed on the same device. During electrokinetic injections, V_{pe} was held constant at $V_{channel}$ while the potential in the BI reservoir was decreased from 3160 V to 1960 V. The time gates for the 6 sets of electrokinetic injections were 0.02, 0.04, 0.06, 0.08, 0.10 and 0.12 seconds. The 6 sets of IDEA-derived injections were performed by changing V_{cap} from −1000, −1200, −1400, −1600, −1800 and −2000 V to 0 V across an DE layer with a mean thickness of 40.00 μm and an a 0.50 mm^2 IDEA.

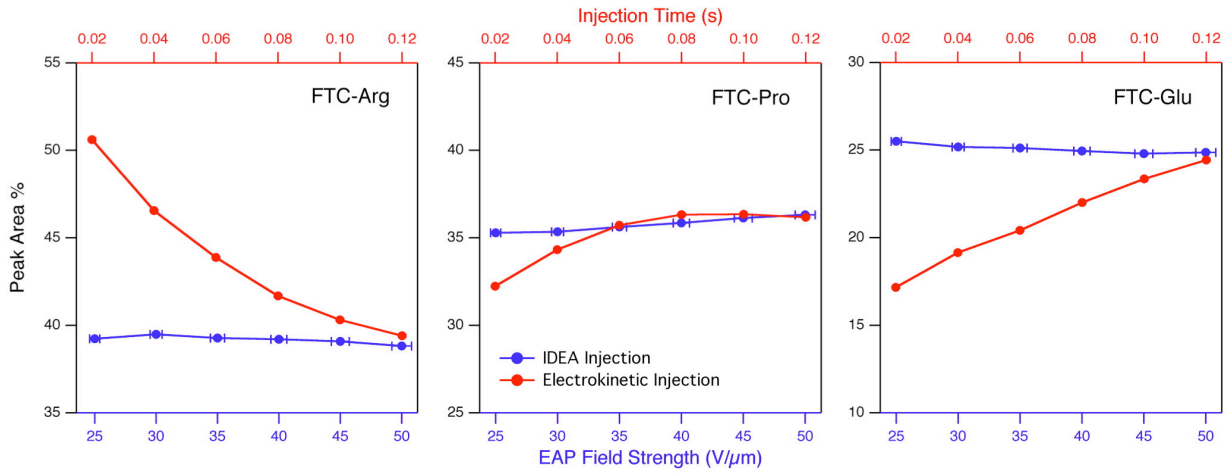

Figure 3.6 Plots showing the relationship between injection volume and peak area percentage with a mixture of three FTC-labeled amino acids for electrokinetic injections (red) and IDEA-derived injections (blue). Five separations were performed with each injection volume.

It is evident from the data that the chemical composition of the IDEA-derived injections was very stable as a function of injection volume. The range of total peak area between the smallest injection (ΔV_{cap} = 1000 V) and the largest (ΔV_{cap} = 2000 V) was 0.046 – 0.513 (arbitrary units). Over this range, the mean arginine, proline and glutamic acid peak area percentages for all 30 injections were 39.18 ± 0.21%, 35.75 ± 0.39% and 25.06 ± 0.24%, respectively. Conversely, the behavior of the peak area percentages for electrokinetic sampling as the injection volume increased was consistent with theoretical studies.[136] That is, the peak area percentages for a mixture of analytes will asymptotically approach the true peak area percentages of the sample as the injection volume increases. It is obvious from the data that the smallest electrokinetic injections (0.02 s, 0.133 total peak area) were very biased, with the largest discrepancies for the amino acids with the highest and lowest apparent mobilities. Smaller electrokinetic injections, comparable with the smallest IDEA-derived injections, would experience even more extreme sampling bias. Only the largest electrokinetic injections (0.12 s, 1.364 total peak area) seem to possess the true peak area percentage for all three amino acids. However, fast separations with large injections can exhibit non-Gaussian peaks and erode resolution, making them more problematic for electrophoretic separations.

3.4. Conclusions

The performance of integrated dielectric elastomer actuators (IDEAs) used specifically to hydrodynamically inject samples for microchip electrophoresis has been evaluated. The integration of these actuators onto the existing microfluidic platform is a simple process that does not require modification of the standard μCE channel geometry. Importantly, IDEAs can be operated without the use of additional large, off-chip equipment since they only require the use of a single high-voltage power supply. Injections made using IDEAs are fast (< 200 ms) and do not display a significant amount of hysteresis. Changing the magnitude of the electric field across the EAP layer prior to capacitor discharging can vary the injection volume. Regarding separation performance, it was determined that IDEA-derived injections do not erode the separation efficiency of the analytes while maintaining an excellent level of reproducibility. These are qualities that enable IDEA devices to handle fluid sampling from a wide range of sources under many different experimental conditions. Lastly, the IDEA-derived injections display a negligible amount of sampling bias, which preserves important information about the relative abundance of species in a mixture.

Chapter 4 - Investigation of IDEA Compression

4.1. Introduction

In Chapter 2, we investigated how changing the physical parameters (V_{cap}/IDEA size/DE elasticity) of the system affects the degree of actuation. From EAP theory and the results of our experiments, there are three obvious methods for increasing the total fluid displacement in an IDEA: increasing the (1) Maxwell stress for a given DE thickness, (2) the DE elasticity (strain) and (3) the area of the IDEA. This can be accomplished experimentally by increasing V_{cap}, changing the electronic (dielectric constant) and physical (elasticity) properties of the DE layer, or changing the dimensions of the patterned electrode or the microchannel. However, increasing V_{cap} is only effective up to the dielectric strength of the DE layer, at which point catastrophic failure occurs. The use of high voltages also poses a safety risk to the operator. Changing the electronic and physical properties of the DE layer is not easily done without changing the chemistry of the DE, which may prohibitively complicate microchip fabrication and/or operation. Furthermore, increasing the dielectric constant of the DE through the use of high-*k* dopants may decrease its elasticity, which is counter-productive.

The goal of efforts to maximize the performance of an IDEA unit should be to produce a high level of DE strain while minimizing V_{cap}. This will increase the user-friendliness of the device as well as decrease the complexity of the electronics needed to operate it. Perhaps the most promising method of meeting this goal is through careful design of the channel and patterned electrode geometries. The largest problem with increasing the size of the IDEA units as described in Section 2.3.3. is that simply increasing the length of the patterned electrode produces an actuator with a large fluidic resistance per unit area as well as a grossly large effective width. It is necessary that the incorporation of IDEA units onto a microfluidic device does not significantly change the scale of the fluidic network. Furthermore, decreasing the effective length and width of a single IDEA unit will allow for multiple units to be place in close proximity (~ 1500 μm apart) of one another. Thus, in order to maximize the fluid displacement in the channel while reducing the effective size of the IDEA, it is important to understand exactly how actuation of the DE layer deforms the microchannel region opposite the patterned electrode.

In order to predict the mechanical behavior of DE actuators, Soulimane *et al*. modeled the deformation of a PDMS film sandwiched between two metallic electrodes.[156] The PDMS DE layer used in the model was a rectangular film (200 μm × 400 μm) with a thickness of 10 μm. The compression of the DE layer was simulated using CoventorWare software when a Maxwell stress of 200 Pa was generated between the electrodes. According to their model, the PDMS film is deformed to a higher degree at the corners and along the edges as compared to the center of the film. This "compression map" provides more detailed information about DE actuation that is communicated through illustrations that show the general mechanism of DE actuation (such as Figure 1.11). However, Soulimane *et al*. did not provide any experimental data to corroborate the results of their model.

In this chapter, we create a model of our IDEA configuration to probe the magnitude of the electric field in relationship to the microchannel cross-section. The results of this model are compared to the deformation model created by Soulimane *et al*. Furthermore, we use fluorescence microscopy to analyze how IDEA operation deforms the microchannel geometry. The nature of this deformation is analyzed at different values of V_{cap} for a 0.05 mm^2 IDEA. Lastly, we investigate the local deformation of the active microchannel area for a 0.50 mm^2 IDEA at different distances from the channel intersection on an IDEA-μCE device. Analysis of the difference in fluorescence intensity between the actuated and unactuated states of the IDEA is used to estimate the increase in channel volume that occurs during actuator operation.

4.2. Materials and Methods

4.2.1. Modeling Parameters

Modeling of the electric field between the patterned electrode and the microfluidic channel during IDEA actuation was performed by Dr. Ryszard Jankowiak (Department of Chemistry, Kansas State University) using COMSOL Multiphysics software on a 64-bit machine (0.6 Tflops, 8 GB RAM, 3.2 GHz Quad Core processor). The PDMS fluidic layer is 0.8 mm thick. The microchannel has a width of 50 μm and a depth of 20 μm. The channel is separated from the patterned chrome electrode by a layer of PDMS that is 40 μm thick. The patterned electrode is 1 μm thick, 2 mm wide and sits directly on a piece of 1 mm thick glass. The center of the patterned electrode sits directly beneath the center of the channel. For these calculations, the dielectric constant of the PDMS was 2.65. The channel was filled with an aqueous solution

having a dielectric constant of 80 and a conductivity of 1 siemen/meter. In the simulation, the potential in the microchannel was increased step-wise from 0 V to 1000 V, 1333 V, 1666 V and finally 2000 V. The potential applied to the patterned chrome electrode has held at ground during the simulation.

4.2.2. Chemicals

Sodium borate, sodium bicarbonate and dimethyl sulfoxide (DMSO) were obtained from Fisher Scientific (Pittsburgh, PA). Sodium dodecyl sulfate (SDS) was obtained from Sigma Chemical Co. (St. Louis, MO). PDMS (Sylgard 184) was obtained from Dow Corning (Midland, MI). All of these chemicals were used as received. Arginine was obtained from MP Biomedical (Solon, OH). Fluorescein-5-isothiocyanate (FITC) was purchased from Invitrogen (Molecular Probes, Carlsbad, CA). Derivitization of the amino acids with FITC was performed as recommended by the fluorophore manufacturer according to instructions packaged with the probe. The labeling reaction was accomplished by combining an excess of amino acid solution with amine-reactive FITC to produce FTC-labeled amino acids at a concentration of 1.36 mM. This procedure has been detailed thoroughly in Section 3.2.1. The distilled, deionized water used to prepare every solution was purified with an E-pure system (Barnstead, Dubuque, IA). Solutions were filtered immediately before introduction to the microchip reservoirs using syringe-driven 0.45 μm PVDF filters (Fisher Scientific).

4.2.3. Microchip Fabrication

The fabrication of IDEA-μCE devices has been described previously in Section 2.2.2. The devices used in this chapter are identical to those used in Chapter 2 and Chapter 3 except that the patterned electrode is made of indium tin oxide (ITO) instead of chrome. ITO was used because it is optically transparent in thin films and therefore allows us to spectroscopically interrogate the IDEA unit during its operation. Production of ITO electrode bases is described below.

4.2.3.1. Fabrication of ITO Electrodes

2 x 3 inch ITO-coated glass slides (Delta Technologies, Stillwater, MN) were used to fabricate the electrode bases. These slides are polished float glass (0.7 mm thick) coated with 120 – 160 nm of ITO. The ITO film has a resistance between 8 and 12 Ω and an optical

transmittance greater than 83%. The ITO slides were cleaned for 15 minutes in a sonication bath of 20% (w/w) ethanolamine in distilled and deionized water at 80 °C. After sonication, the slides were rinsed with copious amounts of water and then dried in an oven at 175 °C for no less than 30 minutes.

After drying, the ITO slides were coated with S1811 positive photoresist (Rohm & Haas, Marlborough, MA) using a spin-coater. The resist was spun at 2000 rpm for 30 seconds. The ITO slide was then baked at 115 °C for 1 minute prior to UV exposure through a photomask transparency with the electrode pattern printed on it (same masks as those described in Section 2.2.2.1). After an exposure dose of ~ 110 mJ/cm^2 from a near-UV flood exposure system, the weakened photoresist was removed in 351 series developer (Rohm & Haas). The slide was then rinsed with water and dried in a stream of nitrogen.

Etching of the exposed ITO was performed in a solution that consisted of 20% (v/v) HCl, 5% HNO_3 and a small amount of detergent. This solution was heated to at least 55 °C in order to expedite the etching process. The resist-covered ITO slides were submerged in the etching solution for 2 minutes, after which time they were immediately rinsed with a 10% (w/w) solution of Na_2CO_3 in order to stop the etching reaction. The ITO slide was rinsed off with copious amounts of water and then rinsed with acetone and ethanol to remove the remaining photoresist.

4.2.4. Compression Analysis

In order to analyze deformation of the IDEA, a 16-bit cooled CCD camera (Roper Scientific, Trenton, NJ) was used in conjunction with a Nikon Eclipse TE2000-U inverted microscrope (Nikon Instruments Inc, Melville, NY). An epiluminescence attachment featuring a mercury arc lamp and a Nikon B-2A filter block were used to produce the excitation light, which was between 450 and 490 nm in wavelength. The light was focused on the channel region directly above the patterned ITO electrode with a 20 × Nikon objective. Voltages were applied to the channel reservoirs with platinum electrodes connected to a custom-made Bertan HV power supply (Hauppauge, NY). This power supply consisted of five separate HV units (0 – 10 kV) that were individually controlled through a Labview program that was written in-house (National Instruments, Austin, TX).

The microfluidic channels were prepped only with run buffer, which was 5 mM sodium borate and 1.5 mM SDS (pH = 9.2). Both the BI and SI reservoirs were filled with 5.44 μM

FTC-arginine, which simply acted as a fluorophore to highlight the channel network. Potentials were applied to the BI and SI reservoirs and the FTC-Arg solution was allowed to flow through the channels for at least 5 minutes in order to obtain a stable fluorophore concentration. In order to probe channel deformation due to IDEA operation, the CCD camera recorded images while the IDEA was switched back and forth between its actuated and relaxed states. A series of 17 images (9 actuated and 8 unactuated, each with a 30 ms exposure time) were recorded 4 seconds apart, such that an image was recorded approximately midway between capacitor charging and discharging. The relationship between the voltages sequence and the image capture time can be seen in Figure 4.1. Each run investigated actuator operation as it switched back and forth between V_{cap} values of approximately zero and a significant, non-zero value. All of the images from the cooled CCD camera were recorded using WinView32 software (Roper Scientific).

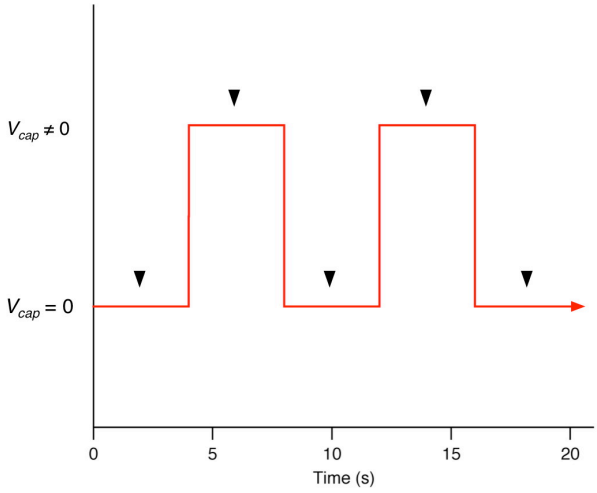

Figure 4.1 Schematic showing the voltage sequence applied during a compression analysis experiment. V_{cap} is switched back and forth between zero and a non-zero value at 4 second intervals. Images were also recorded at 4 second intervals but with a 2 second phase shift relative to the voltage transitions (black triangles).

4.3. Results and Discussion

4.3.1. Modeling Analysis

Panels A – D of Figure 4.2 show the results of the modeling study when potential drops of 1000 V, 1333 V, 1666 V and 2000 V, respectively, are applied across the DE layer. In these images the microchannel cross-section is visable as the large rectangle in the middle of the panel

and the patterned electrode is the thin strip located near the bottom of the panel. The small rectangle inside the channel is a copper electrode, which was used in the model to simplify the application of potentials in the system. The vector arrows show the magnitude and direction of the electric field lines present between the channel and the patterned electrode. The color scale shows the potential present in the system at that location.

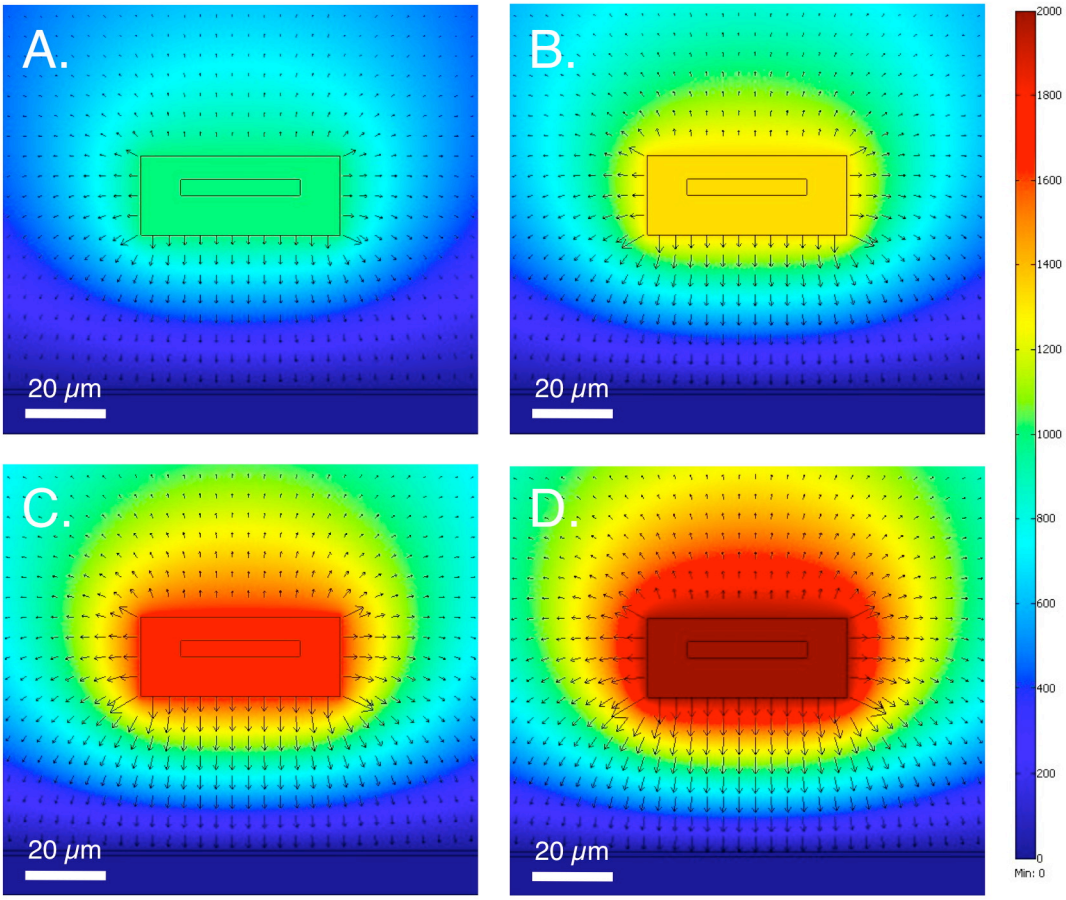

Figure 4.2 Illustrations that show the electric field lines present on an IDEA device when V_{cap} is (A) 1000 V, (B) 1333 V, (C) 1666 V and (D) 2000 V. These images were produced using COMSOL Multiphysics software.

Of particular note in these images is the size of the electric field vector arrows across the bottom of the channel. Larger arrows correspond to a greater electric field at that location. At each value of V_{cap}, the vector arrows are smallest in the center of the channel and increase as they approach the side of the channel. The vector arrows located at the corners of the channel cross-section (channel edges) are drastically greater than along the rest of the channel floor. The results obtained from this model agree with those results obtained by Soulimane *et al*. since a

greater electric field strength along the edges of the active IDEA area would produce greater compression in those areas. Likewise, the smaller electric field strength in the middle of the active IDEA area would produce a lower degree of compression.

4.3.2. Image Analysis

Images were analyzed using ImageJ software (National Institutes of Health). Specifically, line scans measuring the fluorescence intensity were performed across the width of the channel at chosen locations. The line scans had a width of 4 pixels and an arbitrary length. The pixel coordinates chosen from the first image in the first series analyzed were then applied in the analysis of all the other images taken at that location. Natural fluctuations in the intensity of the mercury arc lamp produce occasional images with significantly increased or significantly reduced intensities. These images were identified and discarded. The remaining line scans for a given run were averaged together to produce two line scans – one representing the mean actuated state and the other representing the mean unactuated state. The line scan for the mean unactuated state was then subtracted from the line scan for the mean actuated state, which produced a line scan of the intensity difference between these two states. This process can be seen in Figure 4.3. Alternatively, the "image math" function (Process > Math > Add/Subtract/Multiply/Divide/etc.) in ImageJ could be used to obtain a full image of the difference between these two states from the original images.

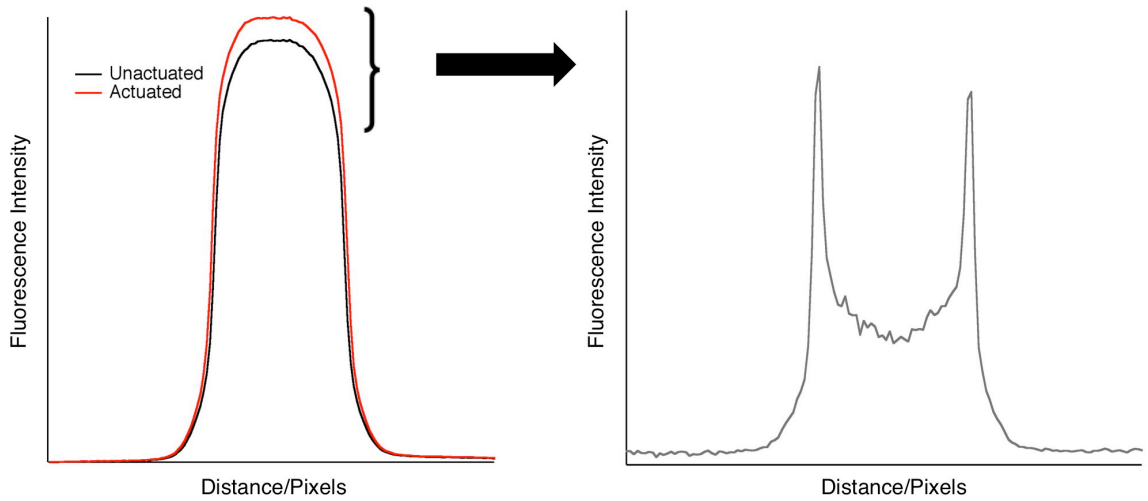

Figure 4.3 Illustration showing representative mean line scans from the actuated and unactuated states of an IDEA during operation. The second panel shows the difference in fluorescence intensity between the two states.

The difference in the fluorescence intensity between the actuated line scan and the unactuated line scan represents the additional volume of fluorophore in the channel, which is caused by the deformation of the DE layer during IDEA actuation. As detailed in Section 1.4.2., this deformation consists of compression in the *z* axis (thickness) and stretching in the *x* and *y* axes. These strains are manifested as an increase in both the width and depth of the microfluidic channel. Visual investigations of the differential line scans show both aspects of the channel deformation. Figure 4.4 shows a portion of a representative differential line scan; the portion shown here starts outside of the channel and then terminates in the middle of the channel. The dashed line shows the position of the channel wall in the unactuated state. The location of the unactuated channel walls were assigned by the *x* coordinates at the FWHM (full width at half-maximum) for the unactuated line scans. The FWHM corresponded very closely to the width of the microfluidic channels measured in bright field, which is ~ 52 µm.

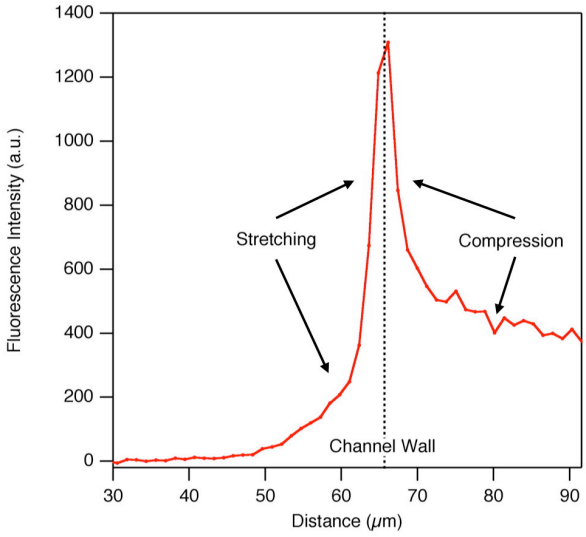

Figure 4.4 A differential line scan showing how the change in fluorescence spatially relates to the position of the unactuated channel wall.

In the middle of the channel (around the 90 µm mark in Figure 4.4), the increase in fluorescence is evidence of an increase in the channel depth due to compression of the DE layer. Towards the channel wall, the increase in fluorescence rises sharply. Arguments can be made that this increase is due to two different phenomena: an increase in DE compression along the edge of the IDEA (compared to the middle of the channel) and an increase in the channel width.

We suspect that the "bat ear" appearance of the differential trace is due to both of these phenomena working in tandem. Specifically, a larger amount of compression is mainly responsible for the large increase in fluorescence just inside of the unactuated channel wall position and channel width expansion is mainly responsible for the large increase in fluorescence just outside of the unactuated channel wall position. Thus, it would appear that these results confirm the results obtained from theoretical analysis performed by Soulimane *et al*.

4.3.3. Analysis of Channel Deformation as a Function of V_{cap}

Figure 4.5 shows the differential line scans for an IDEA during operation at V_{cap} values of approximately ± 1000 V, ± 1320 V, ± 1640 V and ± 2000 V. The device used in this experiment had a 0.05 mm^2 IDEA with a mean DE thickness of 40.48 µm. Line scans were performed across the channel and run through the approximate middle of the IDEA. It is obvious from the graphs that the difference in fluorescence between the actuated and unactuated states increases as a function of $|V_{cap}|$. One interesting thing to note is that the lateral position of the fluorescence apices in the differential scans do not appear to change significantly as $|V_{cap}|$ increases. This further suggests that the large increase in fluorescence at the edge of the channel is due an increase in compression in this region and not solely due to the widening of the channel from DE expansion in this plane. Otherwise, it would be expected that the distance between the apices would increase as $|V_{cap}|$ increases.

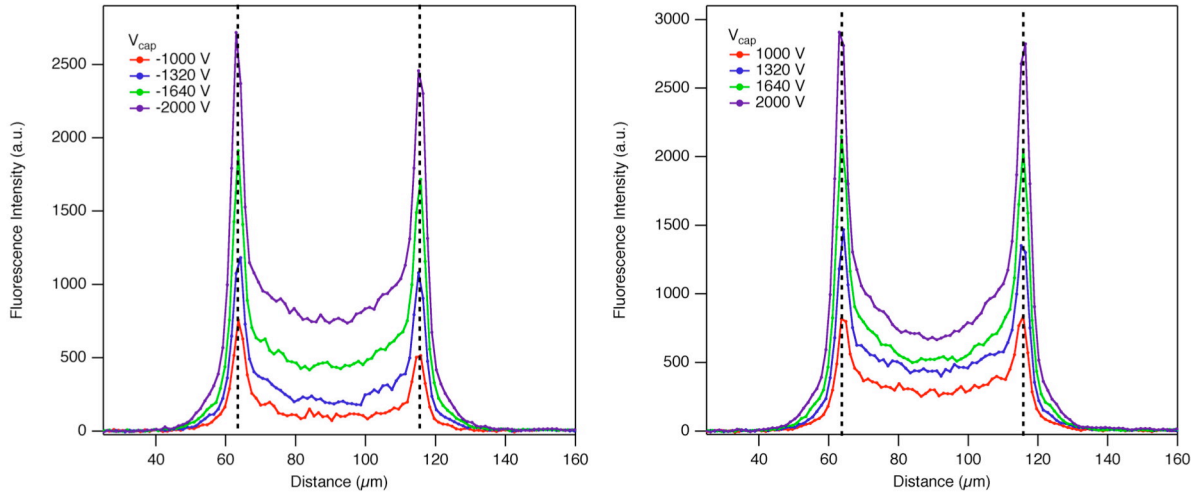

Figure 4.5 Graphs showing the differential line scans for $|V_{cap}|$ values of ± 1000 V, ± 1320 V, ± 1640 V and ± 2000 V with negative polarity (left) and positive polarity (right). The

location of the channel walls in the unactuated state are shown on the graphs as dashed lines.

An approximate volume change in the active channel region during IDEA actuation can be obtained from the relationship between the integrals for the differential line scan and the mean unactuated line scan. The working assumption here is that the relationship between these two integrals is proportional to the relationship between the change in channel volume and the native channel volume. In order to extrapolate from a cross-sectional area to a volume, we also assume that the voltage drop in the channel across the IDEA (~ 50 V) is insignificant; that is, we assume that the differential line scan is the same at every point along the length of the active channel. This relationship is described by the following equation:

$$\frac{A_{dls}}{A_{muls}} = \frac{\Delta V}{V_0} \tag{4.1}$$

where A_{dls} is the area of the differential line scan, A_{muls} is the area of the mean unactuated line scan, ΔV is the change in the volume of the channel and V_0 is the native volume of the channel. The native volume of the active channel region is 1.02 nL. The area values from the line scans were obtained from analysis in IGOR Pro and are given in Table 4.1.

Table 4.1 Integrated fluorescence data from the line scans in Figure 4.5. The data was obtained from directly from IGOR analysis using the "print area" command.

V_{cap}		A_{dls}	A_{muls}	A_{dls} / A_{muls}
−1000 V		10254.9	583423	0.017577
−1320 V		19400.5	587509	0.033022
−1640 V		34289.0	589742	0.058142
−2000 V		54758.6	588564	0.093038
1000 V		19343.6	583188	0.033169
1320 V		30822.6	584787	0.052707
1640 V		40834.3	588103	0.069434
2000 V		57113.3	589608	0.096867

Inserting these values along with the native channel volume into Equation 4.1 gives a value of additional channel volume for each value of E_{cap}. The relationship between these two sets of values can be seen in Figure 4.6. The general trend seen here is the same as that witnessed for the size of electrophoretic injections produced by IDEA actuation. The largest actuator response, obtained at E_{cap} = 49.4 V/μm, corresponds to a 9.7% increase in the volume of the active channel segment. It is evident from this data that there is a difference in the magnitude of the actuator response between the negative and positive polarities of E_{cap}. This same effect was seen in Figure 2.8 and its cause is currently unknown.

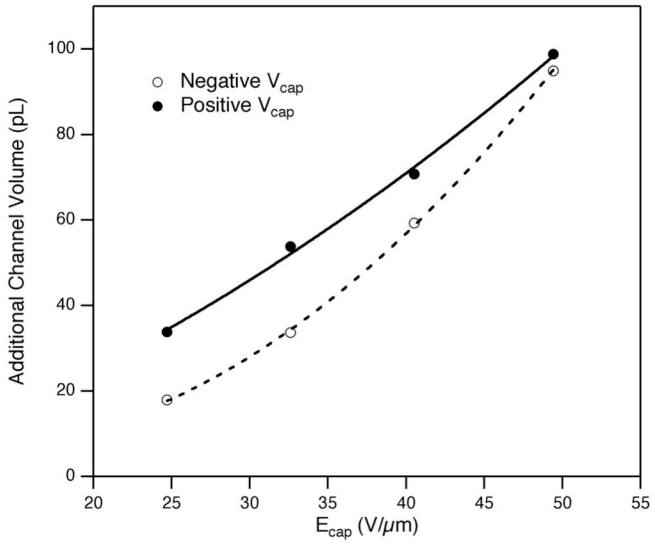

Figure 4.6 The relationship between the increase in channel volume and the magnitude of the electric field strength across the DE layer for both positive (solid line) and negative polarity (dashed line).

4.3.4. Investigation of Local Channel Compression In Large IDEAs

As stated in Section 2.2.5.1., for the IDEA-μCE device the potential in the microfluidic channel decreases linearly between the channel intersection and the sample waste reservoir. For the smallest IDEA (0.05 mm^2), the potential drop across the 1 mm electrode is negligible (~ 50 V for a 500 V/cm separation field strength). Conversely, the voltage drop across larger electrodes at the same separation field strength can be quite substantial (~ 500 V for a 1 cm electrode, ~ 1250 V for a 2.5 cm electrode and ~ 2000 V for a 4 cm electrode). In order to investigate how the potential drop in the channel can affect the deformation of the DE layer along the length of

the active channel section, we performed a fluorometric analysis of the channel deformation on each side of a 1 cm long IDEA during its operation.

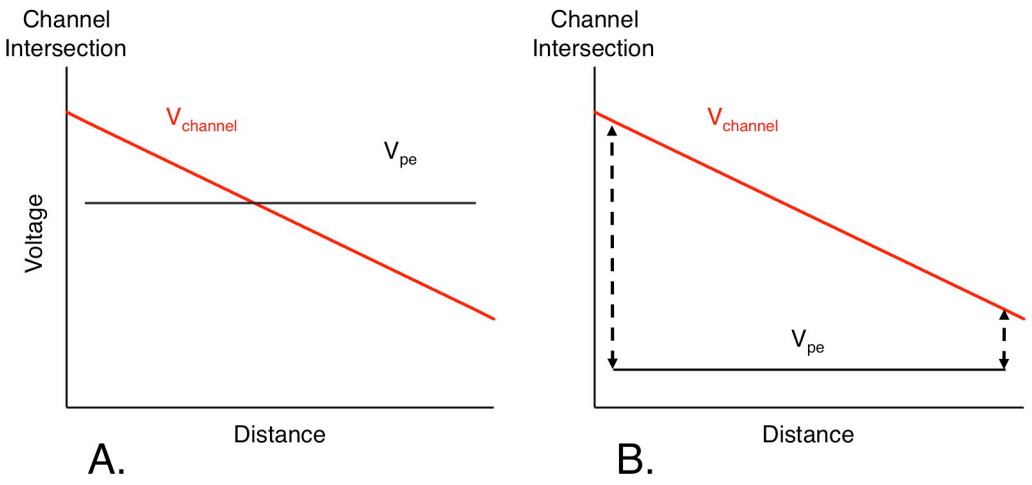

Figure 4.7 Graphs showing the general relationship between $V_{channel}$ and V_{pe} as a function of the distance from the channel intersection for the unactuated state (panel A) and the actuated state (panel B, $V_{cap} < 0$).

Figure 4.7 is a schematic that shows how the voltage drop in the microfluidic channel impacts the magnitude of V_{cap} in both the unactuated state (panel A) and the actuated state (panel B, $V_{cap} < 0$). In the unactuated state, V_{pe} is held at the average potential in the channel opposite the patterned electrode. In Chapter 2, this value was referred to as $V_{channel}$ (Equation 2.1) but here we are investigating the compression at different locations within the IDEA, so the terms $V_{channel}$ and V_{cap} will be used when looking at specific points along the length of the channel. With larger IDEAs, the microchannel in the "unactuated" state actually has a larger volume than it does in its native state. This is because V_{cap} can be quite significant in the regions of the IDEA closest to the intersection and the sample waster reservoir (Figure 4.7a). For the specific case when V_{pe} is lowered and the IDEA is actuated (Figure 4.7b), V_{cap} decreases linearly as a function of its distance from the channel intersection. As a result of this voltage configuration, one would expect that the amount of DE compression/channel deformation is greater on the channel intersection-side of the IDEA than on the sample waste reservoir-side of the IDEA.

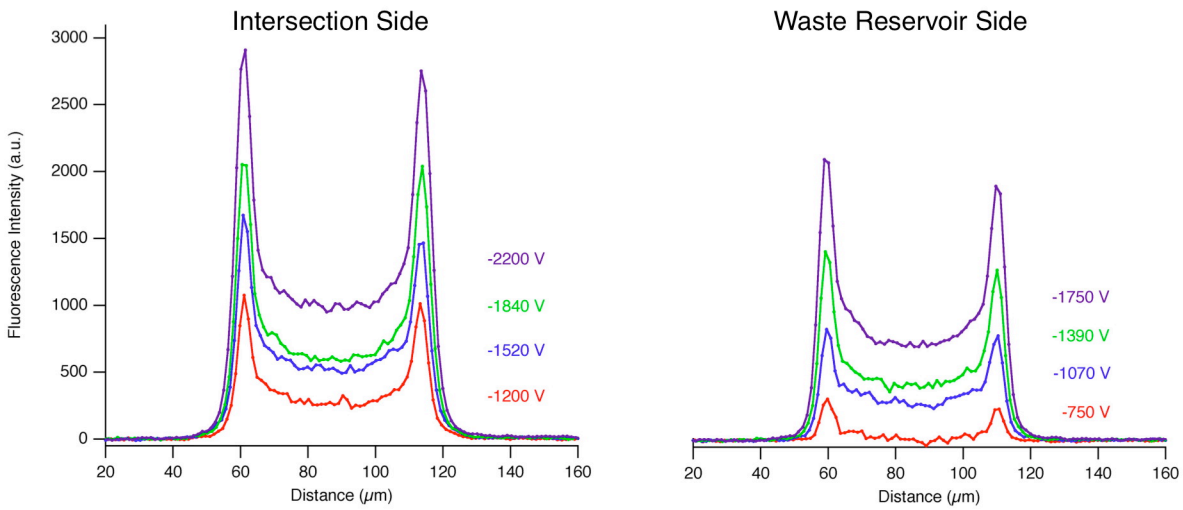

Figure 4.8 Graphs showing the differential line scans for average V_{cap} values of -1000 V (red), -1320 V (blue), -1640 V (green) and -2000 V (purple) recorded at two different locations on a large (0.50 mm^2) IDEA. The numbers to the right of each set of line scans are the V_{cap} values at that specific location.

Figure 4.8 shows the differential line scans measured at two different locations on the same IDEA during operation at average V_{cap} values of -1000 V, -1320 V, -1640 V and -2000 V. The device used for this analysis had a 0.50 mm^2 IDEA with a mean DE thickness of 41.43 µm. The location of the line scans recorded on the intersection-side of the IDEA was 690 µm downstream of the channel intersection. $V_{channel}$ at this location was approximately 2440 V. The location of the line scans recorded on the sample waste reservoir-side was 9795 µm downstream of the channel intersection. $V_{channel}$ at this location was approximately 1990 V. Thus, these two locations are separated by ~ 0.91 cm and the potential drop from one location to the other is 450 V. In the graphs, the values next to the differential line scans are the V_{cap} values at that specific location with the average V_{cap} values for the entire IDEA in the actuated state listed above. It is evident from this data that DE compression on the intersection-side of the IDEA is greater than that on the sample waste reservoir side of the IDEA. This data confirms the voltage analysis pictured in Figure 4.7.

Just as was done for the 0.05 mm^2 IDEA in Section 4.3.3., an approximate volume change in the active region of the 0.50 mm^2 IDEA can be obtained using the relationship between the integrals for the differential line scan and the mean unactuated line scan. For this calculation, it is assumed that the relationship between these two integrals is proportional to the

relationship between the increase in the area of the channel cross-section and the area of the channel cross-section in the unactuated state. This relationship is given by the following equation:

$$\frac{A_{dls}}{A_{muls}} = \frac{\Delta A_{cs}}{A_{cs}} \tag{4.2}$$

where A_{cs} is the cross-sectional area of the channel at the probed location during the unactuated state and ΔA_{cs} is the increase in the cross-sectional area of the channel at that same location when the IDEA is actuated. Values for ΔA_{cs} were calculated for each of the two probed locations (690 μm and 9795 μm downstream of the intersection) for each average value of V_{cap}. The data for these calculations, which assume that A_{cs} is equal to 1019 μm^2, can be seen in Table 4.2.

Table 4.2 Integrated fluorescence data from the line scans in Figure 4.8. The data was obtained directly from IGOR analysis using the "print area" command.

Local V_{cap}		A_{dls}	A_{muls}	A_{dls} / A_{muls}	ΔA_{cs} (μm^2)
Intersection Side					
-1200 V		20792.7	627965	0.033111	33.7
-1520 V		36800.8	628845	0.058521	59.6
-1840 V		45309.4	630046	0.071914	73.3
-2200 V		68892.4	628609	0.109495	111.6
Waste Reservoir Side					
-750 V		2988.4	599014	0.004989	5.1
-1070 V		18143.9	600698	0.030204	30.8
-1390 V		28323.0	604392	0.046862	47.8
-1750 V		47070.5	601988	0.078192	79.7

The relationship between the increase in cross-sectional area of the channel and the local V_{cap} is shown in Figure 4.9a. In order to calculate the increase in channel volume due to IDEA actuation, we assume that the change in cross-sectional area decreases linearly in the region of

the IDEA that lies between the two probed locations. Based on this assumption, the increase in channel volume due to actuator operation is defined as:

$$\Delta V = \left(\Delta A_{cs2} \times d\right) + 0.5d\left(\Delta A_{cs1} - \Delta A_{cs2}\right) \tag{4.3}$$

where ΔA_{cs1} is the increase in channel cross-sectional area for the intersection side, ΔA_{cs2} is the increase in channel cross-sectional area for the sample waste reservoir side, and d is the distance between these two locations (0.9105 cm). The relationship between the increase in channel volume and the average E_{cap} for the entire IDEA can be seen in Figure 4.9b. The trend between these two sets of values is reminiscent of that seen for the 0.05 mm^2 IDEA in Figure 4.6 although the increase in volume is ~ 9 × greater at each value of E_{cap}. This is to be expected since the 0.50 mm^2 IDEA has an active area that is 9 × larger. The largest actuator response (~ 871 pL), obtained at $|E_{cap}|$ = 48.3 V/μm, corresponds to an increase of 9.4% in the volume of the channel between the two probed locations.

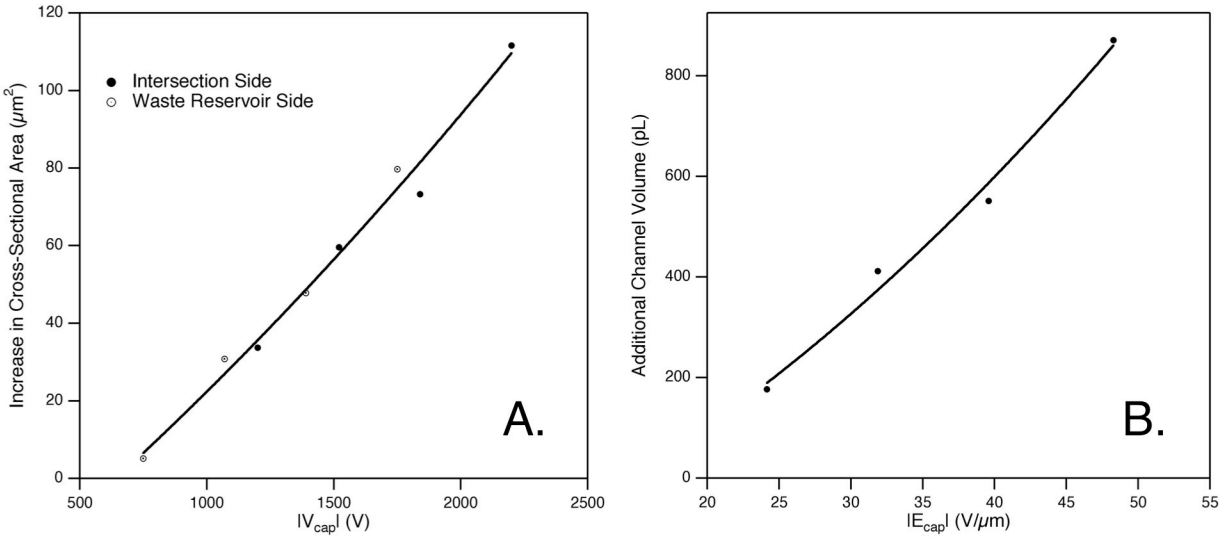

Figure 4.9 Panel A shows the relationship between the increase in the cross-sectional area of the channel as a function of V_{cap} for two different regions of a 0.50 mm^2 IDEA. Panel B shows the overall increase in channel volume as a function of the average E_{cap} for the entire IDEA.

4.3.5. Conclusions

Some of the spatial characteristics of channel deformation during the operation of an IDEA unit have been investigated. The electric field lines between the patterned electrode and

the microchannel during the actuated state have been modeled and were shown to agree with the theoretical results obtained by another group. Additionally, fluorescence microscopy was used to image the active channel region during IDEA operation. From these experiments, channel deformation across the width of the channel was observed and contributions from both DE compression and stretching were determined. This same technique was used to confirm theory regarding the electromechanical behavior of large IDEAs on a μCE device. The fluorometric data was also used to evaluate the approximate increase in channel volume as a function of V_{cap}/E_{cap} for both 0.05 mm^2 and 0.50 mm^2 IDEA units.

Chapter 5 - Conclusions and Future Research

The research presented in this dissertation has been focused on the development and characterization of a novel actuation system for PDMS-based microfluidic devices. The system exploits the ability of PDMS to act as a smart material in the presence of an electric field. IDEAs have the ability to decrease the footprint of highly integrated PDMS microfluidic systems by reducing the abundance of large, off-chip equipment that keeps these devices tethered to the laboratory environment. In Chapter 2, we described the configuration and fabrication of devices with integrated actuator units and investigated their performance with regards to the operating potential drop (V_{cap}), the elasticity of the DE layer and the size of the actuator. In Chapter 3, we evaluated the analytical merits of hydrodynamic injections produced by an IDEA unit located adjacent to the channel intersection of a μCE chip. It was determined that the integration of an IDEA unit onto a device featuring a standard μCE channel design is a simple solution to the problems caused by electrokinetic sampling bias. In Chapter 4, we sought out more detailed information about the nature of DE compression and the resultant channel deformation. The data we obtained from fluorescence microscopy experiments supports an existing model of DE compression in which more compression is present at the corners and along the edges of the DE as opposed to the middle of the actuator.

The basic research presented here has provided a foundation for more expansive, application-based research. As with many tools in the microfluidic "toolbox", we hope that researchers can look at the IDEA technology developed here and find ways to adapt it and optimize it for their own research applications. The concepts in the text below are just a couple of the potential areas of focus for the Culbertson group in the future.

5.1. IDEA Geometry Optimization

One of the most important goals for IDEA construction in the future is to reduce the fluidic resistance of a single IDEA unit while maximizing the increase in channel volume for a given value of V_{cap}. In this dissertation, we studied rectangular IDEAs with areas of 0.05 mm^2, 0.25 mm^2, 0.50 mm^2, 1.25 mm^2 and 2.00 mm^2. While the total IDEA area is small, the two largest actuators have effective lengths of 2.5 and 4.0 cm, which is too large to allow for multiple

IDEA units to be positioned in series on a miniaturized device. Moving forward, focus should be given to designing next-generation IDEAs with the information learned from the experiments in Chapter 4. That is, the geometry of both the microfluidic channel and the patterned electrode can be optimized in order to create more compact and more efficient IDEAs.

Preliminary observations in our lab (not shown) suggest that IDEAs with a "bubble cell" or oval channel design components (Figure 5.1a) have a much lower efficiency than similarly sized IDEAs featuring a rectangular channel with an extreme aspect ratio. This is due to the fact that the bubble cell design has a much lower total edge length. Future channel designs may employ simple serpentine patterns (Figure 5.1b), cross patterns (Figure 5.1c) or "channel & post" moieties (Figure 5.1d), among others, in order to increase edge length while reducing the effective size of the IDEA. Likewise, changing the design of the patterned electrode should also be able to increase IDEA efficiency. For instance, a patterned electrode with a "comb" design having teeth ~ 15 to 25 μm wide and spaced the same distance apart may be able to increase the IDEA efficiency (Figure 5.2). "High-edge" electrode designs like the "comb" concept may be effective enough to permit the use of low resistance channel architectures like the bubble cell.

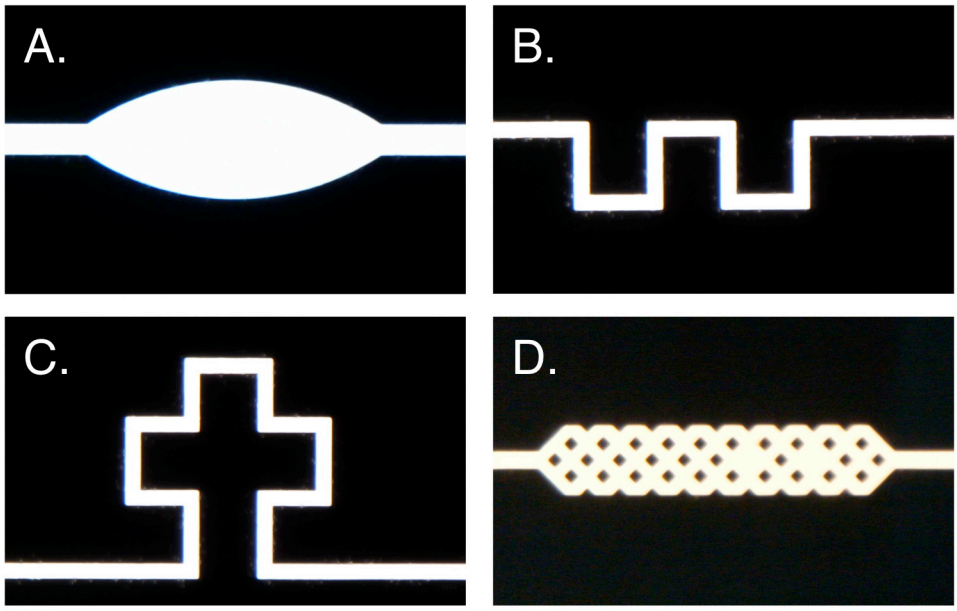

Figure 5.1 Non-standard channel geometries that can be used as the compliant electrode for an IDEA. Oval or "bubble cell" geometries (A) have not been observed to have high efficiencies, but serpentine (B), cross (C) and "channel & post" geometries may increase actuator efficiency due to their increased (edge length:total area) ratio.

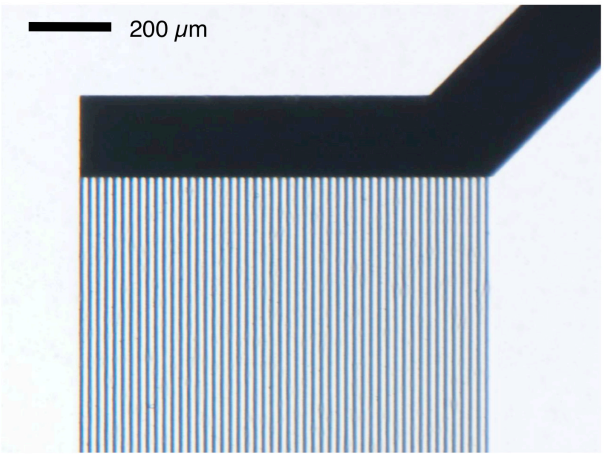

Figure 5.2 A "comb" electrode design that could potentially increase the efficiency of IDEA actuation by way of its high-edge density. The fingers of the "comb" are 10 μm wide and have a 10 μm gap between them.

5.2. Fluid Pumping

As the complexity of fluid-handling components increases, the need to precisely control the manner in which samples navigate the channel network of a microfluidic device has made integrated micro-pumps ubiquitous. Most of the actuation configurations listed in Section 2.1. are manifested as simple valves. A valving unit exists in either a "normally-closed" or "normally-open" state and then it switches to an "open" or "closed" state when it is activated. When the valve is in its "closed" state, the fluidic channel is essentially discontinuous. The serial combination of multiple valving units has been demonstrated to produce on-chip pumping.[9, 10, 29]

The ability to create IDEA pumping units and generate continuous hydrodynamic flow would be an asset for numerous applications where electrokinetic flow is undesirable (*e.g.* the handling of live cells). However, the IDEA configuration presented in this dissertation is incapable of forming valves, *i.e.* the channel is always in an "open" state. We postulate that the fluid drawn into the actuator region follows the path of least resistance and fluid expelled from the actuator region does the same. These two paths will always be the same, which means that under zero-flow conditions, a displaced volume of fluid will have returned to its original location after one charge-discharge cycle. Therefore, it will be necessary to incorporate check valves in order to produce a net flow in a given direction. Check valves are mechanical systems that

permit fluid movement in only a single direction. The diaphragm pump fabricated by Loverich *et al*. featured a set of PDMS swing check valves on either side of the compression chamber.[87]

By positioning one or more IDEA units in between a pair of check valves, we should be able to generate unidirectional peristaltic pumping on a microfluidic device (Figure 5.3).

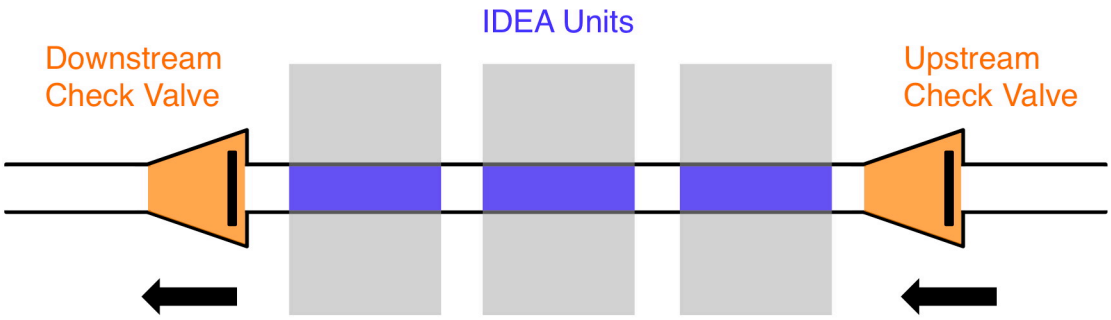

Figure 5.3 Schematic of a first-generation IDEA-pump. The pump consists of one or more IDEA units (three pictured above) that are positioned between two swing check valves.

In a proof-of-concept system, we will use swing check valves similar to those used by Loverich *et al*.[87] The operating component of this valve is a thin (10-20 µm) flap of PDMS that is attached to the ceiling of the channel. The PDMS flap has a clearance of ~ 2-3 µm so that it can move in response to the operation of the IDEA. A close-up of the check valves can be seen in Figure 5.4. Unlike the IDEA-µCE devices investigated in this dissertation, the fluidic channel will be connected to ground. This will ensure that the bulk fluid in the channels is relatively immobile when the IDEA is inactive. When an IDEA unit is charged, the fluid will pass through the upstream check valve and enter the pump. The downstream check valve will block fluid trying to enter the pump from this direction. When the IDEA is discharged, the excess fluid will only be able to exit through the downstream check valve.

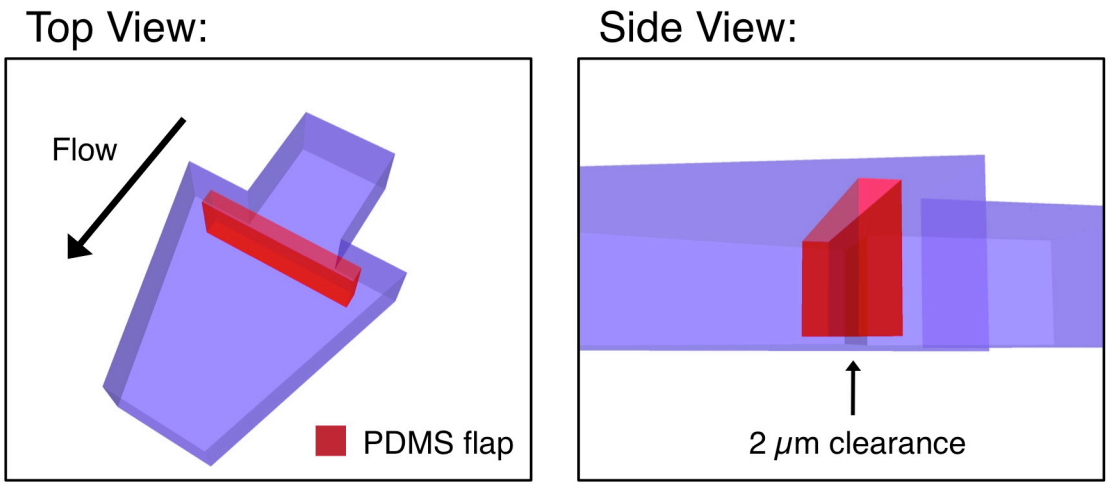

Figure 5.4 3D illustrations of the microfabricated swing check valves used in an IDEA-pump. The PDMS flap swings open when the flow moves along the arrow in the first panel, but swings shut when fluid attempts to move in the opposite direction. The second panel shows that the check valve does not completely block the depth of the channel .

5.2.1. IDEA-Pump Fabrication

The fabrication of the SU-8 mold used to make IDEA-pumps via soft lithography will be slightly different than that described in Section 2.2.2.3. This is due to the inclusion of the swing check valves. In order to produce working valves, multilayer SU-8 lithography must be employed. The first SU-8 layer will have a thickness of 2-3 μm, which provides the clearance between the PDMS flap and the floor of the channel. On top of this layer, a second SU-8 layer will be deposited at a thickness of ~ 20 μm. The thin SU-8 layer is patterned with UV photolithography to possess the design of the entire channel network. The thick SU-8 layer is patterned with photolithography to possess the design of the entire channel network except for the small rectangular cavity that will form the PDMS flap. The structures in these two layers must be aligned to one another using a mask alignment system. Once the multilayer SU-8 mold has been fabricated, the fabrication of the IDEA-pump device is the same as that described in Section 2.2.2.4.

5.2.2. IDEA-Pump Operation

In order to operate the pump, the fluidic channels will be filled with an aqueous electrolyte solution. An electrode that connects to ground will be inserted in one of the fluid

reservoirs. The performance of the pump can then be investigated with the use of one, two or three IDEA units. To power the system, the Electronics Design Lab at Kansas State University has already built a high-voltage power supply (0-2000 V) with 3 channels. The generated flow rate will be dependent on the frequency at which the IDEAs perform a charge-discharge cycle. If more than one IDEA unit is used for pumping, the flow rate can also be modified by changing the phase shift of the waveform applied to the units. The channels on the power supply box made by the KSU EDL are capable of producing charge-discharge waveforms with frequencies of 5, 10, 20, 40 and 80 Hz and twelve different phase shifts. By changing the charge-discharge frequency, phase shift and the operating V_{cap}, it should be possible to precisely tune the pump output over a large range of flow rates. Moreover, since the channel remains unobstructed at all times during operation, IDEA-pumps may prove more suitable than "open-closed" valving pumps when designing microfluidic systems to handle living cells or mimic physiological systems such as the microvasculature.

5.3. IDEA/Segmented-Flow Systems

One of the potential applications for which IDEA technology may be best suited is segmented-flow analysis. The reason for this is that the interaction between PDMS and aqueous solutions that result in large amounts of sorption and poor wettability are eliminated. Instead, aqueous "plugs" or "droplets" (the dispersed phase) are completely encapsulated by an immiscible oil phase (the continuous phase) that separates them both from each other and from the channel wall.[47, 48] The characteristics unique to microfluidic segmented-flow systems are namely four-fold and described as follows. First, transporting and analyzing liquid samples in plugs overcomes concentration limitations caused by sample dilution as the target analytes are contained within a droplet that is on the order of femtoliters to nanoliters and cannot significantly diffuse into the continuous phase. This is valuable for analyses that deal with very low concentrations of target analyte (*i.e.* single-cell analysis), whereas single-phase techniques with a high amount of dispersion can result in final analyte concentrations that are below the detection limit. Second, transporting samples in plugs practically eliminates cross-contamination between adjacent samples due of the elimination of non-specific sorption processes as mentioned above. Third, every plug is a discrete volume and therefore it is theoretically possible that each one can be manipulated and processed on an individual basis. This type of differentiation allows

numerous variables to be probed rapidly. Fourth, the aqueous plugs can be manipulated by changing the relationship between the surface tension of the dispersed phase and the viscosity and velocity of the continuous phase. These forces play a large role in droplet splitting,[56, 157, 158] reagent mixing,[54, 158] and various forms of "bubble logic".[56, 159, 160]

These characteristics of segmented-flow systems are especially advantageous for performing chemical reactions because each plug serves as a microreactor. Due to the inherent quality of microfluidic systems that translates time into distance, the plug content can be determined at different time points by interrogating the plugs at different locations in the channel network. Efficient heat and mass transfer on the microscale allow for uniform reaction conditions to be established quickly in each droplet. The precise application of temperatures and concentration gradients provides for control over the evolution of procedures such as particle synthesis,[55, 161, 162] protein crystallization,[25, 27] blood coagulation[163] and PCR.[164]

Despite the overall sophistication of "droplet-on-a-chip" devices, the use of external syringe pumps to drive fluid flow limits the flexibility of these systems. This is because fluid that is driven by a constant pressure source responds too slowly to input changes, which also must be performed manually. Thus, while it is theoretically possible that individual droplet plugs can each be treated as a discrete chemical system, it is not possible to actually do so under these circumstances. Specifically, these systems lack the ability to generate aqueous plugs on demand, discretely tune the size of consecutive plugs, and to control interspersion of aqueous plugs that originate from different sources. Recently, the accomplishment of the aforementioned tasks as well as controlled droplet fission has been demonstrated on segmented-flow devices with integrated pneumatic valves.[165-168] However, pneumatic control architectures are reliant upon external arrays of electromechanical or electromagnetic valves and a pressure source (vacuum pump or pressurized gas cylinder).

5.3.1. IDEA Plug Injector

We postulate that IDEA technology can be used in conjunction with careful engineering of the design and chemistry of the channel network to exert control over plug generation in segmented flow systems. The general concept is to use a standard T-junction to form the injector. Instead of having each aqueous solution individually addressable via a syringe pump or a pneumatic valve, each aqueous stream would be controlled with an IDEA unit and a pair of

microfabricated check valves (Figure 5.5). Reservoirs of sample and reagent that are electrically grounded could be maintained completely within the area of the microchip. With each "stroke" of the IDEA, the check valves ensure that fluid input occurs from the sample/reagent reservoir and that fluid output is injected into the oil stream as a plug. This configuration eliminates the need for numerous syringe pumps, reagent feed lines, and/or pneumatic control lines. It also enables the operator to produce plugs at programmable intervals (droplet-on-demand capability). In addition, IDEA technology is completely compatible with the use of electrohydrodynamic (EHD) forces to manipulate individual droplets,[169-172] since both of these strategies involve the use of electrodes that are insulated from the channel network by a thin PDMS film.

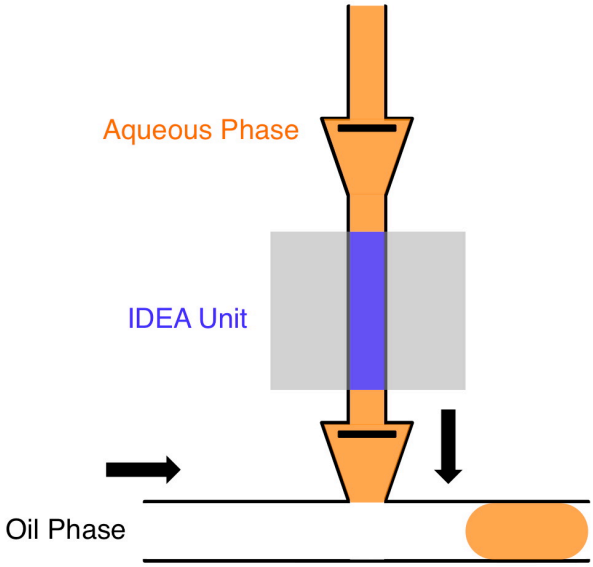

Figure 5.5 Schematic of a first-generation IDEA plug injector for segmented flow systems. Compression and relaxation of the DE layer brings aqueous sample/reagent in from a grounded feed reservoir and expels it into the oil phase. Each cycle forms a distinct plug.

5.3.1.1. IDEA Injector Fabrication

Due to the presence of the microfabricated check valve, the fabrication of the SU-8 mold necessary for soft lithography will be generally the same as described in Section 5.2.1. The thick SU-8 layer may end up being thicker (40 – 75 μm) in order to increase the throughput of the system. Device fabrication will be the same as that described in Section 2.2.2.4.

5.3.1.2. Channel Surface Modification

While the check valves should prohibit flow of the oil phase into the aqueous injection channel, they do not completely eliminate access to the sample/reagent reservoir. The hydrophobic oil phase will preferentially wet the hydrophobic surface of the native PDMS injection channel. If the channel segment in the IDEA region becomes coated in oil, actuation could be disrupted or even cease. Therefore, it may be necessary to modify the surface chemistry of the injection channel in order to increase its hydrophilicity and confine the oil phase to the segmented-flow channel.

In order to do this, we initially propose modifying the channel with a well-established sol-gel process. The fabrication of a sol-gel starts with a liquid, alkoxy precursor (the sol) that undergoes hydrolysis and condensation reactions in order to produce a colloidal suspension (the gel) that consists of metal oxide particles. As desolvation of the gel occurs, the final material is a porous, solid structure. The sol-gel process is a cheap and simple way to manufacture metal oxide materials, which lend their broad chemical versatility to the application at hand. For instance, our group has previously demonstrated the ability to modify the surface of PDMS with silicon oxide and metal oxide nanoparticles using sol-gel processing.[116, 173] In this work, it was determined that modification of PDMS with silica (SiO_2), titania (TiO_2), vanadia (VO_2) and zirconia (ZrO_2) nanoparticles increases the hydrophilicity of the surface.

This same protocol used in Ref. 173 will be used to increase the hydrophilicity of the PDMS in the injection channel. Briefly, the channel will be primed with reagent grade isopropanol followed by a 50% (v/v) solution of the metal alkoxide precursor and isopropanol. After flowing this solution through the channel for ~ 1 minute, the channel will be evacuated and air will be pulled through in order to dry it. The moisture in the air will trigger the hydrolysis reaction with metal alkoxide precursor that has absorbed into the PDMS channel walls. After a thorough drying period in which the metal alkoxide has been given sufficient time to react and form metal oxide nano-structures, the chip will be ready for use.

5.3.1.3. IDEA Plug Injector Operation

The first step in the injector operation is to fill the aqueous phase feed channel. In order for the injector to operate properly, this solution must be an electrolyte solution. An electrode than connects to ground will be inserted in the aqueous feed reservoir. The oil phase, which will be a perfluorocarbon oil (from the Fluorinert™ line made by 3M), will be pumped through the

main channel at a constant flow rate. The IDEA is controlled by a single high-voltage power supply. The magnitude of V_{cap} and the times at which the IDEA is charged and discharged can be programmed by the operator. Changing the magnitude of V_{cap} will alter the volume of the aqueous plug dispensed into the oil phase. If a particular frequency and a constant value of V_{cap} are desired, a channel of the power supply box made by the KSU EDL (discussed in Section 5.2.2.) can be used to operate the IDEA. If something more non-uniform is desired (both in frequency and V_{cap}-time), a high-voltage power supply controlled through Labview software will provide the flexibility required for complex plug formation sequences. The nature of these sequences are important as a series of plugs possessing predetermined volumes and intervals can be used to code information on top of the chemical information that is transported within the plug. That is, aqueous plugs with binary or even Morse code markers built into their sequence can be identified by the software and used to signal additional operations in the system.

References

(1) Effenhauser, C. S. In *Separation Methods in Microanalytical Systems*; Kutter, J. P., Fintschenko, Y., Eds.; CRC Press: Boca Raton, 2006, pp 575.
(2) Nguyen, N.-T.; Wereley, S. T. *Fundamentals and Applications of Microfluidics*, 2 ed.; Artech House, Inc.: Boston, 2006.
(3) Reyes, D. R.; Iossifidis, D.; Auroux, P.-A.; Manz, A. *Anal. Chem.* **2002**, *74*, 2623-2636.
(4) Harrison, D. J.; Fluri, K.; Seiler, K.; Fan, Z.; Effenhauser, C. S.; Manz, A. *Science* **1993**, *261*, 895-897.
(5) Manz, A.; Graber, N.; Widmer, H. M. *Sens. Actuators B Chem.* **1990**, *1*, 244-248.
(6) Skoog, D. A.; West, D. M.; Holler, F. J. *Fundamentals of Analytical Chemistry*, 7 ed.; Saunders College Publishing: Philadelphia, 1996.
(7) Liu, P. *Trends Biotechnol.* **2009**, *27*, 572-581.
(8) Hong, J. W.; Quake, S. R. *Nat. Biotechnol.* **2003**, *21*, 1179-1183.
(9) Unger, M. A.; Chou, H.-P.; Thorsen, T.; Scherer, A.; Quake, S. R. *Science* **2000**, *288*, 113-116.
(10) Grover, W. H.; Skelley, A. M.; Liu, C. N.; Lagally, E. T.; Mathies, R. A. *Sens. Actuators B Chem* **2003**, *89*, 315-323.
(11) Anderson, R. C.; Su, X.; Bogdan, G. J.; Fenton, J. *Nucleic Acids Res.* **2000**, *28*, E60.
(12) Burns, M. A.; Johnson, B. N.; Brahmasandra, S. N.; Handique, K.; Webster, J. R.; Krishnan, M.; Sammarco, T. S.; Man, P. M.; Jones, D.; Heldsinger, D.; Mastrangelo, C. H.; Burke, D. T. *Science* **1998**, *282*, 484-487.
(13) Easley, C. J.; Karlinsey, J. M.; Bienvenue, J. M.; Legendre, L. A.; Roper, M. G.; Feldman, S. H.; Hughes, M. A.; Hewlett, E. L.; Merkel, T. J.; Ferrance, J. P.; Landers, J. P. *Proc. Natl. Acad. Sci.* **2006**, *103*, 19272-19277.
(14) Lagally, E. T.; Scherer, J. R.; Blazej, R. G.; Toriello, N. M.; Diep, B. A.; Ramchandani, M.; Sensabough, G. F.; Riley, L. W.; Mathies, R. A. *Anal. Chem.* **2004**, *76*, 3162-3170.
(15) Liu, P.; Seo, T. S.; Beyor, N.; Shin, K.-J.; Scherer, J. R.; Mathies, R. A. *Anal. Chem.* **2007**, *79*, 1881-1889.
(16) Marcus, J. S.; Anderson, W. F.; Quake, S. R. *Anal. Chem.* **2006**, *78*, 3084-3089.
(17) Toriello, N. M.; Douglas, E. S.; Thaitrong, N.; Hsiao, S. C.; Francis, M. B.; Bertozzi, C. R.; Mathies, R. A. *Proc. Natl. Acad. Sci.* **2008**, *105*, 20173-20178.
(18) Zhong, J. F.; Chen, Y.; Marcus, J. S.; Scherer, A.; Quake, S. R.; Taylor, C. R.; Weiner, L. P. *Lab Chip* **2008**, *8*, 68-74.
(19) He, M.; Edgar, J. S.; Jeffries, G. D. M.; Lorenz, R. M.; Shelby, J. P.; Chiu, D. T. *Anal. Chem.* **2005**, *77*, 1539-1544.
(20) Huang, B.; Wu, H.; Bhaya, D.; Grossman, A.; Granier, S.; Kobilka, B. K.; Zare, R. N. *Science* **2007**, *315*, 81-84.
(21) McClain, M. A.; Culbertson, C. T.; Jacobson, S. C.; Allbritton, N. L.; Sims, C. E.; Ramsey, J. M. *Anal. Chem.* **2003**, *75*, 5646-5655.
(22) Wu, H.; Wheeler, A.; Zare, R. N. *Proc. Natl. Acad. Sci.* **2004**, *101*, 12809-12813.
(23) Thorsen, T.; Maerkl, S. J.; Quake, S. R. *Science* **2002**, *298*, 580-584.
(24) Ouellet, E.; Lausted, C.; Lin, T.; Yang, C. W. T.; Hood, L.; Lagally, E. T. *Lab Chip* **2010**, *10*, 581-588.

(25) Gerdts, C. J.; Tereshko, V.; Yadav, M. K.; Dementieva, I.; Collart, F.; Joachimiak, A.; Stevens, R. C.; Kuhn, P.; Kossiakoff, A.; Ismagilov, R. F. *Angew. Chem. Int. Ed.* **2006**, *45*, 8156-8160.
(26) Hansen, C. L.; Skordalakes, E.; Berger, J. M.; Quake, S. R. *Proc. Natl. Acad. Sci.* **2002**, *99*, 16531-16536.
(27) Li, L.; Mustafi, D.; Fu, Q.; Tereshko, V.; Chen, D. L.; Tice, J. D.; Ismagilov, R. F. *Proc. Natl. Acad. Sci.* **2006**, *103*, 19243-19248.
(28) Fu, A. Y.; Chou, H.-P.; Spence, C.; Arnold, F. H.; Quake, S. R. *Anal. Chem.* **2002**, *74*, 2451-2457.
(29) Gu, W.; Zhu, X.; Futai, N.; Cho, B. S.; Takayama, S. *Proc. Natl. Acad. Sci. USA* **2004**, *101*, 15861-15866.
(30) Huang, C.-J.; Chen, Y.-H.; Wang, C.-H.; Chou, T.-C.; Lee, G.-B. *Sens. Actuators B Chem.* **2007**, *122*, 461-468.
(31) Wang, C.-H.; Lee, G.-B. *Biosens. Bioelectron.* **2005**, *21*, 419-425.
(32) Terry, S. C.; Jerman, J. H.; Angell, J. B. *IEEE Trans. Electron Devices* **1979**, *26*, 1880-1886.
(33) Effenhauser, C. S.; Bruin, G. J. M.; Paulus, A.; Ehrat, M. *Anal. Chem.* **1997**, *69*, 3451-3457.
(34) Duffy, D. C.; McDonald, J. C.; Schueller, O. J. A.; Whitesides, G. M. *Anal. Chem.* **1998**, *70*, 4974-4984.
(35) In *http://www.dowcorning.com/content/sitech/sitechms/*.
(36) Lewis, L. N. In *Silicones and Silicone-Modified Materials*; Clarson, S. J., Fitzgerald, J. J., Owen, M. J., Smith, S. D., Eds.; American Chemical Society: Washington, D.C., 2000, pp 11-19.
(37) Eddings, M. A.; Johnson, M. A.; Gale, B. K. *J. Micromech. Microeng.* **2008**, *18*, 067001/067001-067001/067004.
(38) Samel, B.; Chowdhury, M. K.; Stemme, G. *J. Micromech. Microeng.* **2007**, *17*, 1710-1714.
(39) Satyanarayana, S.; Karnik, R. N.; Majumdar, A. *J. Microelectromech. Syst.* **2005**, *14*, 392-399.
(40) Wu, H.; Huang, B.; Zare, R. N. *Lab Chip* **2005**, *5*, 1393-1398.
(41) Eddings, M. A.; Gale, B. K. *J. Micromech. Microeng.* **2006**, *16*, 2396-2402.
(42) Hung, P. J.; Lee, P. J.; Sabounchi, P.; Aghdam, N.; Lin, R.; Lee, L. P. *Lab Chip* **2005**, *5*, 44-48.
(43) Leclerc, E.; Sakai, Y.; Fujii, T. *Biomed. Microdevices* **2003**, *5*, 109-114.
(44) Rhee, S. W.; Taylor, A. M.; Tu, C. H.; Cribbs, D. H.; Cotman, C. W.; Jeon, N. L. *Lab Chip* **2005**, *5*, 102-107.
(45) Toepke, M. W.; Beebe, D. J. *Lab Chip* **2006**, *6*, 1484-1486.
(46) Lee, J. N.; Park, C.; Whitesides, G. M. *Anal. Chem.* **2003**, *75*, 6544-6554.
(47) Nisisako, T.; Torii, T.; Higuchi, T. *Lab Chip* **2002**, *2*, 24-26.
(48) Thorsen, T.; Roberts, R. W.; Arnold, F. H.; Quake, S. R. *Phys. Rev. Lett.* **2001**, *86*, 4163-4166.
(49) Madou, M. J. *Fundamentals of Microfabrication: The Science of Miniaturization*, 2nd ed.; CRC Press: Boca Raton, 2002.
(50) Beebe, D. J.; Mensing, G. A.; Walker, G. M. *Annu. Rev. Biomed. Eng.* **2002**, *4*, 261-286.

(51) Bard, A. J.; Faulkner, L. R. *Electrochemical Methods: Fundamentals and Applications*, 2nd ed.; John Wiley & Sons, Inc.: New York, 2001.
(52) Walker, G. M.; Beebe, D. J. *Lab Chip* **2002**, *2*, 131-134.
(53) Zhao, B.; Moore, J. S.; Beebe, D. J. *Science* **2001**, *291*, 1023-1026.
(54) Tice, J. D.; Song, H.; Lyon, A. D.; Ismagilov, R. F. *Langmuir* **2003**, *19*, 9127-9133.
(55) Shestopalov, I.; Tice, J. D.; Ismagilov, R. F. *Lab Chip* **2004**, *4*, 316-321.
(56) Tan, Y.-C.; Fisher, J. S.; Lee, A. I.; Cristini, V.; Lee, A. P. *Lab Chip* **2004**, *4*, 292-298.
(57) Day, M. A. *Erkenntnis* **1990**, *33*, 285-296.
(58) Giddings, J. C. *Unified Separation Science*; John Wiley & Sons, Inc.: New York, 1991.
(59) Tiselius, A. *Trans. Faraday Soc.* **1937**, *33*, 524-531.
(60) Jorgenson, J. W.; Lukacs, K. D. *Anal. Chem.* **1981**, *53*, 1298-1302.
(61) Harrison, D. J.; Manz, A.; Fan, Z.; Lüdi, H.; Widmer, H. M. *Anal. Chem.* **1992**, *64*, 1926-1932.
(62) Jacobson, S. C.; Hergenröder, R.; Koutny, L. B.; Ramsey, J. M. *Anal. Chem.* **1994**, *66*, 1114-1118.
(63) Manz, A.; Harrison, D. J.; Verpoorte, E. M. J.; Fettinger, J. C.; Paulus, A.; Lüdi, H.; Widmer, H. M. *J. Chromatogr.* **1992**, *593*, 253-258.
(64) Poole, C. F. *The Essence of Chromatography*; Elsevier: Amsterdam, 2003.
(65) Schoch, R. B.; Han, J.; Renaud, P. *Rev. Mod. Phys.* **2008**, *80*, 839-883.
(66) Hayes, M. A.; Kheterpal, I.; Ewing, A. G. *Anal. Chem.* **1993**, *65*, 27-31.
(67) Jacobson, S. C.; Culbertson, C. T. In *Separation Methods in Microanalytical Systems,* 1st ed.; Kutter, J. P., Fintschenko, Y., Eds.; CRC Press: Boca Raton, 2006, pp 575.
(68) Martin, A. J. P.; Synge, R. L. M. *Biochem. J.* **1941**, *35*, 1358-1368.
(69) Biddiss, E.; Chau, T. *Med. Eng. Phys.* **2008**, *30*, 403-418.
(70) Goulbourne, N.; Mockensturm, E.; Frecker, M. In *Dielectric Elastomers as Electromechanical Transducers*; Carpi, F., De Rossi, D., Kornbluh, R., Pelrine, R., Sommer-Larsen, P., Eds.; Elsevier: Amsterdam, 2008, pp 177-188.
(71) Heydt, R.; Kornbluh, R.; Pelrine, R.; Mason, V. *J. Sound Vibr.* **1998**, *215*, 297-311.
(72) Heydt, R.; Pelrine, R.; Joseph, J.; Eckerle, J.; Kornbluh, R. D. *J. Acoust. Soc. Am.* **2000**, *107*, 833-839.
(73) Kornbluh, R. D.; Pelrine, R. E.; Prahlad, H.; Heydt, R. *MEMS/MOEMS Components and Their Applications* **2004**, *5344*, 13-27.
(74) Pei, Q.; Pelrine, R.; Stanford, S.; Kornbluh, R.; Rosenthal, M. *Synth. Met.* **2003**, *135*, 129-131.
(75) Pelrine, R.; Kornbluh, R.; Pei, Q.; Joseph, J. *Science* **2000**, *287*, 836-839.
(76) Shankar, R.; Ghosh, T. K.; Spontak, R. J. *Soft Matter* **2007**, *3*, 1116-1129.
(77) Zhang, X.; Löwe, C.; Wissler, M.; Jähne, B.; Kovacs, G. *Adv. Eng. Mater.* **2005**, *7*, 361-367.
(78) Shiga, T. In *Neutron Spin Echo Spectroscopy Viscoelasticity Rheology*; Springer-Verlag: Berlin, 1997, pp 133-162.
(79) Akle, B. J.; Bennett, M. D.; Leo, D. J. *Sens. Actuators A Phys.* **2006**, *126*, 173-181.
(80) Kaneto, K.; Kaneko, M.; Min, Y.; MacDiarmid, A. G. *Synth. Met.* **1995**, *71*, 2211-2212.
(81) Nemat-Nasser, S.; Wu, Y. *J. Appl. Phys.* **2003**, *93*, 5255-5267.
(82) Pei, Q.; Inganäs, O. *Adv. Mater.* **1992**, *4*, 277-278.
(83) Smela, E.; Inganäs, O.; Lundström, I. *Science* **1995**, *268*, 1735-1738.

(84) Baughman, R. H.; Cui, C.; Zakhidov, A. A.; Iqbal, Z.; Barisci, J. N.; Spinks, G. M.; Wallace, G. G.; Mazzoldi, A.; De Rossi, D.; Rinzler, A. G.; Jaschinski, O.; Roth, S.; Kertesz, M. *Science* **1999**, *284*, 1340-1344.
(85) Pelrine, R. E.; Kornbluh, R. D.; Joseph, J. P. *Sens. Actuators A Phys.* **1998**, *64*, 77-85.
(86) Carpi, F.; Chiarelli, P.; Mazzoldi, A.; De Rossi, D. *Sens. Actuators A Phys.* **2003**, *107*, 85-95.
(87) Loverich, J. J.; Kanno, I.; Kotera, H. *Lab Chip* **2006**, *6*, 1147-1154.
(88) Ma, W.; Cross, L. E. *Appl. Phys. A* **2004**, *78*, 1201-1204.
(89) Dubois, P.; Rosset, S.; Koster, S.; Stauffer, J.; Mikhaïlov, S.; Dadras, M.; de Rooij, N.-F.; Shea, H. *Sens. Actuators A Phys.* **2006**, *130-131*, 147-154.
(90) Rosset, S.; Niklaus, M.; Dubois, P.; Shea, H. *Adv. Funct. Mater.* **2009**, *19*, 470-478.
(91) Trujillo, R.; Mou, J.; Phelan, P. E.; Chau, D. S. *Int. J. Adv. Manuf. Technol.* **2004**, *23*, 176-182.
(92) Carpi, F.; Migliore, A.; De Rossi, D. *Proc. SPIE* **2005**, *5759*, 64-74.
(93) Pelrine, R.; Kornbluh, R.; Joseph, J.; Heydt, R.; Pei, Q.; Chiba, S. *Mater. Sci. Eng. C* **2000**, *11*, 89-100.
(94) Pelrine, R.; Kornbluh, R. In *Dielectric Elastomers as Electromechanical Transducers*; Carpi, F., De Rossi, D., Kornbluh, R., Pelrine, R., Sommer-Larsen, P., Eds.; Elsevier: Amsterdam, 2008, pp 3-12.
(95) Macosko, C. W. *Rheology: principles, measurements and applications*; VCH Publishers, Inc.: New York, 1994.
(96) Ogden, R. W. *Proc. Roy. Soc. Lond. A* **1972**, *326*, 565-584.
(97) Nam, J.-D.; Choi, H. R.; Koo, J. C.; Lee, Y. K.; Kim, K. J. In *Electroactive Polymers for Robotics Applications*; Kim, K. J., Tadokoro, S., Eds.; Springer-Verlag: London, 2007, pp 37-48.
(98) Van Krevelen, D. W. *Properties of Polymers: Their Estimation and Correlation with Chemical Structure*, 2nd ed.; Elsevier: Amsterdam, 1976.
(99) Gottlieb, M.; Macosko, C. W.; Lepsch, T. C. *J. Polym. Sci., Phys. Ed.* **1981**, *19*, 1603-1617.
(100) Kofod, G.; Sommer-Larsen, P.; Kornbluh, R.; Pelrine, R. *J. Intell. Mater. Syst. Struct.* **2003**, *14*, 787-793.
(101) O'Halloran, A.; O'Malley, F. In *Topics in Bio-Mechanical Engineering*; Prendergast, P. J., McHugh, P. E., Eds.; TCBE & NCBES: Dublin, 2004, pp 184-215.
(102) Kofod, G. *J. Phys. D Appl. Phys.* **2008**, *41*, 215405-215401-215405-215411.
(103) Lee, S. J.; Chan, J. C.-Y.; Maung, K. J.; Rezler, E.; Sundararajan, N. *J. Micromech. Microeng.* **2007**, *17*, 843-851.
(104) Handique, K.; Burke, D. T.; Mastrangelo, C. H.; Burns, M. A. *Anal. Chem.* **2001**, *73*, 1831-1838.
(105) Graf, N. J.; Bowser, M. T. *Lab Chip* **2008**, *8*, 1664-1670.
(106) Tan, C. K. L.; Tracey, M. C.; Davis, J. B.; Johnston, I. D. *J. Micromech. Microeng.* **2005**, *15*, 1885-1893.
(107) Vyawahare, S.; Sitaula, S.; Martin, S.; Adalian, D.; Scherer, A. *Lab Chip* **2008**, *8*, 1530-1535.
(108) Kaigala, G. V.; Hoang, V. N.; Backhouse, C. J. *Lab Chip* **2008**, *8*, 1071-1078.
(109) Pal, R.; Yang, M.; Johnson, B. N.; Burke, D. T.; Burns, M. A. *Anal. Chem.* **2004**, *76*, 3740-3748.

(110) Lee, D. E.; Soper, S.; Wang, W. *Microsyst. Technol.* **2008**, *14*, 1751-1756.
(111) Machauf, A.; Nemirovsky, Y.; Dinnar, U. *J. Micromech. Microeng.* **2005**, *15*, 2309-2316.
(112) Xie, J.; Shih, J.; Lin, Q.; Yang, B.; Tai, Y.-C. *Lab Chip* **2004**, *4*, 495-501.
(113) Pan, T.; McDonald, S. J.; Kai, E. M.; Ziaie, B. *J. Micromech. Microeng.* **2005**, *15*, 1021-1026.
(114) Sadler, D. J.; Singh, G.; Zenhausern, F.; Saraf, R. F. *Mat. Res. Soc. Symp. Proc.* **2003**, *741*, J1.2.1-6.
(115) Jacobson, S. C.; Koutny, L. B.; Hergenröder, R.; Moore, A. W.; Ramsey, J. M. *Anal. Chem.* **1994**, *66*, 3472-3476.
(116) Roman, G. T.; Hlaus, T.; Bass, K. J.; Seelhammer, T. G.; Culbertson, C. T. *Anal. Chem.* **2005**, *77*, 1414-1422.
(117) Kornbluh, R.; Pelrine, R.; Joseph, J.; Heydt, R.; Pei, Q.; Chiba, S. *Smart Mater. Struct.* **1999**, *3669*, 149-160.
(118) Lacour, S. P.; Prahlad, H.; Pelrine, R.; Wagner, S. *Sens. Actuators A Phys.* **2004**, *111*, 288-292.
(119) Galler, N.; Ditlbacher, H.; Steinberger, B.; Hohenau, A.; Dansachmüller, M.; Camacho-Gonzales, F.; Bauer, S.; Krenn, J. R.; Leitner, A.; Aussenegg, F. R. *Appl. Phys. B* **2006**, *85*, 7-10.
(120) Kofod, G.; Sommer-Larsen, P. In *Dielectric Elastomers as Electromechanical Transducers*; Carpi, F., De Rossi, D., Kornbluh, R., Pelrine, R., Sommer-Larsen, P., Eds.; Elsevier: Amsterdam, 2008, pp 159-168.
(121) Buch, J. S.; Wang, P.-C.; DeVoe, D. L.; Lee, C. S. *Electrophoresis* **2001**, *22*, 3902-3907.
(122) Schasfoort, R. B. M.; Schautmann, S.; Hendrikse, J.; van den Berg, A. *Science* **1999**, *286*, 942-945.
(123) Lee, C. S.; Blanchard, W. C.; Wu, C.-T. *Anal. Chem.* **1990**, *62*, 1550-1552.
(124) Horiuchi, K.; Dutta, P. *Lab Chip* **2006**, *6*, 714-723.
(125) Kim, S. M.; Burns, M. A.; Hasselbrink, E. F. *Anal. Chem.* **2006**, *78*, 4779-4785.
(126) Jacobson, S. C.; Hergenröder, R.; Koutny, L. B.; Warmack, R. J.; Ramsey, J. M. *Anal. Chem.* **1994**, *66*, 1107-1113.
(127) Effenhauser, C. S.; Manz, A.; Widmer, H. M. *Anal. Chem.* **1993**, *65*, 2637-2642.
(128) Jacobson, S. C.; Ermakov, S. V.; Ramsey, J. M. *Anal. Chem.* **1999**, *71*, 3273-3276.
(129) Mecker, L. C.; Martin, R. S. *Anal. Chem.* **2008**, *80*, 9257-9264.
(130) Roper, M. G.; Shackman, J. G.; Dahlgren, G. M.; Kennedy, R. T. *Anal. Chem.* **2003**, *75*, 4711-4717.
(131) Shackman, J. G.; Dahlgren, G. M.; Peters, J. L.; Kennedy, R. T. *Lab Chip* **2005**, *5*, 56-63.
(132) Gottschlich, N.; Jacobson, S. C.; Culbertson, C. T.; Ramsey, J. M. *Anal. Chem.* **2001**, *73*, 2669-2674.
(133) Ramsey, J. D.; Jacobson, S. C.; Culbertson, C. T.; Ramsey, J. M. *Anal. Chem.* **2003**, *75*, 3758-3764.
(134) Rocklin, R. D.; Ramsey, R. S.; Ramsey, J. M. *Anal. Chem.* **2000**, *72*, 5244-5249.
(135) Huang, X.; Gordon, M. J.; Zare, R. N. *Anal. Chem.* **1988**, *60*, 375-377.
(136) Blas, M.; Delaunay, N.; Ferrigno, R.; Rocca, J.-L. *Electrophoresis* **2007**, *28*, 2961-2970.
(137) Slentz, B. E.; Penner, N. A.; Regnier, F. *Anal. Chem.* **2002**, *74*, 4835-4840.
(138) Backofen, U.; Matysik, F.-M.; Lunte, C. E. *Anal. Chem.* **2002**, *74*, 4054-4059.
(139) Gai, H.; Yu, L.; Dai, Z.; Ma, Y.; Lin, B. *Electrophoresis* **2004**, *25*, 1888-1894.

(140) Luo, Y.; Wu, D.; Zeng, S.; Gai, H.; Long, Z.; Shen, Z.; Dai, Z.; Qin, J.; Lin, B. *Anal. Chem.* **2006**, *78*, 6074-6080.
(141) Fütterer, C.; Minc, N.; Bormuth, V.; Codarbox, J.-H.; Laval, P.; Rossier, J.; Viovy, J.-L. *Lab Chip* **2004**, *4*, 351-356.
(142) Lacharme, F.; Gijs, M. A. M. *Electrophoresis* **2006**, *27*, 2924-2932.
(143) Solignac, D.; Gijs, M. A. M. *Anal. Chem.* **2003**, *75*, 1652-1657.
(144) Li, M. W.; Martin, R. S. *Electrophoresis* **2007**, *28*, 2478-2488.
(145) Lin, C.-C.; Chen, C.-C.; Lin, C.-E.; Chen, S.-H. *J. Chromatogr. A* **2004**, *1051*, 69-74.
(146) Qi, L.-Y.; Yin, X.-F.; Zhang, L.; Wang, M. *Lab Chip* **2008**, *8*, 1137-1144.
(147) Zhang, L.; Yin, X.; Fang, Z. *Lab Chip* **2006**, *6*, 258-264.
(148) Easley, C. J.; Karlinsey, J. M.; Landers, J. P. *Lab Chip* **2006**, *6*, 601-610.
(149) Karlinsey, J. M.; Monahan, J.; Marchiarullo, D. J.; Ferrance, J. P.; Landers, J. P. *Anal. Chem.* **2005**, *77*, 3637-3643.
(150) Li, B.; Jiang, L.; Wang, Q.; Qin, J.; Lin, B. *Electrophoresis* **2008**, *29*, 4906-4913.
(151) Ermakov, S. V.; Jacobson, S. C.; Ramsey, J. M. *Anal. Chem.* **2000**, *72*, 3512-3517.
(152) Price, A. K.; Anderson, K. M.; Culbertson, C. T. *Lab Chip* **2009**, *9*, 2076-2084.
(153) Karger, B. L.; Snyder, L. R.; Horvath, C. *An Introduction to Separation Science*; John Wiley & Sons, Inc.: New York, 1973.
(154) Hayes, M. A.; Ewing, A. G. *Anal. Chem.* **1992**, *64*, 512-516.
(155) Lee, C. S.; McManigill, D.; Wu, C.-T.; Patel, B. *Anal. Chem.* **1991**, *63*, 1519-1523.
(156) Soulimane, S.; Al Ahmad, M.; Matmat, M.; Camon, H. *Thermal, Mechanical and Multi-Physics Simulation and Experiments in Microelectronics and Micro-Systems, 2008. EuroSimE 2008.* **2008**, 1-4.
(157) Link, D. R.; Anna, S. L.; Weitz, D. A.; Stone, H. A. *Phys. Rev. Lett.* **2004**, *92*, 054503.
(158) Song, H.; Tice, J. D.; Ismagilov, R. F. *Angew. Chem. Int. Ed.* **2003**, *42*, 767-772.
(159) Fuerstman, M. J.; Garstecki, P.; Whitesides, G. M. *Science* **2007**, *315*, 828-832.
(160) Prakash, M.; Gershenfeld, N. *Science* **2007**, *315*, 832-835.
(161) Hung, L.-H.; Choi, K. M.; Tseng, W.-Y.; Tan, Y.-C.; Shea, K. J.; Lee, A. P. *Lab Chip* **2006**, *6*, 174-178.
(162) Xu, S.; Nie, Z.; Seo, M.; Lewis, P.; Kumacheva, E.; Stone, H. A.; Garstecki, P.; Weibel, D. B.; Gitlin, I.; Whitesides, G. M. *Angew. Chem. Int. Ed.* **2005**, *44*, 724-728.
(163) Song, H.; Chen, D. L.; Ismagilov, R. F. *Angew. Chem. Int. Ed.* **2006**, *45*, 7336-7356.
(164) Beer, N. J.; Hindson, B. J.; Wheeler, E. K.; Hall, S. B.; Rose, K. A.; Kennedy, I. M.; Colston, B. W. *Anal. Chem.* **2007**, *79*, 8471-8475.
(165) Choi, J.-H.; Lee, S.-K.; Lim, J.-M.; Yang, S.-M.; Yi, G.-R. *Lab Chip* **2010**, *10*, 456-461.
(166) Churski, K.; Michalski, J.; Garstecki, P. *Lab Chip* **2010**, *10*, 512-518.
(167) Willaime, H.; Barbier, V.; Kloul, L.; Maine, S.; Tabeling, P. *Phys. Rev. Lett.* **2006**, *96*, 054501.
(168) Zeng, S.; Li, B.; Su, X.; Qin, J.; Lin, B. *Lab Chip* **2009**, *9*, 1340-1343.
(169) Ahn, K.; Agresti, J.; Chong, H.; Marquez, M.; Weitz, D. A. *Appl. Phys. Lett.* **2006**, *88*, 264105.
(170) Kim, H.; Luo, D.; Link, D. R.; Weitz, D. A.; Marquez, M.; Cheng, Z. *Appl. Phys. Lett.* **2007**, *91*, 133106.
(171) Link, D. R.; Grasland-Mongrain, E.; Duri, A.; Sarrazin, F.; Cheng, Z.; Cristobal, G.; Marquez, M.; Weitz, D. A. *Angew. Chem. Int. Ed.* **2006**, *45*, 2556-2560.
(172) Wang, W.; Yang, C.; Liu, Y. S.; Li, C. M. *Lab Chip* **2010**, *10*.

(173) Roman, G. T.; Culbertson, C. T. *Langmuir* **2006**, *22*, 4445-4451.